Decoding protein kinase signaling during mitosis: Exploiting molecular scaffolds and developing drug-targeting tools for studying local kinase biology

Paula Bucko

A dissertation
submitted in partial fulfillment of the
requirements for the degree of

Doctor of Philosophy

University of Washington
2020

Reading Committee:
John D. Scott, Chair
Linda Wordeman
Dustin Maly

Program Authorized to Offer Degree:
Pharmacology

University of Washington

ABSTRACT

Decoding protein kinase signaling during mitosis: Exploiting molecular scaffolds and developing drug-targeting tools for studying local kinase biology

Paula Bucko

Chair of the Supervisory Committee:
John D. Scott
Department of Pharmacology

Fundamental cellular processes such as cell division, migration, differentiation, and growth require environmental signals to be converted into chemical responses that generate biological outputs. Accordingly, these events rely on the precise and timely regulation of signaling proteins inside the cell. Organization of enzymes in space and time becomes particularly important in a process such as mitosis where regulation of mitotic protein kinases ensures that DNA is properly segregated between the two daughter cells. During mitosis, two key protein kinases, Aurora A and polo-like kinase 1 (Plk1) carry out many functions to ensure the fidelity of cell division. Current approaches in which small-molecule kinase inhibitor drugs are used to ascribe function to Aurora A and Plk1 provide important insight into the global roles of these proteins inside the cell. However, since these enzymes share similar localization patterns and many overlapping roles, knowing their individual contributions at specific locations is not possible with existing pharmacological approaches. This is because traditional inhibitor drugs distribute throughout the cell, inhibiting enzymes at many locations, and thus limit the ability to resolve how a protein functions at a distinct organelle. Therefore, decoding the roles of Aurora A and Plk1 at distinct subcellular locations is critical for understanding how cell division is regulated. More importantly, elucidating local kinase action can uncover how signaling becomes dysregulated in disease, thus paving the way for development of more effective therapeutics.

Using a combination of chemical genetics, gene-editing, super-resolution microscopy, live-cell imaging, and biochemistry the studies in this thesis uncover how Aurora A and Plk1 coordinate signaling events at distinct locations in the cell during mitosis. In this work, I exploit the local scaffolding ability of Gravin, an A-kinase anchoring protein (AKAP), to study how anchored pools of Aurora A and Plk1 facilitate mitotic events. Additionally, I develop a new drug-targeting system called LoKI (Local Kinase Inhibition) to deliver Aurora A and Plk1 inhibitors to specific subcellular locations to further probe local kinase action. My studies uncover that Gravin localizes active pools of Aurora A and Plk1 at mitotic centrosomes and show that loss of local kinase activity at this location attenuates substrate phosphorylation, produces mitotic spindle defects, and prolongs mitosis. I also discover a new role for this anchoring protein in coordinating the recruitment of γ-tubulin during mitosis and demonstrate that loss of Gravin disrupts protein-protein interactions that facilitate the proper targeting of this key microtubule nucleating component. Together, these studies elucidate how local kinase action drives mitosis and provide evidence that subcellular targeting of protein kinases is a molecular mechanism that underlies precise execution of critical protein phosphorylation events inside cells.

ACKNOWLEDGEMENTS

I would first like to thank my PhD advisor, John, for his support, guidance, and encouragement throughout graduate school. For all of the opportunities he has given me, allowing me to pursue the questions that excited me most, giving me a venue to mentor undergraduate students, and offering me the chance to present my work across the globe, I am sincerely grateful. Thank you to members of my committee, Linda Wordeman, Dusty Maly, Edith Wang, and Nephi Stella for input and advice over the years. Thank you to the Pharmacology Department especially Debbie, Jenny, and Diane. A special thanks to the Wordeman lab: Linda, Juanje, Mike, and Justin I appreciate you welcoming me in as one of your own, inviting me to your lab meetings and for your mentorship and feedback throughout my time as a PhD student. Thank you to all members of the Scott lab for the support and assistance over the years but especially to Donelson, Stacey, Janani, Laura, Rigney, Katherine, and Mitch for the countless discussions that were so valuable to shaping me along this journey. Thank you to the fearless undergraduate students Akansha Bhat, Irvin Garcia, and Ridhima Manocha for their willingness to work with me, their dedication to the research, and their excitement to venture into the unknown. You have taught me to ask better questions, appreciate the findings, and to be a stronger scientist. Thank you to my undergraduate advisor, Justin, for giving me so many rare opportunities as an undergraduate researcher and for support and incredible mentorship to this day. Thank you to all my family, Jolanta, Jan, and Patrick and friends, Tracy and Erin for their support throughout this time. Finally, I want to thank my partner Dan for his patience, support, friendship, and unconditional love over the years. You have been there during all of the highs and lows and encouraged me at every step along the way. You inspire me to be a better person, push me to never give up, and help me when times get really tough. We have grown incredibly during this time and the journey has been so much fun with you by my side. Thank you for all of the adventures, experiences, and everything in between. You make my world so much brighter.

TABLE OF CONTENTS

CHAPTER 1: INTRODUCTION TO LOCAL SIGNALING OF ANCHORED PROTEIN KINASES

CHAPTER 2: SUBCELLULAR DRUG TARGETING ILLUMINATES THE FUNCTIONS OF AURORA A AND POLO-LIKE KINASE 1 AT DISTINCT LOCATIONS DURING MITOSIS

CHAPTER 3: GRAVIN SIGNALING NETWORKS COORDINATE γ-TUBULIN ORGANIZATION AT MITOTIC SPINDLE POLES

CHAPTER 4: CONCLUSIONS AND FUTURE DIRECTIONS

APPENDIX

LIST OF FIGURES

CHAPTER 1 FIGURES

CHAPTER 2 FIGURES

CHAPTER 3 FIGURES

PREFACE

Portions of the text and data from this dissertation are reprinted (adapted) from the following works under fair use and/or with permission under the terms of the CC-BY License:

1. Bucko PJ, Lombard CK, Rathbun L, Garcia I, Bhat A, Wordeman L, Smith FD, Maly DJ, Hehnly H, and Scott JD. 2019. Subcellular drug targeting illuminates local kinase action. eLife 8:e52220.

2. Bucko PJ and Scott JD. 2021. Drugs that regulate local cell signaling: AKAP targeting as a therapeutic option. Annu Rev Pharmacol Toxicol, 61:2.1-2.19.

3. Bucko PJ, Garcia I, Manocha R, Bhat A, Worderman L, and Scott JD. *Under Review.* Gravin signaling networks coordinate γ-tubulin organization at mitotic spindle poles.

CHAPTER 1: INTRODUCTION TO LOCAL SIGNALING OF ANCHORED PROTEIN KINASES

1.1 INTRODUCTION

Cells respond to environmental cues by mobilizing signal transduction cascades that engage protein kinases, protein phosphatases, and other signaling effectors. Accordingly, correct organization of these enzymes in space and time enables the efficient and precise transmission of chemical signals (Sutherland 1972). Compartmentalization of signaling components within distinct subcellular environments is achieved by anchoring, adapter, and scaffold proteins, which serve as platforms for the assembly and maintenance of multi-enzyme complexes (Scott and Pawson 2009). A-kinase anchoring proteins (AKAPs) are a family of protein scaffolds that are defined by their ability to bind the protein kinase A (PKA) holoenzyme and tether other signaling molecules (Scott, Dessauer, and Tasken 2013; Tasken and Aandahl 2004; Wong and Scott 2004). While protein kinase inhibitor drugs are powerful research tools for elucidating signaling events, existing methods for delivering these molecules limits investigation of protein kinases at distinct microenvironments (Ferguson and Gray 2018). Thus, the ability of AKAPs to associate with intracellular membranes or organelles affords an opportunity to exploit subcellular targeting as a means to direct drugs to particular pools of enzymes.

1.2 AKAPs

AKAPs are a structurally diverse but functionally related family of signal organizing elements encoded by over 50 human genes (Langeberg and Scott 2015; Gabrovsek et al. 2017). These anchoring proteins share three common features (Figure 1). First, AKAPs associate with PKA via a docking and dimerization (D/D) domain (Carr et al. 1991; Newlon et al. 1997). The PKA holoenzyme is a serine/threonine protein kinase that exists as a tetramer composed of a regulatory (R) subunit dimer and two catalytic (C) subunits. The R subunits, encoded by four genes (RIα, RIβ, RIIα, or and RIIβ), and the three catalytic C subunit isoforms (Cα, Cβ, or Cγ) arrange into either type I PKA or type II PKA holoenzymes (reviewed in (Taylor et al. 2012)). Type I PKA contains RI subunits and is less often compartmentalized (Corbin, Keely, and Park 1975). Type II PKA is the predominant form known to interact with AKAPs (Carr et al. 1992). The AKAP's amphipathic helix forms a binding surface for the R subunit dimer that constrains PKA action to within 200–400 Åangstroms of the AKAP (Smith et al. 2017; Smith et al. 2013). The first AKAP identified, microtubule-associated protein 2 (MAP2), was originally isolated from bovine brain microtubule preparations as a type II PKA interactor (Theurkauf and Vallee 1982). Since then, numerous AKAPs have been discovered by using RII overlays, a biochemical technique for detecting RII subunit-binding proteins (Carr et al. 1991). Subsequently, RI binding and dual-specificity (capable of binding both RI and RII) AKAPs have been characterized (Huang et al. 1997; Kovanich et al. 2010; Means et al. 2011). A second common feature of AKAPs is that they contain a subcellular localization domain that directs them to specific regions within cells (Esseltine and Scott 2013). This interaction allows AKAPs to constrain cell signaling within defined microdomains (Figure 2). For this reason, single nucleotide polymorphisms and genetic lesions in AKAPs not only alter kinase anchoring but can also disrupt the subcellular targeting (Smith et al. 2018). A third feature that most AKAPs possess is the ability to form complexes with other signaling molecules such as kinases, phosphatases, adenylyl cyclases, and phosphodiesterases (Dessauer 2009; Lomas and Zaccolo 2014). This scaffolding function allows for the efficient transmission of a chemical signal within a defined subcellular locale while insulating the effect to the vicinity of specific substrates (Langeberg and Scott 2015; Esseltine and Scott 2013; Zaccolo et al. 2000; Schleicher and Zaccolo 2018). For this latter reason, these macromolecular complexes can be thought of as "AKAP signaling islands" (Smith et al. 2017).

1.3 GRAVIN

Originally identified as an autoantigen in serum from patients with myasthenia gravis (Gordon et al. 1992), Gravin (AKAP12/AKAP250/SSeCKS), was later discovered to be a scaffolding protein that clusters type II PKA with PKC (Nauert et al. 1997). Its role in migration, cell proliferation, and metastasis has been investigated over the years (Gelman 2010; Muramatsu et al. 2017). Gravin maps to 6q24–25.2, a deletion hotspot in a variety of cancers, and its expression is often downregulated in cancer cell lines and tissue (Gelman 2012). Likewise, lower levels of Gravin in tumor stroma from patients with breast and prostate cancer suggest that this scaffold attenuates secretion of tumor chemoattractants from neighboring fibroblasts to suppress metastasis (Muramatsu et al. 2017). In contrast, elevated Gravin levels in ovarian cancer cells correlate with poor prognosis (Bateman et al. 2015). These divergent results suggest that the role of Gravin as a tumor suppressor versus as a driver of oncogenesis may depend on the particular type of cancer and relative expression of the protein in a specific tissue. It is also likely that epigenetic regulation through promoter hypermethylation may result in varied Gravin expression (Gelman 2012; Wilhelm et al. 2016). Recent phosphoproteomics and peptide array kinomics approaches have identified Gravin as a potential prognostic biomarker for high-grade meningiomas. These data suggest that tumor progression, invasiveness, and recurrence correlate with lower Gravin levels (Parada et al. 2018). Suppression of the Raf/MEK/ERK mitogenic pathway is thought to be one mechanism by which Gravin inhibits cancer cell invasiveness, but its ability to scaffold PKC may also influence susceptibility to oncogenic transformation (Su et al. 2010; Akakura et al. 2010). Recent evidence suggests that inactivating mutations in certain PKC isoforms are cancer-driving events (Newton and Brognard 2017). However, more studies are necessary to clarify the role of Gravin-anchored PKC in these processes. Recently, depletion of Gravin has been linked to defective mitotic signaling in cancer cell lines and germ-line derived human seminoma samples (Hehnly et al. 2015). This supports previous studies that implicate Gravin in controlling mitotic progression (Gelman 2010). Additionally, the discovery that this anchoring protein can coordinate two mitotic kinases, Aurora A and polo-like kinase 1 (Plk1), further suggests that Gravin may play a critical role in safeguarding events during cell division (Canton et al. 2012; Hehnly et al. 2015; Colicino et al.

2018; Bucko et al. 2019). Thus, gaining greater mechanistic insight into how Gravin signaling islands coordinate different aspects of mitogenic signaling and cell division may aid in the development of novel anti-cancer therapies.

1.4 THE ROLE OF GRAVIN-ANCHORED KINASES IN MITOSIS

Overview of Mitosis

In order to generate copies of themselves cells must undergo a highly complex process called mitosis. Just prior to mitosis the cell duplicates its genetic material as well as a key organelle called the centrosome. The centrosome forms two structurally distinct centrioles that are surrounded by an amorphous “cloud” of protein, or pericentriolar material (PCM) (Nigg and Stearns 2011). During a process called centrosome maturation, the centrosome acquires a mass of proteins and initiates the nucleation of microtubules to drive the formation of the microtubule-based mitotic spindle (Gupta and Pelletier 2017). Concurrently, the centrosome organizes a vast array of scaffold and signaling proteins near the centrioles and along the growing spindle to prepare the cell for its journey through mitosis (Nigg and Stearns 2011). Following this maturation step, the two centrioles move to opposite sides of the cell, driving the formation of a bipolar mitotic spindle (Wang, Jiang, and Zhang 2014). These preliminary events facilitate mitotic entry (cell transition from G2 into M phase) and are highly dependent on the activity of various protein kinases such as the “master regulator” of mitosis, cyclin-dependent kinase 1 (CDK1), as well as downstream players such as Aurora A kinase and polo-like kinase 1 (Plk1), (Asteriti, De Mattia, and Guarguaglini 2015; Barr, Sillje, and Nigg 2004; Lens, Voest, and Medema 2010). These proteins become upregulated at the G2/M transition and ultimately dictate how successfully a cell progresses through mitosis (Lens, Voest, and Medema 2010). Coordinated localization and activation of mitotic protein kinases allows for the correct segregation of DNA into two new daughter cells (Pines and Rieder 2001). However, if any of the aforementioned steps become dysregulated, cell abnormalities, impaired tissue development, and even cancer can ensue (Levine and Holland 2018).

Protein phosphorylation during mitosis

To ensure proper orchestration of cell-division events, mitotic enzymes are tightly controlled by reversible protein phosphorylation (Welburn and Jeyaprakash 2018). This is accomplished by the balanced interplay between phosphate addition to a substrate by kinases and removal by phosphatases (Gelens et al. 2018). While there are numerous players that ensure the fidelity of mitosis, Aurora A and Plk1 are two serine/threonine kinases that play very important roles throughout the mitotic cycle (Joukov and De Nicolo 2018). Moreover, we recently discovered that the AKAP Gravin forms a complex with Aurora A and Plk1 during mitosis to provide spatiotemporal control of various events during cell division (Hehnly et al. 2015). For this reason, these protein kinases will be the focus of the following sections.

Aurora A kinase

Aurora A is a major regulator of cell division (Vader and Lens 2008; Nikonova et al. 2013). It plays a key role in the maturation and separation of the centrosomes, drives assembly of the bipolar mitotic spindle, triggers entry into mitosis, and assists in various other cell cycle events (Hannak et al. 2001; Cowley et al. 2009; Marumoto et al. 2002). This protein kinase localizes to the centrosome and mitotic spindles to help facilitate these processes (Kufer et al. 2002; Joukov et al. 2010). Though it was originally believed that Aurora A predominantly functions at these two locations, more recently it has been implicated in stabilizing microtubule-kinetochore attachments at kinetochores (Chmatal et al. 2015; Ye et al. 2015; DeLuca et al. 2018). While it is now well established that Aurora A is required for the initiation, progression through, and completion of mitosis, overexpression of Aurora A leads to a number of cellular phenotypes including monopolar spindles, aneuploidy (abnormal number of chromosomes), increased resistance to apoptosis, and failure to meet cell cycle checkpoints (Glover et al. 1995; Vader and Lens 2008; Nikonova et al. 2013). In recent years, the discovery of Aurora A overexpression in various cancers including ovarian, colorectal, and breast has suggested a role for this kinase in cancer development and progression (He et al. 2015; Koh et al. 2017; Cirak et al. 2015).

Polo-like kinase 1

Polo-like kinase 1 (Plk1) localizes to centrosomes, kinetochores, and the midbody to coordinate various aspects of cell division (Joukov and De Nicolo 2018). This kinase interacts with its binding partners through the polo-box domain (PDB), which consists of two polo-box regions, that allow it to recognize and bind to substrates that have been primed by phosphorylation (Elia, Cantley, and Yaffe 2003; Lee et al. 2008). Plk1 regulates early and late mitotic events including mitotic entry, chromosome maturation, bipolar spindle formation, and chromosome congression and segregation (Gheghiani et al. 2017; Sunkel and Glover 1988; Sumara et al. 2004; Kang et al. 2006). Consequently, abrogation of Plk1 activity has been associated with mitotic delay, monopolar spindles, and micronuclei formation (a consequence of missegragated chromosomes) (Lenart et al. 2007; Lera et al. 2016) Since Plk1 is extensively involved in coordinating various events during mitosis, perhaps it is not surprising that elevated expression of this kinase has been documented in non-small cell lung, breast, ovarian, thyroid, and colorectal cancers (Takai et al. 2005).

Drugging Aurora A and Plk1 to elucidate function

Aurora A is activated through autophosphorylation of threonine 288 and then phosphorylates Plk1 on threonine 210 to increase catalytic activity (Littlepage et al. 2002; Macurek et al. 2008; Seki et al. 2008). Accordingly, kinase inhibitor drugs that block this activity have been paramount to elucidating how Aurora A and Plk1 function in normal and pathological states (Asteriti et al. 2014; Lenart et al. 2007). Moreover, small-molecule kinase inhibitor drugs are a major class of chemotherapeutic agents; therefore, the targeting of kinases for cancer treatment represents a unique approach for developing novel drug therapies (Fabbro et al. 2012; Hoelder, Clarke, and Workman 2012). For Aurora A and Plk1, the anti-tumor effects of MLN8237 and BI2536 (inhibitors of Aurora A and Plk1, respectively) have been documented in tumor cell lines and xenograft mouse models (Manfredi et al. 2011; Steegmaier et al. 2007). These studies implicate both kinases as promising anti-mitotic cancer targets (Tang et al. 2017; Lee et al. 2015; Gutteridge et al. 2016).

Aurora A and Plk1 associate through a variety of scaffold and adapter molecules including Bora, Cep190, INCENP, and Gravin (Joukov and De Nicolo 2018; Hehnly et al. 2015). As a result, they share similar localization patterns and overlapping functions during various stages of the mitosis (Lens, Voest, and Medema 2010; Asteriti, De Mattia, and Guarguaglini 2015). Moreover, the spatial distribution and activity of protein kinases during this time is in constant flux which makes it challenging to elucidate the functions to individual enzymes (Bruinsma et al. 2015). Specifically, it is difficult to decipher the unique contributions of Aurora A and Plk1 at distinct subcellular locations such as mitotic centrosomes and kinetochores (Li et al. 2015; Lera et al. 2016). Current approaches in which small-molecule kinase inhibitor drugs are used to ascribe function to Aurora A and Plk1 provide important insight into the global roles of these kinases inside the cell (Asteriti et al. 2014; Lenart et al. 2007; Cheng et al. 2018). However, the indiscriminate distribution of such traditional inhibitor drugs limits our ability to resolve how individual mitotic enzymes function at distinct organelles (Scutt et al. 2009).

1.5 DECIPHERING CONTRIBUTIONS OF KINASES TO LOCAL SIGNALING EVENTS

Targeting the AKAP interaction

One way to gain mechanistic insight into how kinase activity at a specific location drives a cellular process is to study the molecular scaffolds that form complexes with enzymes (Langeberg and Scott 2015). A unique avenue for exploring the intricacies of AKAP-mediated signaling could involve disrupting the binding of AKAP-interacting proteins (Figure 3). For example, disrupting Aurora A and Plk1 function at Gravin complexes can provide mechanistic clues into how these mitotic kinases work at centrosomes (Hehnly et al. 2015; Colicino et al. 2018). The concept of targeting AKAP-enzyme interfaces may not only help decipher local signaling events but can also aid in the development novel therapeutics (Calejo and Tasken 2015; Kennedy and Scott 2015; Troger et al. 2012). Peptide sequences that target the PKA/AKAP interface have traditionally been used to monitor local PKA phosphorylation events (reviewed by (Kennedy and Scott 2015; Deak and Klussmann 2016)). The first such reagent was the 24-residue peptide Ht31, which remains among the best-characterized disruptors of the PKA/AKAP interaction (Carr and Scott 1992). Since then, Ht31 has been paramount in elucidating how the PKA/AKAP interaction drives normal cellular processes such as modulation of synaptic ion channels, insulin secretion, ocular lens transparency, and communication between adjacent cells via gap junctions (Rosenmund et al. 1994; Gold et al. 2012; Dukic et al. 2017). Similarly, small-molecule and peptide disruptors have been reported to block AKAP binding to protein phosphatase 2B (PP2B) and protein phosphatase 1 (PP1) (Nygren and Scott 2016). These reagents provide opportunities for monitoring local protein dephosphorylation. More recently, strategies for blocking interactions of AKAPs with other signaling effectors including ion channels, such as TRPV4, and small GTPases, like RhoA, hold equal promise for deciphering local signaling events (Mack and Fischer 2017; Schrade et al. 2018). While novel reagents that alter interactions with additional AKAP partners (e.g., protein kinases, adenylyl cyclases and phosphodiesterases) are likely to be developed in the years to come, to date, very few such compounds are available.

Directing kinase inhibitor drugs to individual kinases

Employing small-molecule kinase inhibitors that dampen activity is a preferred experimental tool for establishing the cellular roles of individual protein kinases (Ferguson and

Gray 2018). However, traditional drug-delivery approaches are limited in their ability to decode how signaling events are regulated by specific kinases (Klaeger et al. 2017). Chemical-genetics methods in which bulky purine analogs are designed to inhibit engineered analog-sensitive kinases have fewer off-target effects than traditional ATP-competitive drugs (Bishop et al. 2000). More recently, these tools have been effective in disentangling the roles of individual protein kinases, including Aurora A and Plk1 during mitosis (Koch et al. 2012; Lera et al. 2016). Drug-resistant forms of Aurora A and Plk1 have also been vital to resolving the molecular targets of promiscuous inhibitor drugs and for ascribing kinase-specific functions (Scutt et al. 2009; Sloane et al. 2010). Finally, antibody mimetics that direct promiscuous inhibitor drugs to specific kinases offer yet another means for studying the contributions of individual enzymes (Gower et al. 2016). However, while these chemical-genetic tools advance our understanding of kinase-mediated signaling events, existing methods are limited in their ability to discriminate the functions of individual signaling enzymes at distinct organelles (Jones and Jallepalli 2016). Thus, to elucidate local kinase action there is a need for new pharmacological strategies that inhibit kinases at specific subcellular locations (Figure 3C).

Elucidating kinase action at distinct subcellular locations

This thesis work uncovers how the Gravin-anchored protein kinases, Aurora A and Plk1, coordinate distinct signaling events at specific subcellular locations during mitosis. In Chapter 2, I describe a new chemical biology tool called LoKI (local kinase inhibition) that I develop for inhibiting the activity of protein kinases at specific mitotic structures. This approach utilizes genetically-encoded platforms that contain localization sequences, including AKAP-targeting domains, which are fused to a self-labeling SNAP-tag (Keppler et al. 2003). Using chemically modified inhibitors of Aurora A and Plk1 that can covalently attach to the localized SNAP-tag, I can effectively probe local kinase action at centrosomes and kinetochores during mitosis. Specifically, I show that inhibition of centrosome-associated pools of Aurora A and Plk1 disrupts phosphorylation of individual substrates, produces mitotic spindle defects, and prolongs mitosis. I also discover that inhibition of kinetochore-associated Aurora A diminishes phosphorylation of microtubule-kinetochore components. Moreover, I explore the utility of this system in multiple human cell lines as well as in developing zebrafish embryos and demonstrate that this approach can be used to study local signaling at other organelles such as the plasma membrane and mitochondria. In Chapter 3, I examine the role of Gravin-anchored Plk1 signaling in coordinating γ-tubulin organization at mitotic centrosomes. First, I discover that Gravin loss impairs the accumulation and asymmetric distribution of γ-tubulin at mitotic spindle poles. Second, I use LoKI to explore how centrosome-localized Plk1 activity drives this process. Together, the studies in Chapters 2 and 3 extend our understanding of several key protein kinase signaling events during mitosis and provide mechanistic insight into the spatiotemporal control of these processes.

Elucidating how molecular scaffolds organize signaling enzymes provides mechanistic clues into how cellular processes are coordinated in space and time. Additionally, designing pharmacological tools that target inhibitor drugs to specific subcellular locations deciphers local kinase action. In my studies, I use these complementary approaches to uncover how Aurora A and Plk1 function at distinct mitotic structures. While the utility of LoKI platforms has yet to be fully realized, organellar targeting of well-characterized drugs via AKAPs offers a new means for advancing the investigation of protein kinases at specific locations. Ultimately, by decoding how individual enzymes within distinct microenvironments contribute to signaling events, we will gain greater insight into how local kinase action underlies complex biological processes.

1.6 FIGURES

Figure 1:

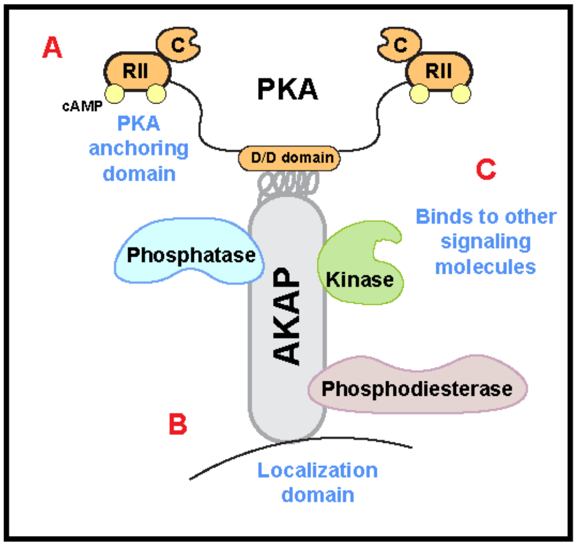

Figure 1 Legend: A schematic of a prototypic A-kinase anchoring protein (AKAP) signaling island. (**A**) The amphipathic helix interacts with the docking and dimerization (D/D) domain on the R-subunit of protein kinase A (PKA). (**B**) Subcellular targeting of AKAPs proceeds through specialized targeting domains that interact with organelles or cellular membranes. (**C**) AKAPs compartmentalize various signaling molecules.

Figure 2:

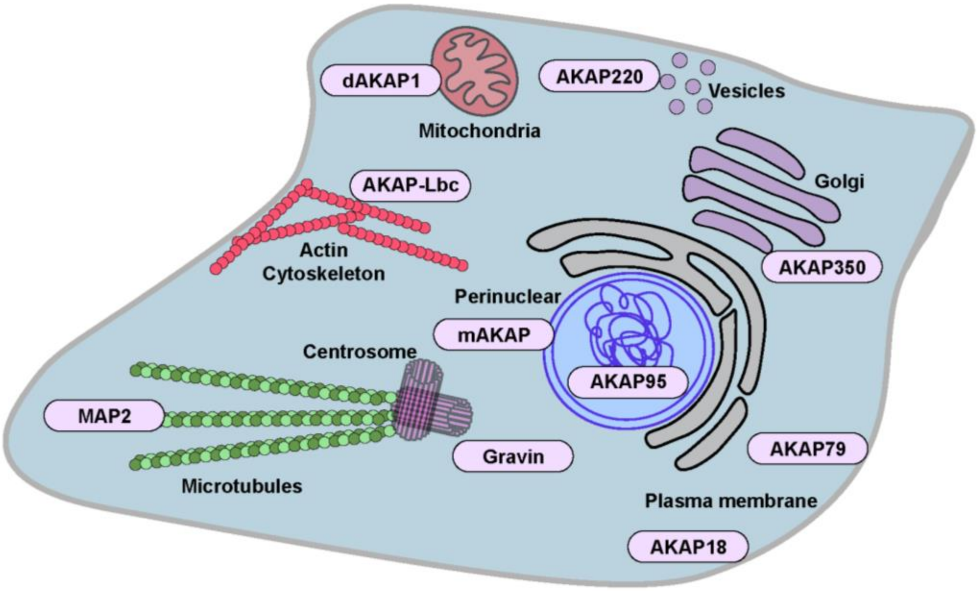

Figure 2 Legend: Subcellular locations of key A-kinase anchoring proteins (AKAPs). Schematic of a prototypic cell showing the subcellular locations of well-characterized AKAPs tethered to membranes or intracellular organelles.

Figure 3:

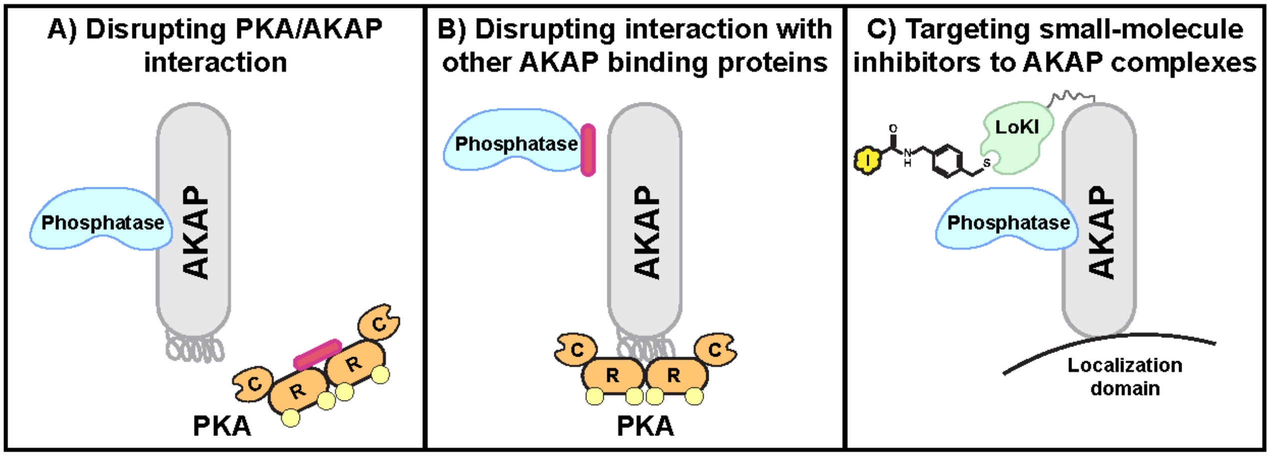

Figure 3 Legend: Reagents that manipulate A-kinase anchoring protein (AKAP) signaling. (**A**) Disruption of protein kinase A (PKA) holoenzyme anchoring involves a variety of peptides and small-molecules that target the interface between AKAPs and R-subunit dimers. (**B**) Displacement of phosphatases from AKAP signaling islands is mediated by peptides that mimic targeting motifs on the surface of the anchoring protein. (**C**) Exploitation of AKAP localization domains to deliver kinase inhibitor drugs to defined subcellular locations.

CHAPTER 2: SUBCELLULAR DRUG TARGETING ILLUMINATES THE FUNCTIONS OF AURORA A AND POLO-LIKE KINASE 1 AT DISTINCT LOCATIONS DURING MITOSIS

2.1 ABSTRACT

Deciphering how signaling enzymes operate within discrete microenvironments is fundamental to understanding biological processes. A-kinase anchoring proteins (AKAPs) restrict the range of action of protein kinases within intracellular compartments. We exploited the AKAP targeting concept to create genetically encoded platforms that restrain kinase inhibitor drugs at distinct subcellular locations. Local Kinase Inhibition (LoKI) allows us to ascribe organelle-specific functions to broad specificity kinases. Using chemical genetics, super resolution microscopy, and live-cell imaging we discover that centrosomal delivery of Polo-like kinase 1 (Plk1) and Aurora A (AurA) inhibitors attenuates kinase activity, produces spindle defects, and prolongs mitosis. Targeted inhibition of Plk1 in zebrafish embryos illustrates how centrosomal Plk1 underlies mitotic spindle assembly. Inhibition of kinetochore-associated pools of AurA blocks phosphorylation of microtubule-kinetochore components. This versatile precision pharmacology tool enhances investigation of local kinase biology.

2.2 INTRODUCTION

Protein kinase inhibitor drugs are an emerging class of therapeutics for a variety of clinical indications (Ferguson and Gray 2018). These small molecules are also powerful research tools that can be used to discover new aspects of kinase signaling (Caunt et al. 2015). While "*drugging*" individual kinases can establish their role in cellular events, this global approach cannot discriminate where or when these signaling enzymes operate inside the cell. Thus, designing pharmacological strategies that influence the spatial and temporal action of kinases is at the frontier of precision medicine.

Polo-like kinase 1 (Plk1) and Aurora A (AurA) are important regulators of cell division (Barr, Sillje, and Nigg 2004; Combes et al. 2017; Lens, Voest, and Medema 2010). Accordingly, ATP-competitive drugs that block their activity, such as BI2536 and MLN8237, ascribe functions to these kinases and are promising anticancer therapies (Steegmaier et al. 2007; Tang et al. 2017; Lenart et al. 2007; Asteriti et al. 2014; Manfredi et al. 2011). However, elucidating the individual spatial and temporal actions of Plk1 and AurA remains challenging as these enzymes continually change their location and activity throughout mitosis (Bruinsma et al. 2015; Joukov and De Nicolo 2018; Lera et al. 2016). As a result, global drug delivery strategies mask the unique contributions of each kinase at distinct mitotic structures. Moreover, standard drug regimens that saturate dividing cells with these compounds may increase off-target effects and toxicity (Klaeger et al. 2017).

Plk1 and AurA have been implicated in the control of mitotic progression (Barr, Sillje, and Nigg 2004; Combes et al. 2017; Lens, Voest, and Medema 2010). The anchoring protein Gravin/AKAP12 participates in this process by forming a macromolecular complex with these enzymes (Hehnly et al. 2015). A-kinase anchoring proteins (AKAPs) are scaffolding proteins that limit the scope of cell signaling events at distinct cellular locations (Scott and Pawson 2009; Langeberg and Scott 2015; Esseltine and Scott 2013). For example, anchored protein kinase A action is constrained to within 200-400 angstroms of the AKAP (Smith et al. 2013; Smith et al. 2017). This has led to the formulation of a signaling island model where catalytic activity of anchored kinases is restricted to the immediate vicinity of select substrates (Scott and Pawson 2009; Langeberg and Scott 2015; Esseltine and Scott 2013). Likewise, anchoring of Plk1 and AurA occurs on a phosphorylated species of Gravin at Threonine 766 (Canton et al. 2012; Hehnly et al. 2015; Colicino et al. 2018). Consequently, loss or disruption of this scaffold abrogates Plk1 and AurA organization at centrosomes and promotes mitotic delay (Hehnly et al. 2015). Yet, an outstanding question that remains is exactly how do centrosome-localized pools of Gravin-anchored Plk1 and AurA coordinate mitotic signaling events.

In the present study we first establish that Gravin is required for localizing active pools of Plk1 and AurA at mitotic centrosomes. We then develop a novel chemical-biology tool, LoKI (**Lo**calized **K**inase **I**nhibition), to probe the actions of Plk1 and AurA at defined subcellular locations. Finally, we demonstrate that local inhibition of Plk1 and AurA kinases at centrosomes and kinetochores disrupts substrate phosphorylation, spindle organization, and mitotic duration. Together, these studies decipher how activities of individual kinases at precisely defined microenvironments contribute to the global signaling events that underlie mitosis.

2.3 RESULTS

Gravin loss prolongs mitosis and perturbs accumulation of Plk1 and AurA at centrosomes

Gravin depletion via shRNA-mediated knockdown perturbs mitotic progression (Hehnly et al. 2015). However, whether cells that completely lack Gravin also exhibit prolonged mitoses is unknown. Time-lapse video microscopy was used to monitor mouse embryonic fibroblasts (MEFs) from wild-type and Gravin knockout (KO) mice (Figure 1A, Figure 1-figure supplement 1A). Live-cell imaging of wild-type MEFs expressing GFP-tagged histone 2B established a baseline mitotic duration (nuclear envelope breakdown to anaphase onset) as 32.6 minute (Figure 1B). In contrast, mitosis was delayed by 11.9 minutes in Gravin KO cells (Figure 1B). These data further establish that Gravin promotes timely progression of cells through mitosis (Gelman 2010).

Gravin is required for organization of Plk1 and AurA at mitotic centrosomes (Hehnly et al. 2015). Whether Gravin loss reduces active pools of Plk1 and AurA at this location remains unclear. To test this we explored whether activity of centrosome-localized Plk1 and AurA is perturbed in cells lacking Gravin. We examined pT210-Plk1 and pT288-AurA immunofluorescence (measures of Plk1 and AurA activity, respectively) in HEK293 cells stably expressing a control or Gravin shRNA (Figure 1C, D). Gravin depletion reduced immunofluorescence of pT210-Plk1 to 80.2% of control shRNA-expressing cells (Figure 1C, E).

Strikingly, pT288-AurA signal in Gravin-depleted cells dropped to 58.5% of control cell immunofluorescence (Figure 1D, F). These findings reveal that Gravin is required for localizing active pools of Plk1 and AurA at mitotic centrosomes.

LoKI platforms direct kinase inhibitor drugs to specific subcellular locations

To decipher how Gravin-associated pools of Plk1 and AurA coordinate mitotic signaling events we needed to selectively target drugs to this location without disrupting the Gravin-Plk1-AurA macromolecular complex. During interphase Gravin is dispersed throughout the cell (Figure 1G, Figure 1-figure supplement 1B). In mitosis, however, pT766-Gravin accumulates at centrosomes, a major hub of Plk1 and AurA signaling (Figure 1G, Figure 1-figure supplement 1B). This provided the impetus to pharmacologically inhibit mitotic kinases at centrosomes (Figure 1H). A key advance in our studies came with the development of the LoKI tool which allows us to target kinase inhibitor drugs to specific subcellular locations. We fused a **p**ericentrin **A**KAP450 **c**entrosomal-**t**argeting (PACT) domain (Gillingham and Munro 2000) to a SNAP-tag moiety which can be covalently labeled with chloropyrimidine (CLP)-linked substrates inside cells (Keppler et al. 2003) (Figure 2A). A CLP-conjugated analog of BI2536 (CLP-BI2536) was generated to selectively target Plk1 (Figure 2A, B, Figure 2-figure supplement 1A). *In vitro* kinase activity measurements demonstrated that CLP-BI2536 potently inhibits Plk1 (IC_{50} = 49 ± 26 nM; Figure 2C, Figure 2-figure supplement 1B).

To generate stable cell lines, U2OS osteosarcoma cells were infected with lentiviral constructs encoding the SNAP-PACT moieties fused to an mCherry reporter (Figure 2-figure supplement 1C). Inducible protein expression was accomplished by a doxycycline-inducible promoter (Figure 2-figure supplement 1D). Immunoblot detection of mCherry-SNAP-PACT persisted up to 4 hours upon removal of doxycycline (Figure 2-figure supplement 1E). As anticipated, mCherry-SNAP-PACT associates with centrosomes during interphase and mitosis (Figure 2-figure supplement 1F). Super-resolution structured illumination (SIM) imaging revealed that the SNAP-PACT construct (magenta) was labeled by CLP-fluorescein (yellow) at centrosomes (Figure 2D, E). Counterstaining with α-tubulin (green) revealed the mitotic spindle and DAPI (blue) detected DNA (Figure 2D). Collectively these results demonstrate that centrosomal targeting of SNAP-PACT creates a platform for the delivery of CLP-conjugates (Figure 2-figure supplement 1G). This new drug targeting method is herein referred to as **LoKI-on** (**Lo**calized **K**inase **I**nhibition-**on**). In parallel, a LoKI-off vector containing an inactivating mutation (C144A) in SNAP-tag was constructed (Figure 2-figure supplement 1H). LoKI-off is unable to incorporate CLP-conjugates and serves as the control platform (Figure 2-figure supplement 1H).

Pulse-chase experiments were used to determine how efficiently CLP-BI2536 labeled SNAP-PACT. U2OS cells were treated with CLP-BI2536 (over a range of concentrations) to block CLP-rhodamine conjugation (Figure 2F**.** Incubation with 250 nM CLP-BI2536 for 4 hours at 37°C was defined as the optimal drug regimen (~50% labeling of SNAP-PACT; Figure 2F, Figure 2-figure supplement 2A, B). Next, we measured the pT210-Plk1 immunofluorescence signal as an index of active kinase (Lee and Erikson 1997) (Figure 2-figure supplement 3A, B). In mitotic cells expressing LoKI-off, incubation with 250 nM CLP-BI2536 reduced pT210-Plk1 immunofluorescence to 58.1% of DMSO-treated controls (Figure 2G, I). Strikingly, the pT210-Plk1 signal was reduced to 21.4% in cells expressing LoKI-on (Figure 2H, I). This trend persisted with lower CLP-BI2536 concentrations and even after a 1-hour washout of drug (Figure 2 I, J). Further validation confirmed that the reduction of pT210-Plk1 does not result from a loss in total Plk1 protein at centrosomes (Figure 2-figure supplement 3C). Additional controls established that inducible expression of LoKI-on was necessary to attenuate the pT210-Plk1 signal (Figure 2-figure supplement 3D). Immunoblot analyses of nocodazole-synchronized cells collected via mitotic shake-off further support these findings (Figure 2-figure supplement 3E). Parallel analyses were conducted in HeLa and hTERT-immortalized RPE retinal pigment epithelial cells (Figure 2-figure supplement 3F-J). We note that due to clonal cell line differences between LoKI-off and

LoKI-on cells, baseline immunofluorescence signal was normalized to DMSO-treated controls (Figure 2-figure supplement 4). Collectively, these findings establish LoKI as a new pharmacological tool to selectively block Plk1 activity at centrosomes.

Targeting Plk1 inhibitor drugs to centrosomes perturbs early mitotic events

Correct assembly of bipolar spindles ensures the fidelity of chromosome segregation into daughter cells (Prosser and Pelletier 2017). Abrogation of Plk1 activity has been linked to mitotic spindle defects that include abnormal bipolar and monopolar structures (Sunkel and Glover 1988; Lane and Nigg 1996; Sumara et al. 2004) (Figure 3A). Spindle classification measurements were carried out to assess if centrosomal inhibition of Plk1 induces these morphological anomalies (Figure 3B). Analysis in U2OS cells revealed that application of CLP-BI2536 in LoKI-on cells increased the incidence of abnormal bipolar (green) and monopolar (purple) spindles by 24.6% as compared to LoKI-off controls (10.3%; Figure 3B, C, Figure 3-figure supplement 1A). More pronounced spindle defects were observed when local drug delivery experiments were repeated in RPE cells (Figure 3D, Figure 3-figure supplement 1B). Interestingly, local delivery of CLP-BI2536 did not further exacerbate defective spindle organization in Hela cells, which naturally exhibit a high incidence of aberrant spindles (Figure 3E, Figure 3-figure supplement 3C). Thus, targeting Plk1 inhibitor drugs to centrosomes promotes mitotic spindle defects in various cell types.

Spindle assembly relies on γ-tubulin, a protein that interacts with α/β-tubulin polymers (Moritz et al. 1995; Zheng et al. 1995). Plk1 phosphorylates pericentriolar substrates that coordinate γ-tubulin accumulation at mitotic centrosomes to facilitate microtubule nucleation (Lane and Nigg 1996; Haren, Stearns, and Luders 2009; Xu and Dai 2011) (Figure 3F). Accordingly, we monitored centrosomal accumulation of γ-tubulin in U2OS cell after application of CLP-BI2536 for 4 hours followed by a 1-hour washout (Figure 3G-I, Figure 3-figure supplement 1D). The γ-tubulin signal (yellow) accumulated at centrosomes in LoKI-off controls (Figure 3G, I).

However, γ-tubulin levels were drastically reduced when LoKI-on cells were exposed to the same drug regimen (Figure 3H, I). Amalgamated data from five independent experiments are presented (Figure 3I). These findings indicate that targeting CLP-BI2536 to centrosomes impairs accumulation of γ-tubulin at this location.

Targeting AurA inhibitors to centrosomes suppresses AurA activity

A versatile feature of the LoKI system is the ability to compartmentalize a variety of drug analogs. The AurA inhibitor MLN8237 was a logical candidate to highlight the broad applicability of this approach. CLP-MLN8237 was synthesized (Figure 4A, Figure 4-figure supplement 1A). *In vitro* kinase activity measurements demonstrated that CLP-MLN8237 potently inhibits AurA (IC_{50} < 9.5 nM; Figure 4B, Figure 4-figure supplement 1B). Cell-based characterization established that treatment with 100 nM CLP-MLN8237 for 4 hours at 37°C was sufficient to label ~50% of drug binding sites (Figure 4C). Next, we used immunofluorescent detection of pT288-AurA as an index of kinase activity (Figure 4-figure supplement 2A, B). In mitotic cells expressing LoKI-off, incubation with 100 nM CLP-MLN8237 reduced pT288-AurA immunofluorescence to 27.8% of DMSO-treated controls (Figure 4-figure supplement 2C). Importantly, the pT288-AurA signal was further reduced to 14.2% in cells expressing LoKI-on (Figure 4D, E). Thus, increasing the local concentration of MLN8237 enhances drug action by approximately 2-fold at this precise subcellular location. This data demonstrates the versatility of the LoKI system as a pharmacological platform to block distinct kinases that operate at mitotic centrosomes.

Combined Plk1 and AurA inhibiton at centrosomes more profoundly delays mitosis than global kinase inhibition

To investigate the coordinate activities of Plk1 and AurA at the centrosome (Asteriti, De Mattia, and Guarguaglini 2015) we took advantage of another feature of the LoKI-on platform, the ability to co-localize CLP-drug combinations via a dual SNAP conjugation moiety (Figure 4F).

Live-cell imaging of U2OS cells expressing GFP-tagged histone 2B (Figure 4G, Figure 4-figure supplement 2D) was used to calculate a baseline for mitotic timing (nuclear envelope breakdown to anaphase) as 35.1 minute (Figure 4H). Mitosis was delayed by 19.4 minutes when CLP-BI2536 (250 nM) and CLP-MLN8237 (100nM) were simultaneously applied to LoKI-off cells (Figure 4G, H). However, the same combination treatment prolonged mitosis 3-fold (59 min delay) when experiments were repeated in LoKI-on cells (Figure 4G, H). Moreover, the mitotic duration observed in LoKI-on cells after combination treatment extended beyond what was seen with either inhibitor alone (Figure 4-figure supplement 3A, B). These data accentuate the utility of LoKI-on as a means to direct drug combinations to defined cellular locations in space and time.

Implementation of LoKI in live zebrafish embryos implicates Plk1 activity at centrosomes in coordinating mitoses during early development

Zebrafish provide an excellent model organism to test local drug action using the LoKI system because their transparency simplifies imaging analysis (Zon and Peterson 2005). Zebrafish embryos were microinjected with mCherry-LoKI-on mRNA and allowed to develop for 5 hours until they reached ~50% epiboly (Figure 5A, B). Detection of mCherry fluorescence confirmed expression of the local drug-targeting construct (Figure 5B). Higher resolution imaging of fixed embryos confirmed accumulation of LoKI-on at centrosomes during interphase and mitosis (Figure 5-figure supplement 1A). Co-distribution of the SNAP moiety (magenta) with CLP-647 dye (yellow) confirmed assembly of the drug-targeting platform at centrosomes (Figure 5-figure supplement 1B). Microinjection of the Plk1 inhibitor adduct CLP-BI2536 (250nM) permitted local drug delivery. Live-cell imaging 5 hours post injection exposed a range of adverse mitotic phenotypes. Mitotic spindles were visualized using a microtubule binding protein, EMTB-3xGFP (Figure 5C). Multipolar spindles, spindle orientation defects, and prolonged mitoses were evident in drug-treated embryos expressing LoKI-on (Figure 5C). Fixed-cell imaging of whole embryos revealed intact microtubule organization and few mitotic cells in LoKI-off embryos treated with

CLP-BI2536 (Figure 5D). In contrast, drug-treated LoKI-on embryos exhibited microtubule abnormalities and a higher incidence of mitotic cells (Figure 5E). Fluorescent detection of the SNAP moiety confirmed centrosomal targeting of LoKI platforms (Figure 5D, E). Additional analyses correlated centrosomal inhibition of Plk1 with increased mitotic indices in LoKI-on embryos (Figure 5F). Conversely, control experiments in LoKI-off embryos showed that CLP-BI2536 had minimal effect, as indicated by a significantly higher proportion of interphase cells (Figure 5F). Thus, targeted delivery of kinase inhibitor drugs to mitotic centrosomes induces a range of adverse mitotic phenotypes in developing embryos relative to global drug application.

Targeting CLP-MLN8237 to kinetochores reveals that AurA-mediated Hec1 phosphorylation is a local event

Kinetochores are proteinaceous structures that ensure the proper attachment of spindle microtubules to the centromeric region of condensed chromatin (Hinshaw and Harrison 2018) (Figure 6A). To further demonstrate the versatility of the LoKI system, we utilized a targeting domain from the kinetochore protein Mis12 (Goshima et al. 2003) (Figure 6A). Inducible expression of the mCherry-tagged fusion was accomplished by a doxycycline-inducible promoter (Figure 6B, Figure 6-figure supplement 1A). Immunoblot detection of Mis12-LoKI-on persisted up to 4 hours upon removal of doxycycline (Figure 6-figure supplement 1B). Immunofluorescent staining revealed that mCherry-tagged Mis12-LoKI-on co-localized with centromeric DNA (anti-centromere antibodies (ACA), cyan) at kinetochores during mitosis (Figure 6C). Counterstaining with α-tubulin antibodies (green) revealed the mitotic spindle (Figure 6C). SIM imaging revealed that a CLP-dye (CLP-647, yellow) accumulated with the SNAP moiety (magenta) at kinetochores of Mis12-LoKI-on cells (Figure 6D). In contrast, recruitment of CLP-647 was not evident in Mis12-LoKI-off cells (Figure 6D). Line plot analyses of the CLP-647 signal in selected kinetochores emphasizes this result (Figure 6E). Pulse-chase experiments established that incubation with 100-250 nM of the AurA inhibitor adduct CLP-MLN8237 for 4 hours at 37°C was the optimal drug regimen (~50% of drug binding sites occupied; Figure 6F). Parallel, validation studies were performed with CLP-BI2536 (Figure 6-figure supplement 1C).

Roles for AurA at centrosomes and mitotic spindles are well documented (Nikonova et al. 2013). However, recent reports have implicated AurA as a modulator of microtubule attachment to kinetochores (Chmatal et al. 2015; Ye et al. 2015). At this location AurA phosphorylates serine 69 in Hec1, a subunit of the NDC80 complex (DeLuca et al. 2018). This local phosphorylation stabilizes microtubule-kinetochore interaction to safeguard chromosome segregation (DeLuca 2017). However, the proximity of centrosomes to kinetochores in early mitosis has hampered attempts to resolve the contribution of discrete AurA pools. Therefore, immunofluorescent detection of pS69-Hec1 served as an index for local AurA kinase activity at kinetochores (Figure 6G, H). As before, counterstaining for α-tubulin (green) and DNA (blue) revealed the mitotic spindle (Figure 6G, H). In cells expressing Mis12-LoKI-off, incubation with 100 nM CLP-MLN8237 caused a negligible decrease in pS69-Hec1 signal as compared to DMSO-treated controls (Figure 6G, I). Conversely, in Mis12-LoKI-on cells the pS69-Hec1 signal was reduced to 59.8% (Figure 6H, I). Representative heat maps further illustrate this phenomenon (Figure 6G, H). Importantly, the pS69-Hec1 signal at centrosomes was unaffected by drug treatments (Figure 6G, H, Figure 6-figure supplement 2A). Amalgamated data from three independent experiments reveal that this trend persisted even at higher concentrations (Figure 6I). Immunoblot analyses of nocodazole-synchronized cells collected via mitotic shake-off further support our findings (Figure 6-figure supplement 2B). Finally, when SNAP-PACT LoKI-expressing cells were used to sequester CLP-MLN8237 at centrosomes, we no longer observed a reduction in pS69-Hec1 signal at kinetochores (Figure 6-figure supplement 2C). These data further support a role for AurA at the kinetochore. Ultimately, our findings illustrate how LoKI platforms can be adapted to pharmacologically investigate kinase signaling at distinct subcellular locations within the mitotic cell.

2.4 DISCUSSION

Cells have evolved a highly organized architecture that is segregated into functionally distinct microenvironments (Figure 6J). However, traditional methods of drug delivery do not account for this exquisite degree of molecular organization. Conventional approaches flood cells with bioactive compounds, masking the unique contributions of individual kinases at distinct subcellular locations. Although it is well established that Plk1 and AurA coordinate various aspects of cell division, current drug-targeting strategies limit our ability to decode the spatiotemporal regulation of these events (Barr, Sillje, and Nigg 2004; Combes et al. 2017; Lens, Voest, and Medema 2010). Studying molecular scaffolds that form complexes with these key mitotic enzymes provides important mechanistic insight into how these processes are coordinated (Figure 1; (Hehnly et al. 2015)). Moreover, designing pharmacological tools that restrict the spatial and temporal action of kinase inhibitor drugs is paramount to deciphering local kinase action. In this study, we discovered that the anchoring protein Gravin is required for organizing active pools of Plk1 and AurA at centrosomes (Figure 1C, D). These data support previous findings in which Gravin loss led to increased Plk1 mobility and aberrant CEP215 phosphorylation (Canton et al. 2012; Hehnly et al. 2015; Colicino et al. 2018). Thus, we suggest that Gravin constrains enzymes in a signaling island to provide spatiotemporal control of kinase activity. Conversely, depletion of this anchoring protein alters Gravin-Plk1 and Gravin-AurA protein-protein interactions which underlie healthy cellular function. This further emphasizes a need for designing strategies that inhibit kinase activity locally. For this reason, we developed a novel chemical-biology tool, LoKI, to more precisely probe the actions of Plk1 and AurA at centrosomes and kinetochores. Previous work from Gower and colleagues utilized antibody mimetics to target promiscuous inhibitor drugs to specific kinases (Gower et al. 2016). Our strategy advances this technology by combining AKAP targeting domains with SNAP-tagging technologies. Additionally, we direct selective ATP-competitive inhibitors to specific subcellular locations to achieve local kinase inhibition. By combining biochemical approaches, quantitative imaging, and live-cell microscopy we reveal that local targeting of Plk1 and AurA kinase inhibitor drugs disrupts substrate phosphorylation, spindle organization, and mitotic duration more profoundly than global drug distribution. Thus organellar targeting of drugs offers a new means to advance the investigation of broad-spectrum kinases at precise locations.

Previous studies suggest that Plk1 phosphorylates pericentriolar substrates that coordinate γ-tubulin accumulation at mitotic centrosomes to facilitate microtubule nucleation (Lane and Nigg 1996; Haren, Stearns, and Luders 2009; Xu and Dai 2011). We advance this concept and extend these findings by demonstrating that centrosomal inhibition of Plk1 prevents accumulation of γ-tubulin and correct organization of bipolar mitotic spindles (Figure 3). Thus, by using the LoKI system we are able to definitively establish that Plk1 activity at mitotic centrosomes is a driver in these processes. Furthermore, the utility of LoKI drug targeting was underscored by our *in vivo* studies using zebrafish embryos. We provide evidence that embryos treated with centrosome-targeted Plk1 inhibitors have more microtubule abnormalities than those treated with a non-localized inhibitor (Figure 5C-E). These data implicate centrosomal-localized pools of Plk1 in coordinating mitotic events such as spindle organization and mitotic progression during early zebrafish development. In a broader context, we show that local targeting of Plk1 inhibitors in developing organisms offers an innovative precision technique to probe local drug action.

Another key advance in our studies came with the discovery that AurA-mediated Hec1 phosphorylation is a spatially-coordinated event that occurs at kinetochores. We provide quantitative imaging (Figure 6G-I, Figure 6-figure supplement 2C) and biochemical (Figure 6-figure supplement 2B) data that implicates AurA activity at this mitotic substructure. Although this kinase was originally thought to reside exclusively at centrosomes and mitotic spindles, our findings extend recent evidence for the existence of an AurA pool at kinetochores (DeLuca 2017). We reveal that kinetochore-targeted MLN8237 reduces pS69-Hec1 signal more drastically than globally distributed drug (Figure 6H-I). Our data suggests that even during prometaphase, when kinetochores may encounter centrosome-associated AurA, this phosphorylation is solely a kinetochore-associated event. Furthermore, when we target the AurA inhibitor to centrosomes and measure pS69-Hec1 at kinetochores we no longer see a loss of pS69-Hec1 signal (Figure 6-figure supplement 2C). Thus, we show that centrosome-associated AurA is not likely responsible for this phosphorylation event as has been previously suggested (Chmatal et al. 2015; Ye et al. 2015). More importantly, these findings uncover that S69-Hec1 phosphorylation is a local event that depends on AurA activity at kinetochores. This allows us to postulate that isolated pockets of AurA may act independently and concurrently to orchestrate complex cellular events.

The versatility of this new chemical-biology platform is demonstrated in three ways. First, this approach works in a variety of cell types and microinjection of LoKI mRNA into live zebrafish embryos permits local drug targeting *in vivo* (Figure 5). We foresee that LoKI platforms will be adapted to acutely probe local signaling in other genetically tractable organisms. Second, while derivatized Plk1 and AurA drugs delineate roles for each mitotic kinase, conjugation of chloropyrimidine (CLP) to other ATP analogs offers a general method to synthesize localizable inhibitors for additional members of the kinome (Gower et al. 2016). However, it is worth noting that the reduced cell permeability of certain CLP-drug conjugates, including CLP-BI2536, may necessitate their use at approximately 10-fold higher concentrations than the unmodified drugs (Figure 2I versus Figure 2-figure supplement 3B, Figure 4E versus Figure 4-figure supplement 2B). Additionally, derivatization of certain inhibitors may sterically hinder their access to the ATP-binding pockets of some kinases or, as is the case of the PKA antagonist H89, the lack of a functional group prevents CLP derivatization. Third, plasma membrane and mitochondrial targeting domains from AKAP79 and dAKAP1 expand the repertoire of subcellular compartments reached by LoKI platforms (Figure 6J).

Although our strategy uncovers local contributions of anchored kinase pools within the cell, certain limitations to our current approach exist. For example, we treat cells for 4 hours with CLP-conjugated drug adducts to achieve sufficient inhibitor targeting (~50% of drug binding sites occupied; Figure 2F, Figure 6F). This is a relatively long time period in the context of measuring cell-cycle events. Likewise, in cells we find that high concentrations of CLP-drug (100 nM) are required to produce equivalent effects as 10 nM of non-derivatized MLN8237 (Figure 4E versus Figure 4-figure supplement 2B). We postulate that reduced cell permeability of certain CLP-drug conjugates may account for both of the aforementioned findings. As a result, this necessitates long incubation periods and application of higher concentrations of drug. Finally, it is possible that kinase inhibitor drugs directed to centrosomes have off-target effects at nearby structures such as spindle microtubules. We envision that future advancements of this platform would include photo-caged inhibitors that are inert until they are ready to be released at the site of desired inhibition (Ellis-Davies 2007). Employing this strategy would more strictly define the range of inhibitor action, provide another level of control to the LoKI system, and allow us to better delineate the effects of global versus local inhibition.

One exciting feature of our LoKI platform is the ability to co-localize CLP-drug combinations via a dual SNAP conjugation moiety (Figure 4F). Although in our study this allowed combined inhibition of Plk1 and AurA at centrosomes, we hope that future work will advance on our strategy and provide a system that utilizes multiple self-labeling enzymes to deliver distinct inhibitors to the same location. Employing orthogonal tagging systems such as CLIP-tag or Halo-tag in tandem with SNAP-tag could eliminate the possibility that CLP-BI2536 and CLP-MLN8237 compete for conjugation to the same targeting moiety. Nonetheless, by exploiting our knowledge of how AKAPs compartmentalize signaling enzymes we have developed tools that define the local kinase terrain at the angstrom level. This will allow investigators to probe local signaling events at a level of precision that has not been possible before.

2.5 METHODS

Reagents

A detailed list of reagents is presented in “Chapter 2 Key Resource Table” of Appendix

Plasmid constructs

SNAP, mCherry, eGFP, PACT, Mis12, AKAP79, and dAKAP1 components and were individually PCR amplified with overlapping ends and/or Gateway “att” sites and assembled using Gibson Cloning. Gateway cloning was carried out to subclone SNAP constructs into pLIX402 (a gift from David Root; Addgene plasmid #41394) for PACT and Mis12 studies or pcDNA3.1+ (Life Technologies) for AKAP79 and dAKAP1. To generate mutant SNAP, site-directed mutagenesis was performed with a QuikChange II XL kit (Aligent). GFP-H2B and EMTB-3xGFP constructs were used for live-cell imaging studies. Constructs were verified by Sanger sequencing.

Cell culture and virus generation

Cells used to generate stable cell lines in this study originated as follows: U2OS (purchased from ATCC), HeLa (from L. Wordeman lab and maintained in-house), and hTERT-RPE (from P. Jallepalli lab and maintained in-house). HeLa and hTERT-RPE cells were tested by STR at ATCC. Chang Liver cells, a HeLa contaminant, were detected in the HeLa line while hTERT-RPE cells were an exact match to ATCC cell line CRL-4000 (hTERT-RPE-1). U2OS, HeLa, and hTERT-RPE cells tested negative for mycoplasma contamination as assessed by the Universal Mycoplasma Detection Kit (ATCC 30-1012K). U2OS, HeLa, Control and Gravin shRNA HEK293 (Canton et al. 2012; Hehnly et al. 2015; Colicino et al. 2018), and immortalized MEF (generated as described in (Hehnly et al. 2015) and maintained in-house) cells were maintained in DMEM, high glucose and hTERT-RPE cells were maintained in DMEM/F-12, Hepes (Life Technologies) at 37°C and 5% CO2. All media was supplemented with 10% FBS. Infections for generation of stable SNAP cells were performed using lentiviral particles created in-house. In brief, SNAP pLIX402 vectors were transfected alongside pMD2.G and psPAX2 plasmids (gifts from Didier Trono; Addgene plasmid #12259 [RRID:Addgene_12259] and plasmid #12260 [RRID:Addgene_12260])) into HEK293 cells using Lipofectamine 2000 reagent (Invitrogen) in Opti-MEM® (Life Technologies) media. Virus-containing supernatant was collected, passed through a .45 µm filter, and transduced into cells in the presence of 1µg/ul Polybrene (Santa

Cruz). Cells were selected and maintained in supplemented media with 4 µg/mL Puromycin dihydrochloride (Santa Cruz). Single clones were isolated using Scienceware cloning discs (Sigma-Aldrich). Infections for generation of stable knockdown in HEK293 cells were performed with shRNA lentiviral particles (Santa Cruz Biotech) as described previously (Canton et al. 2012; Hehnly et al. 2015; Colicino et al. 2018). For expression of AKAP79, dAKAP1, and Gravin constructs in U2OS cells, transient transfections were performed using TransIT-LT1 reagent (Mirus) in Opti-MEM® (Life Technologies) media according to manufacturer's instructions.

Synthesis of CLP-reagents

CLP-linker synthesis:

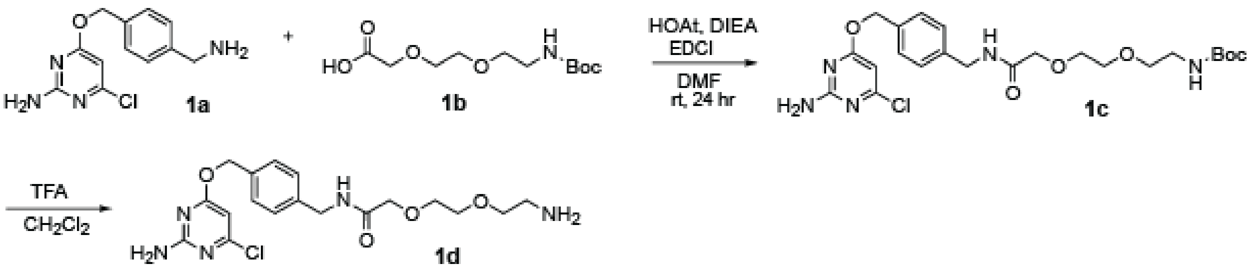

1a CLP-Amine, created as previously described (Hill et al. 2012), 1 Eq of **1a** (0.2 M) and 1.1 Eq of **1b** (Abachemscene) were dissolved in DMF at RT. The reaction was placed on ice. While stirring, 1.3 Eq HOAt (1-Hydroxy-7-azabenzotriazole) and 3 Eq DIEA (N,N-Diisopropylethylamine) were added. After 5 minutes on ice, 1.3 Eq of EDCI (1-Ethyl-3-(3-dimethylaminopropyl)carbodiimide) was added. The reaction was allowed to stir for 24 hours (letting the ice melt and the reaction slowly come to RT). Reaction was dissolved in ethyl acetate, washed with $NaHCO_3$ and brine, and dried with Na_2SO_4. Remaining solvent and DMF were removed via rotovaping and lyophilization. **1c** was deprotected with 30% TFA in DCM (0.2 M **1c** final). Solid **1c** was dissolved in CH_2Cl_2 and cooled on ice. TFA was added dropwise until it reached 30% v/v. Reaction was stirred for 1 hour at RT. Toluene was added (to help remove TFA) and the reaction was rotovapped to near dryness. Reaction was dissolved in ethyl acetate, washed with K_2CO_3, dried Na_2SO_4 and dried via rotovapping and lyophilization. Identity at each step was verified with MS.

BI2536 functionalization (+CLP-linker):

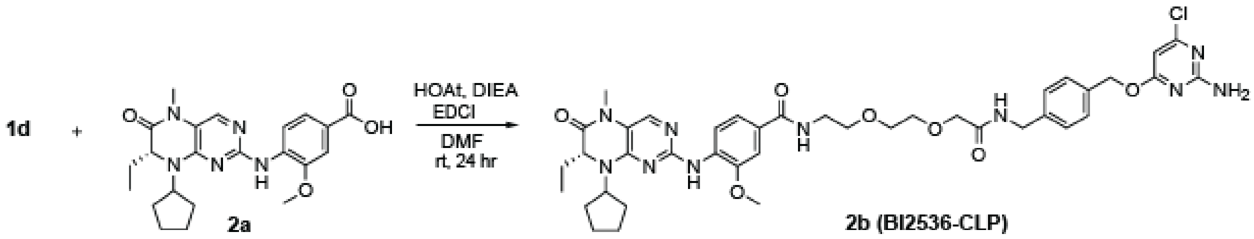

1 Eq **1d** (0.2 M) and 1.1 Eq of **2a** (Chem Scene) were dissolved in DMF at RT. The reaction was placed on ice. While stirring, 1.3 Eq HOAt and 3 Eq DIEA were added. After 5 minutes on ice, 1.3 Eq of EDCI was added. The reaction was allowed to stir for 24 hours (letting the ice melt and the reaction slowly come to RT). DMF was removed and **2b** (BI2536-CLP) was purified with HPLC. Identity was verified with MS. [M+H]+ = 817.7 *m/z*.

MLN8237 functionalization (+CLP-linker):

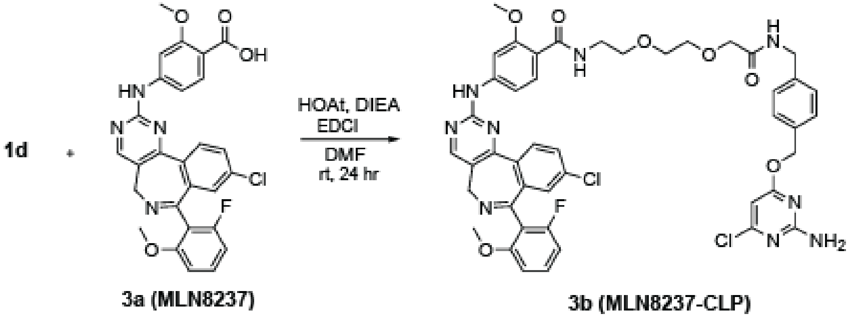

1 Eq **1d** (0.2 M) and 1.1 Eq of **3a** (MLN8237) were dissolved in DMF at RT. The reaction was placed on ice. While stirring, 2 Eq HOAt and 3 Eq DIEA were added. After 5 minutes on ice, 1.2 Eq of EDCI was added. The reaction was allowed to stir for 24 hours (letting the ice melt and the reaction slowly come to RT). DMF was removed and **3b** (MLN8237-CLP) was purified with HPLC. Identity was verified with MS. [M+H]+ = 911.0 *m/z*. **CLP-rhodamine Preparation:** 1 Eq **1a** (0.2 M) and 1 Eq 5(6)-carboxytetramethylrhodamine N-succinimidyl ester (Thermo Fisher) were

dissolved in DMF at RT. While stirring, 3 Eq DIEA were added. The reaction was allowed to stir for 24 hours. DMF was removed and product was purified with HPLC. Identity was verified with MS. $[M+H]^+$ = 676.2 *m/z.*

Protein expression and purification

His_6-SNAP-tag in pMCSG7 (Addgene) was expressed in *Escherichia coli* BL21(DE3) cells in 250 mL LB Miller broth. The evening prior to expression, 5 mL LB Miller broth, containing 50 µg/mL Ampicillin, was inoculated with transformed cells, and they were grown at 37°C overnight. The following day, the starter culture was used to seed 250 mL LB Miller broth in a 500 mL baffle flask. Cells were grown to OD_{600} ~0.3 and the temperature was then reduced to 20°C. Cells were allowed to grow to OD_{600} ~0.8, and then induced with 500 µM isopropyl β-D-thiogalactopyranoside. Induced cells were grown at 20°C overnight. Subsequent purification steps were carried out at 4°C. Cells were spun down at 6500 g, suspended in 10 mL of wash/lysis buffer [50 mM HEPES (pH 7.5), 300 mM NaCl, 20 mM imidazole, and 1 mM phenylmethanesulfonyl fluoride], and lysed via sonication. The lysate was centrifuged at 10000 g for 20 min, and the supernatant was allowed to batch bind with 0.7 mL of Ni-NTA (Ni^{2+}-nitrilotriacetate) beads for 60 min. The resin was collected by centrifugation at 500 g for 5 min and washed with 10 mL of wash/lysis buffer. The wash step was repeated three times. The Ni-NTA/His_6-SNAP-tag was added to a BioRad purification column, and washing was continued until the wash showed no remaining protein by Bradford. The protein was eluted using ~ 5 mL of elution buffer [50 mM HEPES (pH 7.5), 300 mM NaCl, 200 mM imidazole]. The eluate was dialyzed against 50 mM HEPES (pH 7.5), 200 mM NaCl, 5% glycerol, and 1 mM fresh dithiothreitol (DTT). Protein was aliquoted, flash-frozen in liquid N_2, and stored at − 80°C.

SNAP labeling experiments and pulse-chase labeling assays

In vitro labeling: 50 µM SNAP-tag was incubated with 75 µM CLP-linker-inhibitors (or DMSO alone for control reactions) [2.5% (v/v) final DMSO concentration] in buffer [20 mM Tris-Cl (pH 8), 200 mM NaCl, 1 mM DTT (added fresh)] at 26°C for 1.5 hr. The reactions were purified using

Zeba columns (Thermo Fisher) and exchanged into a MS compatible buffer (50 mM NH4HCO3, 0.2% HCO_2H). Ratios of unlabeled to labeled protein were determined using Native MS (Thermo Scientific LTQ Orbitrap XL/Bruker Esquire LC-Ion Trap). **Cellular labeling**: SNAP expressing (dox-induced) cells were treated with SNAP-Cell Fluorescein or SNAP-Cell 647-SiR (NEB) for 30 min in serum free DMEM at 37°C and 5% CO2. Cells were washed one time and incubated in fresh serum free DMEM for 30 min. Cells were fixed and stained as described under ‘immunofluorescence’. For pulse-chase labeling experiments, SNAP expressing (dox-induced) cells were treated with DMSO or increasing doses of CLP-BI2536 or CLP-MLN8237 for 1, 2, or 4 hr in serum free DMEM at 37°C and 5% CO2. Cells were washed one time and incubated in fresh serum free DMEM for 30 min. Cells were treated with 3 µM CLP-rhodamine (made in-house) in serum free DMEM for 30 min. Cells were washed one time and incubated in fresh serum free DMEM for 30 min. One wash with PBS was carried out and cells were lysed using immunoblotting protocol. Samples were resolved on an AnykD Criterion TGX Precast Midi Protein Gel (Biorad). Gels were scanned and fluorescence was measured with a GE Typhoon FLA 9000 scanner. Fluorescence measurements and densitometry was performed using NIH ImageJ (Fiji) software. Total SNAP labeling was determined by normalizing fluorescence signal of rhodamine bands to total SNAP protein expression as determined by densitometry.

% SNAPs Labeled by CLP-rhodamine = CLP rhodamine signal/SNAP western blot signal

% SNAPs Labeled by CLP-inhibitor = 100 % SNAPs Labeled by CLP-rhodamine

In vitro kinase assays

Plk1 assays: The kinase activity of purified Plk1 (SignalChem) was profiled using Casein as the substrate (0.2 mg/mL). Reactions contained 25 mM MOPS, pH 7.2; 12.5 mM β-glycerol-phosphate; 25 mM $MgCl_2$; 2 mM EGTA; 2 mM Na_3VO_4; 2 mM BME (β-mercaptoethanol); and 0.05 mg/mL BSA. Serial dilutions (1:3) of 25X compounds in DMSO [4% (v/v) final concentration in the assay] were used. For SNAP-inhibitor titrations, serial dilutions (1:3) were made in assay buffer, and an equivalent amount of DMSO [4% (v/v) final concentration in the assay] was later added to each well. Reciprocally, in assays where 25X inhibitor was added in DMSO, assay buffer was first added to each well (equivalent to the volume of SNAP-inhibitor in buffer). The last two wells in each row served as control reactions (+Kinase/No Inhibitor; and No Kinase/No Inhibitor) and received DMSO or buffer in place of inhibitor or kinase, respectively. After addition and mixing of the above components, kinase stock dilutions (10 nM final) were added to each well (except for the last well in each row, which served as the No Kinase/No Inhibitor control). Next, ATP-[γ ^{32}P] (final assay concentration: 0.012 μCi/μl) and unlabeled-ATP (final assay concentration: 40 μM) were added to the reactions. Plk1 was preincubated with ATP-competitive inhibitors and ATP-[γ ^{32}P]/unlabeled ATP for 30 min. To initiate the reactions, Casein was added. The reactions were incubated for 1 hr at RT. **Aurora A assays:** The kinase activity of purified Aurora A (Invitrogen) was profiled using myelin basic protein (MBP) as the substrate (0.2 mg/mL). Reactions contained 30 mM HEPES, pH 7.5; 10 mM $MgCl_2$; 0.6 mM EGTA; 2 mM Na_3VO_4; 2 mM BME; and 0.05 mg/mL BSA. Serial dilutions (1:3) of 25X compounds in DMSO [4% (v/v) final concentration in the assay] were used. For SNAP-inhibitor titrations, serial dilutions (1:3) were made in assay buffer, and an equivalent amount of DMSO [4% (v/v) final concentration in the assay] was later added to each well. Reciprocally, in assays where 25X inhibitor was added in DMSO, assay buffer was first added to each well (equivalent to the volume of SNAP-inhibitor in buffer). The last two wells in each row served as control reactions (+Kinase/No Inhibitor; and No Kinase/No Inhibitor) and received DMSO or buffer in place of inhibitor or kinase, respectively. After addition and mixing of the above components, kinase stock dilutions (15 nM final) were added to each well (except for the last well in each row, which served as the No Kinase/No Inhibitor control). To initiate the reactions, ATP-[γ ^{32}P] (final assay concentration: 0.006 μCi/μl) was added to the reactions. The reactions were incubated for 4 hr at RT. **All assays:** Assays were quenched by spotting 4.6 μL of each reaction mixture onto phosphocellulose membranes (Reaction Biology). The membranes were subjected to three sequential washes in 0.5% phosphoric acid for 10 min, dried, and exposed overnight to a phosphor screen (GE Healthcare). Blots were scanned using a phosphor scanner

(GE Typhoon FLA 9000). Raw data were processed with the GraphPad Prism software package (V5.0a) using the One site - Fit logIC_{50} function for curve fitting. Spots were quantified using ImageQuant. The kinase activity was first determined to be linear under assay conditions for Plk1 experiments at 10 nM Plk1 and at 15 nM Aurora A for Aurora A experiments, before conducting inhibitor titrations.

Drug treatments

For induction of SNAP expression cells were treated for 48–72 hr in FBS-supplemented DMEM with 1 µg/mL (for SNAP-PACT) or 4 µg/mL (for SNAP-Mis12) doxycycline hyclate (Sigma-Aldrich) prior to inhibitor treatments. For degradation assays, cells were dox-induced for 72 hr after which doxycycline was washed out (cells were incubated in normal media). At selected time point plates were collected, cells were washed once with PBS, plates were dried quickly, and frozen at −80°C until lysis. For nocodazole synchronization experiments, dox-induced cells were treated for 16 hr with nocodazole and 4 hr with nocodazole plus DMSO, 250 nM CLP-BI2536, or 100 nM CLP-MLN8237. Cells were washed once with PBS, collected via mitotic shake-off, and spun at 2000 rpm for 5 min at 4°C. Supernatants were discarded and pellets were kept for lysis. All lysates were prepared as described under 'immunoblotting'. For fixed cell experiments, both dox-induced and non-induced cells were grown on 1.5 poly-D-lysine coated coverslips (neuVitro) for at least 16 hr in complete DMEM and then treated with DMSO or CLP-compounds in serum-free DMEM for 1–4 hr. For washout experiments (pT210-Plk1 1 hr washout and γ-tubulin data), cells were incubated in serum-free DMEM without inhibitors for an additional 1 hr. Cells were washed once with PBS prior to fixation. For live-imaging experiments, cells were treated with CLP-compounds for 18 hr (see 'microscopy' for more details).

Zebrafish studies

Zebrafish were bred and embryos were collected. Embryos were injected with EMTB-3xGFP (100 pg mRNA or 20 pg pCS2 plasmid construct), SNAP-Cell Fluorescein (300 µM final embryo concentration), and/or CLP-BI2536 (250 nM final embryo concentration), and/or SNAP-PACT active or dead (200 pg mRNA) at the 2 cell stage using a microinjector (Warner Instruments PLI-100A) with a Kanatec magnetic base (MB-B), and a micromanipulator (Marzhauser Wetzlar MM33). Embryos were raised at 30°C until ~50% epiboly, at which point they were imaged on stereoscope, mounted in 2% agarose for live confocal imaging, or fixed using 4% paraformaldehyde + 0.5% Triton-X overnight at 4°C. Embryos were dechorionated in PBST (phosphate buffered saline + 0.1% Tween-20) and incubated in DAPI solution (1 µg/mL in PBS) for 2 hr at room temperature. Fixed embryos were then mounted in 2% agarose and imaged on confocal microscope.

Immunoblotting

Cells were lysed in RIPA lysis buffer (50 mM Tris HCl pH 7.4, 1% Triton X-100, 0.5% Sodium Deoxycholate, 0.1% SDS, 50 mM NaF, 120 mM NaCl, 5 mM β-glycerophosphate) supplemented with protease and phosphatase inhibitors (1 mM benzamidine, 1 mM AEBSF, 2 µg/mL leupeptin, 100 nM microcystin-LR). Lysed samples were boiled for 5 min at 95°C in NuPAGE LDS Sample Buffer 4X (Thermo Fisher) + 5% BME (Sigma-Aldrich). Protein concentration was determined using a Pierce BCA Protein Assay Kit (Thermo Fisher). Samples were resolved on Bolt 4–12% Bis-Tris Plus Gels (Invitrogen) or AnykD Criterion TGX Precast Midi Protein Gel (Biorad). Proteins were transferred to nitrocellulose for immunoblotting and probed with Anti-SNAP-tag rabbit antibody (NEB) and Anti-GAPDH−HRP mouse mAb, (Novus). Detection was achieved with a HRP-conjugated rabbit secondary antibody (GE Healthcare) followed by enhanced chemiluminescence with SuperSignal West Dura Extended Duration Substrate (Thermo Fisher). Densitometry was performed using NIH ImageJ (Fiji) software.

Immunofluorescence

Cells grown on 1.5 poly-D-lysine coated coverslips (neuVitro) for at least 16 hr were fixed for 10 min in 4% paraformaldehyde in PBS or in ice-cold methanol. Cells were permeabilized and blocked in PBS with 0.5% Triton X-100% and 1% BSA (PBSAT) for 30 min. Primary antibodies were diluted in PBSAT and cells were stained for 1 hr. Secondary antibodies conjugated to Alexa

Fluor dyes (Invitrogen) were diluted in PBSAT and applied for 1 hr. Staining with FITC-tubulin antibodies and/or DAPI staining always followed secondary incubation step and was carried out for 10–45 min in PBSAT. Washes (quick on and off) with PBSAT were carried out 10X between antibody and/or dye incubation steps and prior to mounting. Coverslips were mounted on slides using ProLong Diamond Antifade Mountant (Life Technologies).

Spindle classification measurements

To de-identify cell type and dox-treatment conditions and allow for blinded analysis of mitotic spindle differences, all identifying information on microscope slides was masked by a third-party individual. All mitotic cells within a coverslip were classified as either having normal bipolar, abnormal bipolar, or monopolar spindles based on morphology of the DNA and microtubules.

Microscopy

Fixed cell: Super-resolution 3D-SIM images were acquired on a Deltavision OMX V4 (GE Healthcare) system equipped with a 60x/1.42 NA PlanApo oil immersion lens (Olympus), 405-, 488-, 568-, and 642 nm solid-state lasers and sCMOS cameras (pco.edge). For SIM,15 images per optical slice (3 angles and five phases) were acquired. For both SIM and widefield (conventional) acquisitions, image stacks of 2.5–7 um with 0.125 um optical thick z-sections were acquired using immersion oil with a refractive index 1.516 or 1.518. Z-stacks were generated using the SNAP-PACT or SNAP-Mis12 channel to define the upper and lower regions of the plane with a 0.5 µM step size. SIM images were reconstructed using Wiener filter settings of 0.003 and optical transfer functions measured specifically for each channel with SoftWoRx software (GE Healthcare) to obtain super-resolution images with a twofold increase in resolution both axially and laterally. Images from different color channels were registered using parameters generated from a gold grid registration slide (GE Healthcare) and SoftWoRx. Widefield images were deconvolved using SoftWoRx. **Live-cell**: For LoKI experiments cells were first induced with doxycycline for 48–72 hr prior to transfection. For all time-lapse experiments cells were reverse transfected with GFP-H2B plasmid and plated onto µ-Slide 4 Well Glass Bottom: # 1.5H (170 µm

+ /- 5 μm) D 263 M Schott glass (Ibidi) in complete DMEM. Transient transfections were performed using TransIT-LT1 reagent (Mirus) with Opti-MEM (Life Technologies) media. The next day all cells were treated with 2 mM thymidine for 24 hr. The following day thymidine was washed out and after 4 hours cells were incubated with DMSO or CLP-inhibitors (LoKI experiments) or with no reagents (WT/KO Gravin experiments) in serum-free FluoroBrite DMEM. Time-lapse images were acquired on a Keyence BZ-X710 microscope using a 10X objective with 25% transmitted light and 100% aperture stop, with 1/60 s exposure for 488 channel. Images were captured every 5 min for 18 hr. **Zebrafish imaging**: Images were acquired on a Leica DMi8 (Leica, Bannockburn, IL) equipped with a Crest Optics X-light v2 Confocal Unit spinning disk, an 89 North – LDI laser with a Photometrics Prime-95B camera using a Nikon 40 × 1.15 N.A. Lamda S LWD objective. Stereoscope images were acquired on a Leica M165 FC stereoscope with a DFC9000 GT camera and a PLANAPO 10X objective.

Image analysis

Maximum intensity projections from z-stack images were generated using SoftWoRx (GE Healthcare) or NIH ImageJ (Fiji) software. All immunofluorescence signal measures were carried out using Fiji software. Sum slice 32-bit Tiff projections were generated from z-stack images for analysis of immunofluorescence at centrosomes. For kinetochore measurements the ImageJ 'SubtractMeasuredBackground' macro was first applied and sum slice 32-bit Tiff projections were generated. For centrosomes measurements, the oval selection tool in Fiji was used to draw a circle (ROI) around the centrosome in the 568 (SNAP-PACT) channel. The area of the circle remained consistent for all measurements and all replicates of an experiment. Measurements were taken in the 647 channel (which contained pT210-Plk1, Total Plk1, pT288-AurA, or γ-tubulin) using the predefined centrosome ROI. Using the measure function in Fiji, with 'Area' and 'Raw Integrated Density' predefined as measurements, values were determined for each centrosome and for an arbitrarily selected background region. The raw integrated density was recorded for each centrosome and the background. The average raw integrated density for the centrosomes was determined by adding together the raw integrated densities for each centrosome in a cell and dividing that value by 2. The integrated density for the background was subtracted from the average centrosome integrated density to yield a background-subtracted average integrated density signal for a centrosome. If the signal value was negative (signal at centrosome was lower than at background) the value was replaced with a 0. For kinetochore measurements, the selection tool in Fiji was used to draw an arbitrary region (ROI) around the kinetochore in the 405 (ACA, centromeric DNA) channel or in the 568 (SNAP-Mis12) channel. Measurements were taken in the 647 channel (which contained pS69-Hec1) using the predefined kinetochore ROI. Using the measure function in Fiji, with ‘Area’ and ‘Raw Integrated Density’ predefined as measurements, values were determined for each kinetochore. The raw integrated density was recorded for each kinetochore. For both centrosome and kinetochore experiments and average was calculated for each control and experimental condition. To do this the normalized average integrated densities were added together and divided by the total number of cells for that condition. This yielded a value that represents the background-normalized average integrated density at a centrosome or at the kinetochore for a particular condition. Values for drug-treated cells were then normalized to their respective DMSO-treated control. Integrated intensity surface plots were generated from sum-slice 32-bit Tiff projections of representative images using the 3D Surface Plot function in Fiji software. Maximum intensity heat maps were generated from maximum projection representative images using the 3D Surface Plot function with Fire LUT in Fiji software. **Zebrafish three-dimensional renderings**: Three-dimensional renderings were created using Imaris software (Bitplane). Individual mitotic cells were isolated and assigned a new color channel using the ‘Surfaces’ function to create a surface rendering. Surface renderings were created through the use of the Isoline function, where regions of individual mitotic cells were isolated based on intensity. Completed surface renderings were then merged and masked to create a channel that encompassed the mitotic cells of each embryo.

Statistical analysis

Statistics were performed using an unpaired two-tailed Student's t-test in GraphPad Prism software. All values are reported as mean ± standard error of the mean (s.e.m) with p-values less than 0.05 considered statistically significant. Number of independent experiments (N) and number of individual points over several experiments (n) are presented. For γ-tubulin experiments a ROUT (Q = 1%) outlier test was performed and two values were removed prior to performing an unpaired Student's t-test.

Sample size and replicates

The sample size was not statistically determined. Where applicable, $n > 15$ independent measurements were conducted across $N \geq 3$ independent experiments. For doxycycline removal experiments (Figure 2—figure supplement 1E, Figure 6—figure supplement 1B) at least 2–3 independent experiments were conducted per time point.

2.6 ACKNOWLEDGEMENTS

This chapter contains experiments from published work that was reprinted (adapted) with permission under the terms of the CC-BY License, Copyright Bucko et al. Bucko PJ, Lombard CK, Rathbun L, Garcia I, Bhat A, Wordeman L, Smith FD, Maly DJ, Hehnly H, and Scott JD. 2019. Subcellular drug targeting illuminates local kinase action. eLife 8:e52220. Chloe Lombard in Dustin Maly's lab (UW) synthesized CLP-BI2536 and CLP-MLN8237 compounds, purified protein, carried out *in vitro* labeling assays, conducted *in vitro* AurA kinase assays and helped with *in vitro* Plk1 kinase assays. Lindsay Rathbun in Heidi Hehnly's lab (Syracuse University) performed zebrafish experiments. Jennifer DeLuca (Colorado State University) provided the pS69-Hec1 antibody. Thank you to Patrina Pellett for imaging assistance, Juan-Jesus Vincente for help with data analysis and to members of the Scott lab for critical discussions.

2.7 FIGURES

Figure 1:

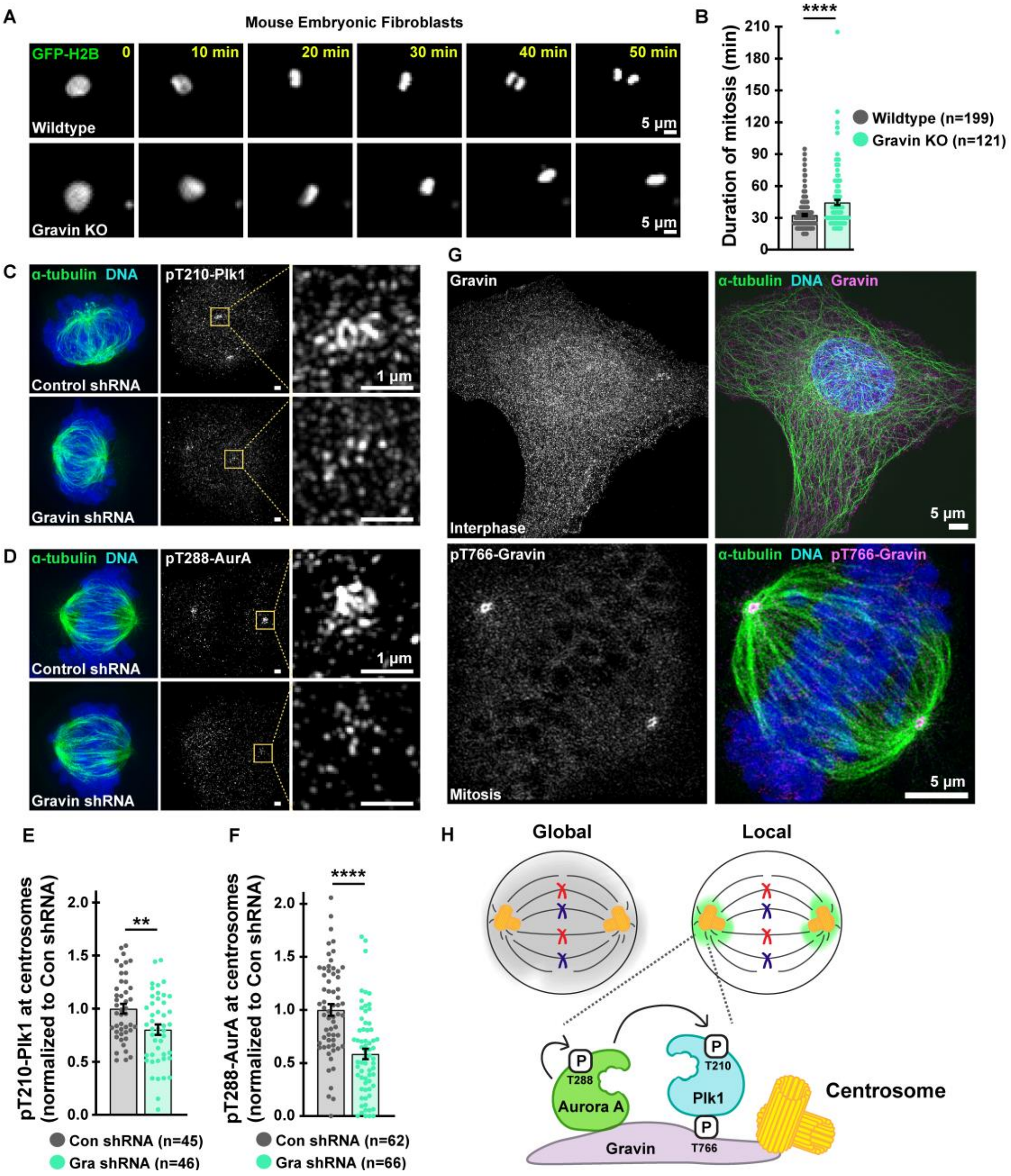

Figure 1 Legend: Loss of Gravin perturbs duration of mitosis and accumulation of active mitotic kinases at centrosomes. (**A**) Time-lapse images of primary MEFs derived from wildtype (top) and Gravin knockout (bottom) cells. Cells transiently expressing GFP-H2B were monitored through mitosis. (**B**) Quantification depicts duration of mitosis from nuclear envelope breakdown anaphase onset; Wildtype, n=199, Gravin KO, n=121, ****p<0.0001. (**C, D**) Structured illumination microscopy (SIM) of representative mitotic HEK293 cells stably expressing Control or Gravin

shRNA. Composite images (left) depict cells stained for α-tubulin (green) and DNA (blue). Immunofluorescence of pT210-Plk1 (**C**) and pT288-AurA (**D**) as an index of kinase activity (mid) and 5X magnification of centrosomal pT210-Plk1 (**C**) and pT288-AurA (**D**) signals (insets). (**E, F**) Quantification of centrosomal pT210-Plk1 (**E**) and pT288-AurA (**F**) immunofluorescence. Points represent individual cells (n). Data are normalized to Con shRNA; (**E**) Con shRNA, n=45, Gra shRNA, n=46, **p=0.0036; (**F**) Con shRNA, n=62, Gra shRNA, n=66, ****p<0.0001. Experiments were conducted at least three times (N=3) and P values were calculated by unpaired two-tailed Student's t-test. Data are mean ± s.e.m. (**G**) SIM micrographs of Gravin (top, gray and magenta) in interphase and pT766-Gravin (bottom, gray and magenta) in mitotic U2OS cells. Composite images (right) depict α-tubulin (green) and DNA (blue). (**H**) Schematic of global drug distribution (gray) vs drug targeting to centrosomes (green). Gravin scaffolds centrosome-localized pools of Plk1 and AurA.

Figure 1-figure supplement 1:

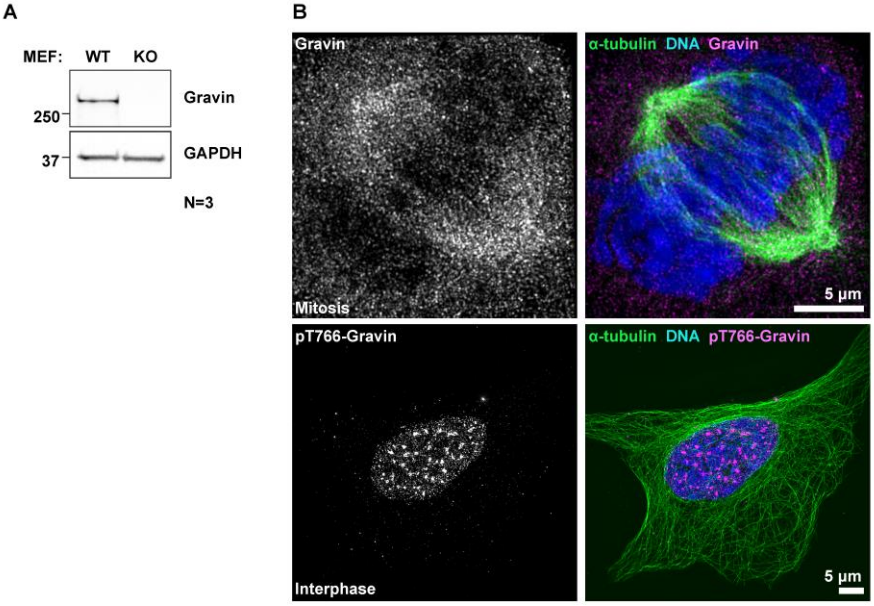

Figure 1-figure supplement 1 Legend: Confirmation of Gravin loss in MEFs and detection of Gravin and pT766-Gravin in mitotic and interphase U2OS cells. (**A**) Immunoblot confirming Gravin expression (top) in wildtype (WT) but not Gravin knockout (KO) primary MEFs. GAPDH loading controls (bottom). (**B**) Matched controls pertaining to Figure 1G. SIM micrographs of Gravin (top, gray and magenta) in mitotic and pT766-Gravin (bottom, gray and magenta) in interphase U2OS cells. Composite images (right) also depict α-tubulin (green) and DNA (blue).

Figure 2:

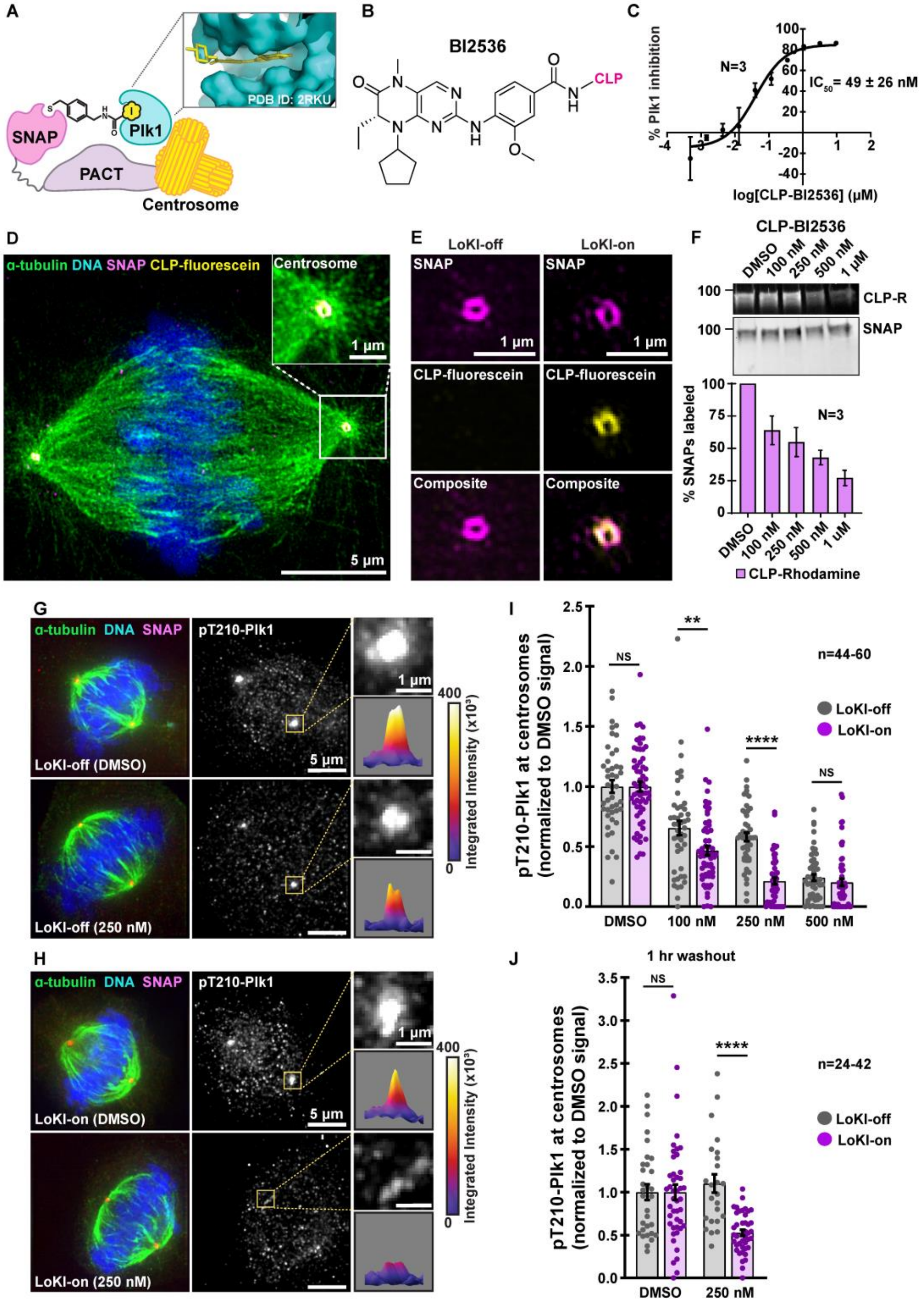

Figure 2 Legend: Generation and validation of the Local Kinase Inhibition (LoKI) system. (**A**) Schematic of a centrosome-directed LoKI platform. SNAP-PACT fusion proteins conjugate CLP-linked Plk1 inhibitors at centrosomes. Inset depicts BI2536 in the ATP-binding pocket of

Plk1. (**B**) Chemical structure of CLP-BI2536. (**C**) Dose-response curve of in vitro Plk1 inhibition with CLP-BI2536. (**D**) Structured illumination microscopy (SIM) of a LoKI-on U2OS cell labeled with CLP-fluorescein. Immunofluorescent detection of α-tubulin (green), DNA (blue), mCherry-SNAP-PACT (magenta) and CLP-fluorescein (yellow). Magnification of SNAP and CLP-fluorescein co-distribution at a centrosome (inset). (**E**) SIM micrographs of LoKI-off (left) and LoKI-on (right) U2OS cells. SNAP expression (top, magenta), CLP-fluorescein conjugation (mid, yellow) and composite images (bottom) are depicted. (**F**) Pulse-chase experiments measuring CLP-BI2536's ability to block CLP-rhodamine conjugation to LoKI-on. In-gel rhodamine fluorescence (top), immunoblot of SNAP loading controls (mid), and fluorescence quantification of pulse-chase experiments (bottom). (**G, H**) Immunofluorescence of representative mitotic LoKI-off (**G**) and LoKI-on (**H**) U2OS cells treated with DMSO or 250 nM CLP-BI2536 for 4 hr. Composite images (left) show α-tubulin (green), DNA (blue), and SNAP (magenta). Immunofluorescent detection of pT210-Plk1 (mid, gray) as an index of kinase activity. 5X magnification of centrosomal pT210-Plk1 signals and surface plots measuring integrated intensity of pT210-Plk1 signal (insets). (**I, J**) Quantification of centrosomal pT210-Plk1 immunofluorescence for LoKI-expressing cells. Points represent individual cells (n). Data normalized to DMSO. Application of DMSO or CLP-BI2536 for 4 hr, (**I**) 100 nM, LoKI-off, n = 46, LoKI-on, n=59, $^{**}p=0.0059$; 250 nM, LoKI-off, n=46, LoKI-on, n=46, $^{****}p<0.0001$ and drug treatment followed by 1 hr washout (**J**) 250 nM, LoKI-off, n=24, LoKI-on, n=42, $^{****}p<0.0001$. Experiments were conducted at least three times (N=3) and P values were calculated by unpaired two-tailed Student's t-test. Data are mean ± s.e.m. NS, not significant.

Figure 2-figure supplement 1:

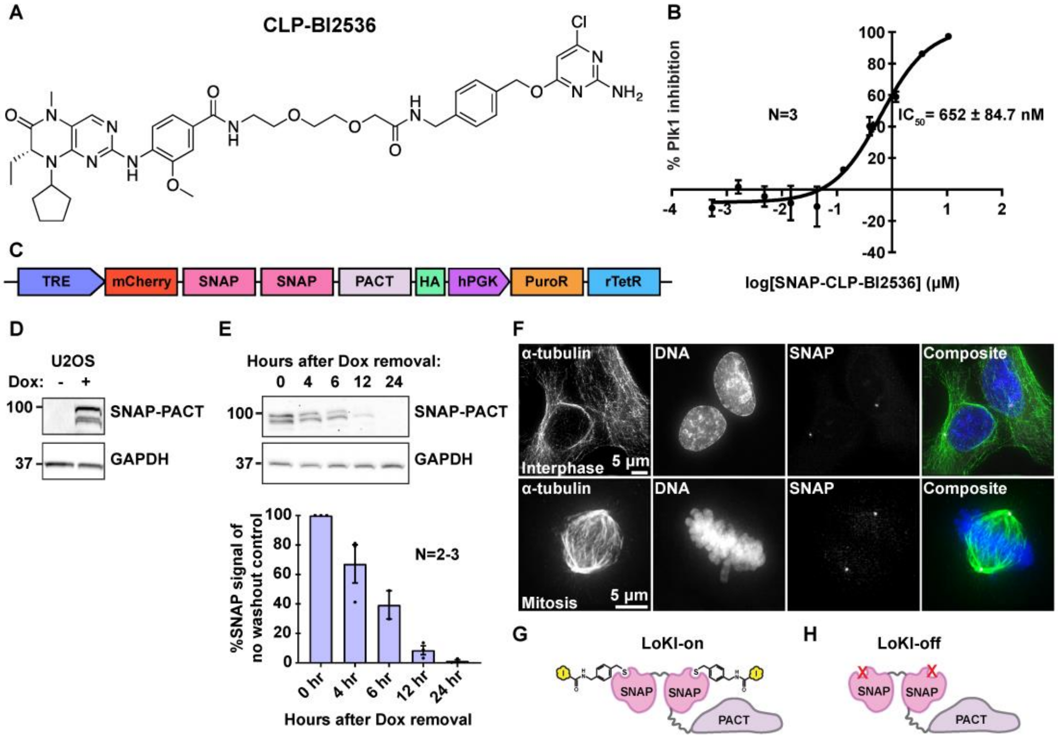

Figure 2-figure supplement 1 Legend: Additional controls for the validation of the LoKI system. (**A**) Full chemical structure of CLP-BI2536. (**B**) Dose-response curve depicting in vitro Plk1 inhibition with increasing concentrations of CLP-BI2536 conjugated to purified SNAP. (**C**) Schematic of LoKI viral construct with mCherry-SNAP-PACT under control of a doxycycline-inducible promoter. (**D**) Immunoblot confirming SNAP-PACT (top) expression after induction with doxycycline for 72 hr and GAPDH loading controls (bottom). (**E**) Immunoblot of SNAP-PACT (top) expression at selected time points after removal of doxycycline and GAPDH loading controls (bottom). Quantification of amalgamated data is presented below. (**F**) Immunofluorescent detection of interphase (top) and mitotic (bottom) U2OS cells showing α-tubulin (left and green), DNA (mid and blue), and SNAP (right and magenta). (**G, H**) Diagram of centrosomal LoKI-on (**G**) platform with drugs conjugated and LoKI-off (H) platform containing a mutation that occludes CLP binding. Experiments were conducted at least two times (N=2–3). Data are mean ± s.e.m.

Figure 2-figure supplement 2:

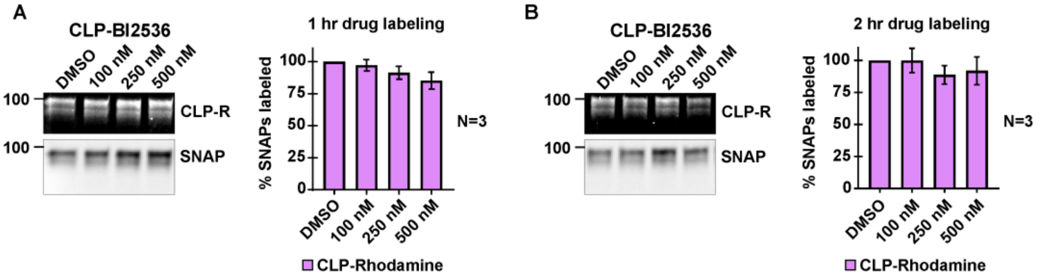

Figure 2-figure supplement 2 Legend: Additional pulse-chase experiments to determine how efficiently CLP-BI2536 labels SNAP-PACT. (**A, B**) Pulse-chase experiments carried out in U2OS cells after 1 hr (**A**) or 2 hr (**B**) treatment with CLP-BI2536. In-gel rhodamine fluorescence (top), immunoblot of SNAP loading controls (mid), and fluorescence quantification of pulse-chase experiments (bottom). Experiments were conducted at least three times (N=3). Data are mean ± s.e.m.

Figure 2-figure supplement 3:

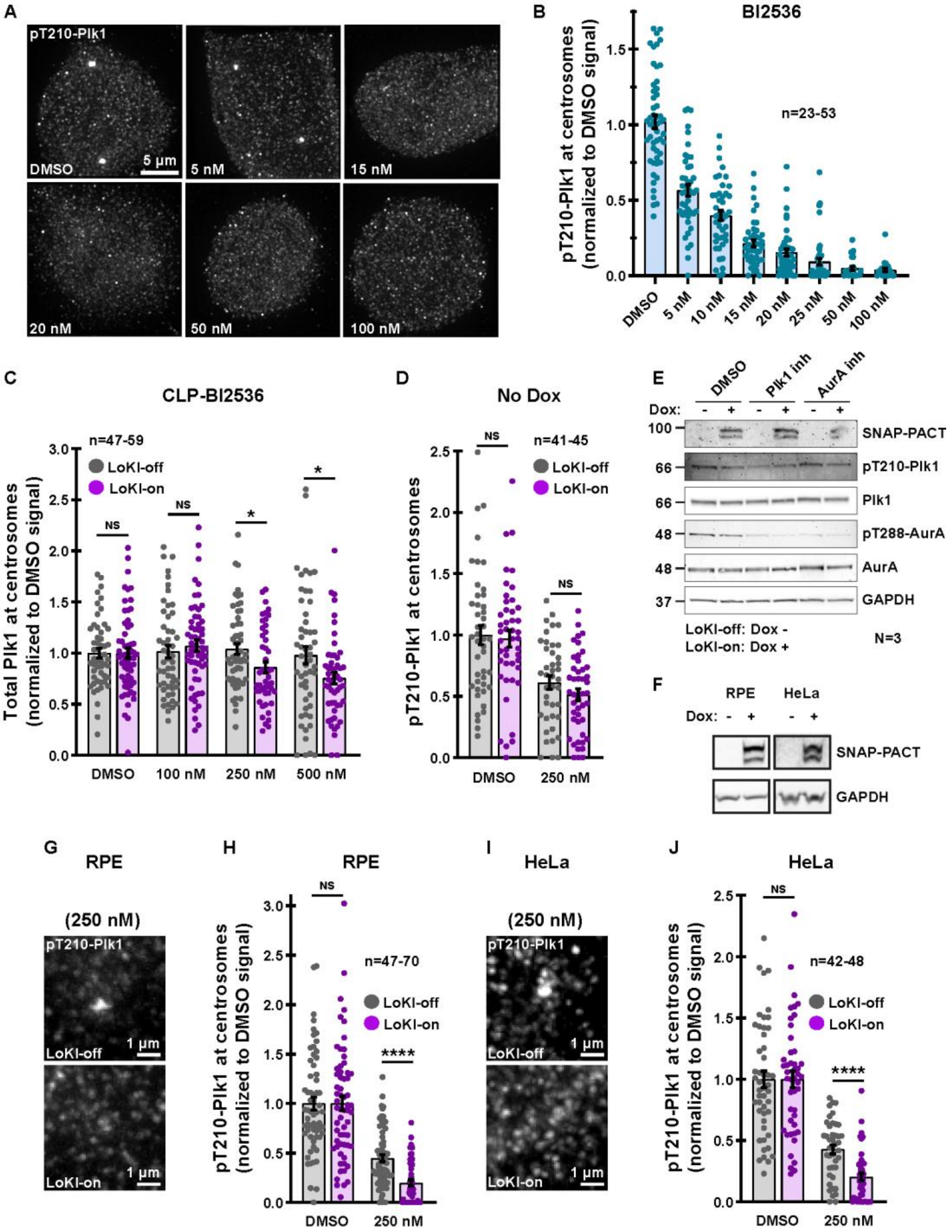

Figure 2-figure supplement 3 Legend: Characterization of Plk1 inhibition with BI2536 and CLP-BI2536. (**A**) Immunofluorescence detection of pT210-Plk1 as an index of kinase activity in parental U2OS cells treated with DMSO or unconjugated BI2536 for 4 hr. (**B**) Quantification of centrosomal pT210-Plk1 immunofluorescence collected from parental U2OS cells. (**C**) Quantification of total Plk1 immunofluorescence at centrosomes in LoKI-expressing cells after 4 hr CLP-BI2536 treatment; 250 nM, LoKI-off, n=55, LoKI-on, n=47, *p=0.0217; 500 nM, LoKI-off,

n=52, LoKI-on, n=51, *p=0.0295. (**D**) Quantification of pT210-Plk1 immunofluorescence in control cells lacking SNAP expression (not induced with doxycycline) after 4 hr CLP-BI2536 treatment. (**E**) Immunoblot detection of pT210-Plk1 (blot 2) and pT288-AurA (blot 4) in LoKI-off and LoKI-on expressing cells collected via mitotic shake-off. Cells were treated for 16 hr with nocodazole and 4 hr with nocodazole plus DMSO, 250 nM CLP-BI2536, or 100 nM CLP-MLN8237. Total Plk1 (blot 3), AurA (blot 5), SNAP-PACT (blot 1), and GAPDH (blot 6) are also depicted. (**F**) Immunoblot confirming SNAP-PACT (top) expression after induction with doxycycline for 72 hr in RPE and HeLa cells and GAPDH loading controls (bottom). (**G–J**) Immunofluorescence detection of pT210-Plk1 at centrosomes in LoKI-off (top) and LoKI-on (bottom) RPE (**G**) and HeLa (**I**) cells treated with 250 nM CLP-BI2536 for 4 hr. Quantification of pT210-Plk1 immunofluorescence at centrosomes in RPE (**H**) 250 nM, LoKI-off, n=70, LoKI-on, n=47, ****p<0.0001 and HeLa (**J**) 250 nM, LoKI-off, n=42, LoKI-on, n=46, ****p<0.0001 LoKI-expressing cells after 4 hr CLP-BI2536 treatment. Points represent individual cells (n). Data normalized to DMSO. Experiments were conducted at least three times (N=3) and P values were calculated by unpaired two-tailed Student’s t-test. Data are mean ± s.e.m. NS, not significant.

Figure 2-figure supplement 4:

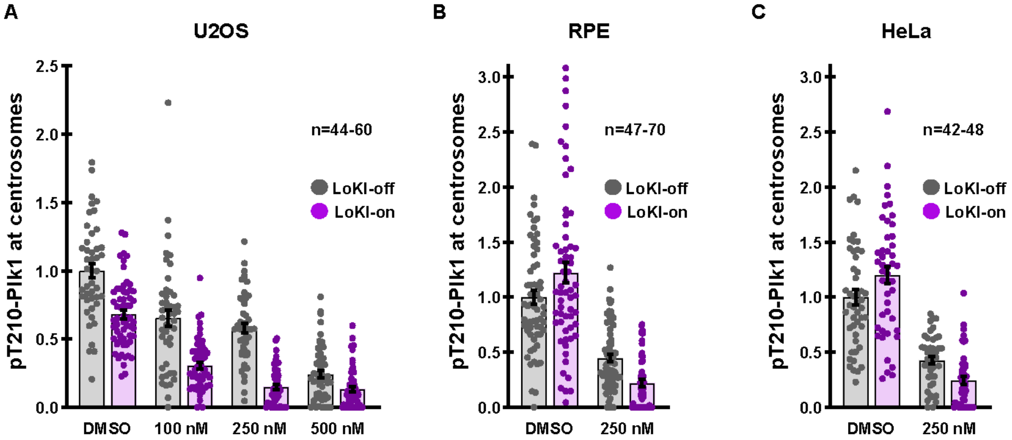

Figure 2-figure supplement 4 Legend: Non-normalized quantification of pT210-Plk1 signal at centrosomes. Quantification of non-normalized pT210-Plk1 immunofluorescence signal at centrosomes in U2OS (**A**) RPE (**B**) and HeLa (**C**) LoKI-expressing cells after treatment with indicated concentrations of CLP-BI2536 for 4 hr. Points represent individual cells (n). Experiments were conducted at least three times (N=3). Data are mean ± s.e.m.

Figure 3:

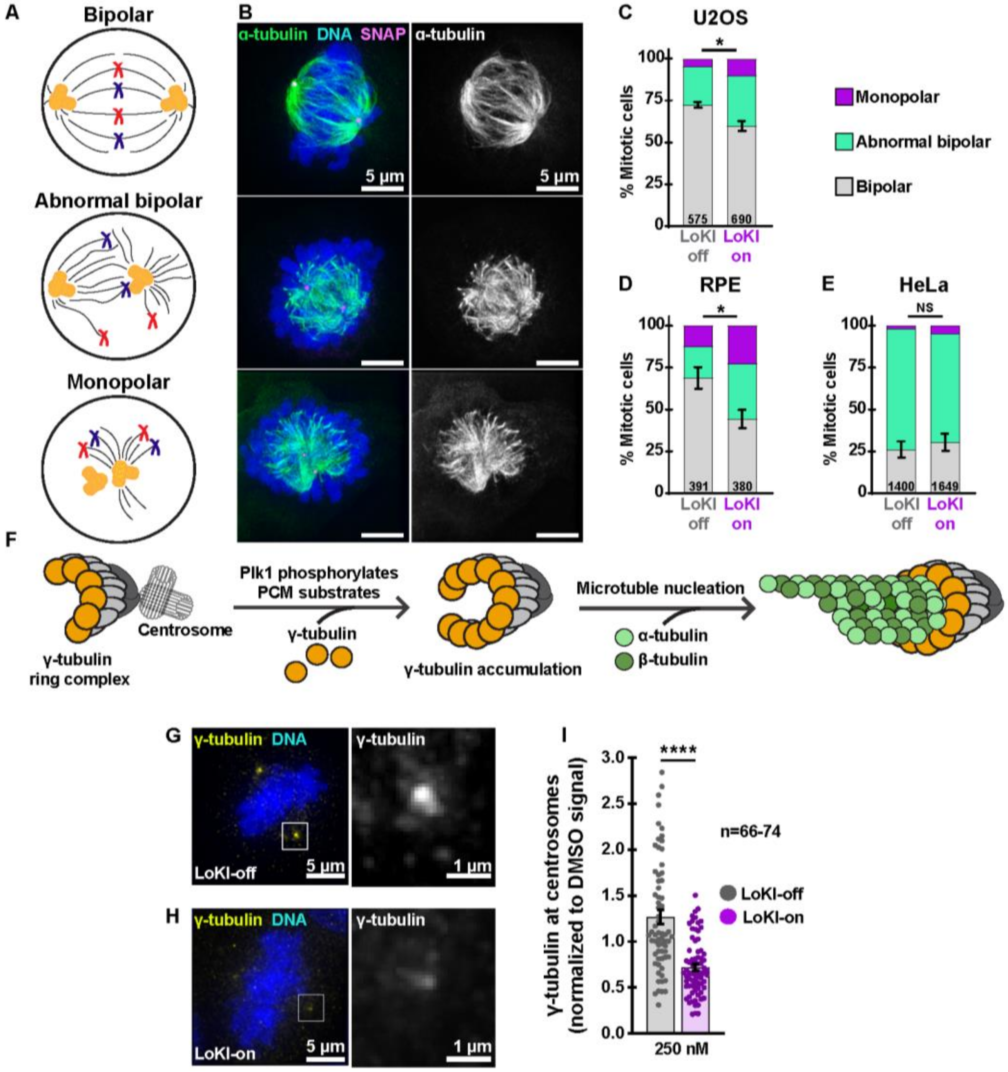

Figure 3 Legend: Centrosome-targeted Plk1 inhibitors perturb early mitotic events. (**A**) Schematic depicting bipolar (top), abnormal bipolar (mid), and monopolar (bottom) mitotic spindle classifications. (**B**) Representative composite (left) images show α-tubulin (green), DNA (blue), and SNAP (magenta) or α-tubulin (right, gray) staining alone for each spindle type in U2OS cells. (**C–E**) Spindle profile measurements of U2OS (**C**) RPE (**D**) and HeLa (**E**) cells treated with 250 nM CLP-BI2536 for 4 hr. Spindle profiling indicates the % of each spindle type in drug-treated LoKI-on and LoKI-off cells. Number of cells analyzed per condition are indicated; (**C**) n=3, *p=0.0214; (**D**) n=3, *p=0.0269. (**F**) Schematic depicting that Plk1 phosphorylation of pericentriolar substrates facilitates accumulation of γ-tubulin at centrosomes and microtubule nucleation. (**G, H**) Representative composite (left) images show γ-tubulin (yellow) and DNA (blue) in U2OS cells expressing LoKI-off (**G**) and LoKI-on (**H**) treated with 250 nM CLP-BI2536 for 4 hr, followed by a 1 hr washout. 5X magnified grayscale images of centrosomal γ-tubulin (right). (**I**) Quantification of centrosomal γ-tubulin immunofluorescence in LoKI-expressing cells. Points represent individual cells (n). Data normalized to DMSO. A ROUT (Q=1%) outlier test was performed and two values were removed prior to performing statistical tests; LoKI-off, n=66, LoKI-

on, n=74, ****p<0.0001. Experiments were conducted at least three times (N=3) and P values were calculated by unpaired two-tailed Student’s t-test. Data are mean ± s.e.m. NS, not significant.

Figure 3-figure supplement 1:

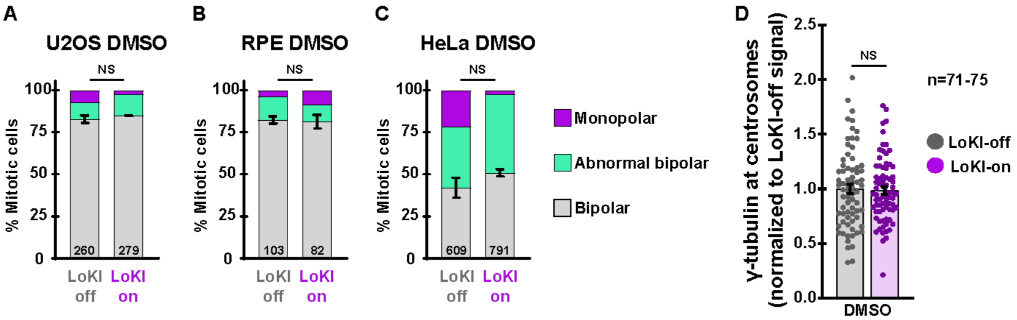

Figure 3-figure supplement 1 Legend: Baseline controls evaluating DMSO-treated cells for mitotic defects. (**A–C**) Mitotic spindle classifications for LoKI-expressing U2OS (**A**) RPE (**B**) and HeLa (**C**) cells treated with DMSO for 4 hr. Profiling indicates the % of each defined spindle type in drug treated LoKI-on and LoKI-off cells. Number of cells analyzed per condition are indicated. (**D**) Quantification of γ-tubulin immunofluorescence at centrosomes in LoKI-expressing U2OS cells treated with DMSO, followed by a 1 hr washout. Points represent individual cells (n). Data normalized to DMSO. Experiments were conducted at least three times (N=3) and P values were calculated by unpaired two-tailed Student's t-test. Data are mean ± s.e.m. NS, not significant.

Figure 4:

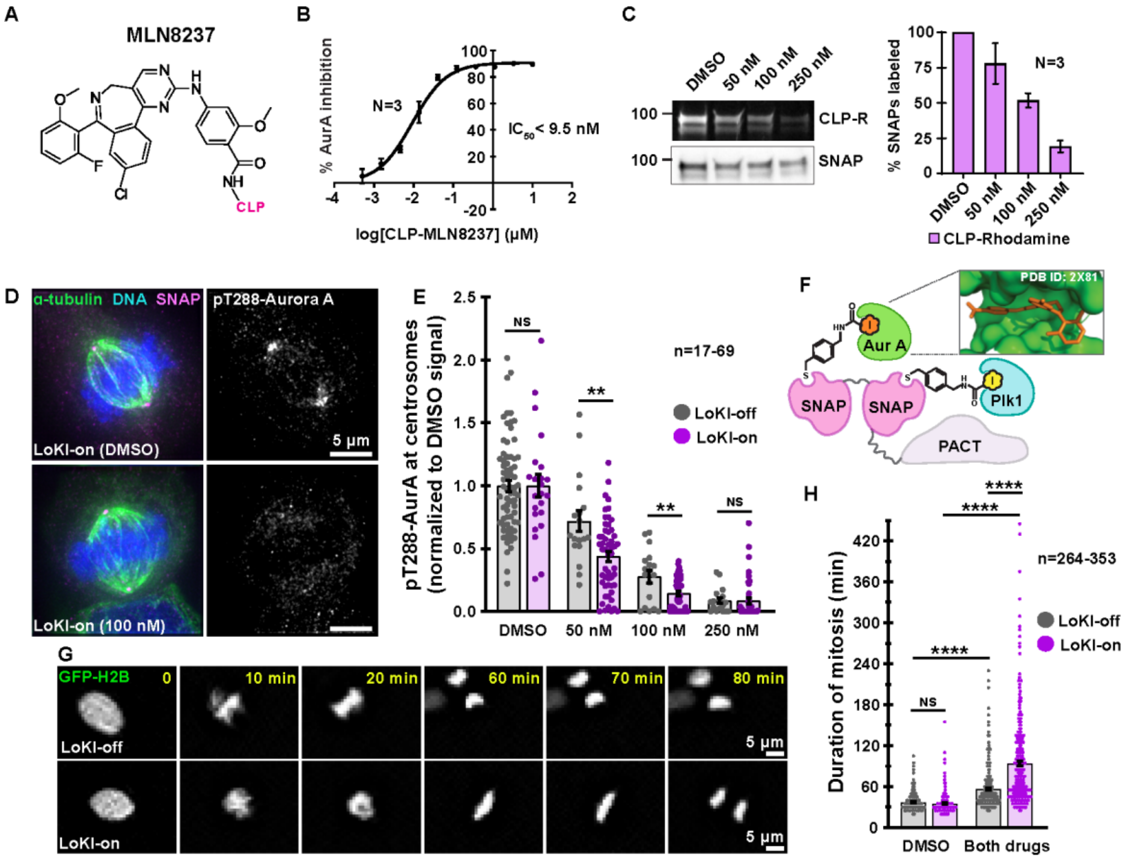

Figure 4 Legend: Combined Plk1 and AurA inhibition at centrosomes more profoundly delays mitosis than global kinase inhibition. (**A**) Chemical structure of AurA kinase inhibitor CLP-MLN8237. (**B**) Dose-response curve of in vitro AurA kinase inhibition with CLP-MLN8237. (**C**) Pulse-chase experiments measuring CLP-MLN8237's ability to block CLP-rhodamine conjugation to LoKI-on. In-gel rhodamine fluorescence (top), immunoblot of SNAP loading controls (mid), and fluorescence quantification of pulse-chase experiments (bottom). (**D**) Immunofluorescence of representative mitotic LoKI-on U2OS cells treated with DMSO or 100 nM CLP-MLN8237 for 4 hr. Composite images (left) show α-tubulin (green), DNA (blue), and SNAP (magenta). Immunofluorescent detection of pT288-AurA (right, gray) as an index of kinase activity is depicted. (**E**) Quantification of centrosomal pT288-AurA immunofluorescence after 4 hr CLP-MLN8237 treatment; 50 nM, LoKI-off, n=18, LoKI-on, n=53, **p=0.0014; 100 nM, LoKI-off, n=18, LoKI-on, n=48, **p=0.0026. (**F**) Schematic of dual LoKI-on moiety conjugated to CLP-BI2536 and CLP-MLN8237. Inset depicts MLN8237 in the ATP-binding pocket of AurA. (**G**) Representative time-lapse images of mitotic LoKI-off (top) and LoKI-on (bottom) cells transiently expressing GFP-H2B. Cells were treated with a combination (both drugs) of 250 nM CLP-BI2536 and 100 nM CLP-MLN8237 and monitored for 18 hr. (**H**) Quantification of time-lapse experiments depicts duration of mitosis from nuclear envelope breakdown to the onset of anaphase; DMSO, LoKI-off, n=264, both drugs, LoKI-off n=353, ****p<0.0001; DMSO, LoKI-on, n=292, both drugs, LoKI-on n=331, ****p<0.0001; both drugs, LoKI-off, n=353, both drugs, LoKI-on, n=331, ****p<0.0001. Points in (**E**) and (**H**) represent individual cells (n). Points in (**E**) are normalized to DMSO. Experiments

were conducted at least three times (N=3) and P values were calculated by unpaired two-tailed Student’s t-test. Data are mean ± s.e.m. NS, not significant.

Figure 4-figure supplement 1:

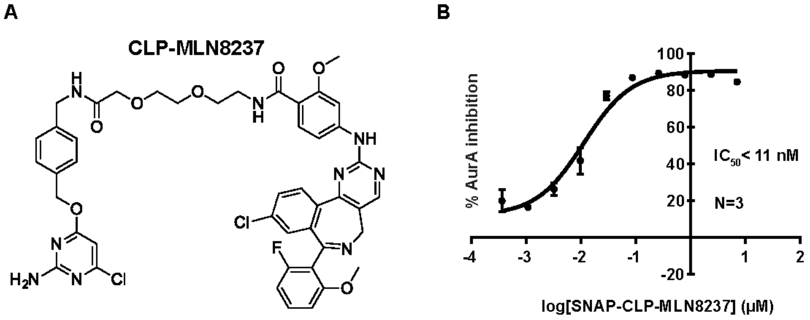

Figure 4-figure supplement 1 Legend: Structure of CLP-MLN8237 and AurA activity assay. (**A**) Full chemical structure of CLP-MLN8237. (**B**) Graph depicting in vitro AurA kinase inhibition with increasing concentrations of CLP-MLN8237 conjugated to purified SNAP. Experiments were conducted at least three times (N=3). Data are mean ± s.e.m.

Figure 4-figure supplement 2:

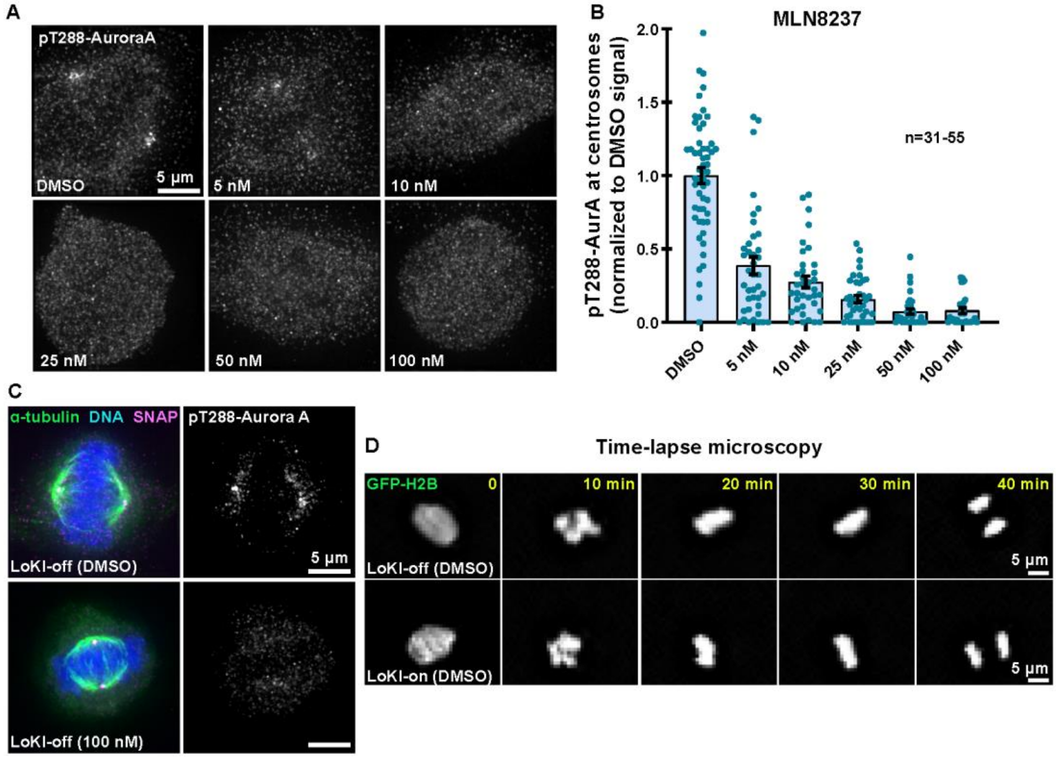

Figure 4-figure supplement 2 Legend: Characterization of AurA inhibition with MLN8237 and CLP-MLN8237. (**A**) Immunofluorescence detection of pT288-AurA as an index of kinase activity in parental U2OS cells treated with DMSO or unconjugated MLN8237 for 4 hr. (**B**) Quantification of centrosomal pT210-AurA immunofluorescence collected from parental U2OS cells. Data normalized to DMSO. Points represent individual cells (n). Experiments were conducted at least three times (N=3). Data are mean ± s.e.m. (**C**) Immunofluorescence of representative mitotic LoKI-off U2OS cells treated with DMSO or 100 nM CLP-MLN8237 for 4 hr. Composite images (left) show α-tubulin (green), DNA (blue), and SNAP (magenta). Immunofluorescent detection of pT288-AurA (right, gray) as an index of kinase activity is depicted. (**D**) Representative time-lapse images of mitotic LoKI-off (top) and LoKI-on (bottom) cells transiently expressing GFP-H2B. Cells were treated with DMSO and monitored for 18 hr.

Figure 4-figure supplement 3:

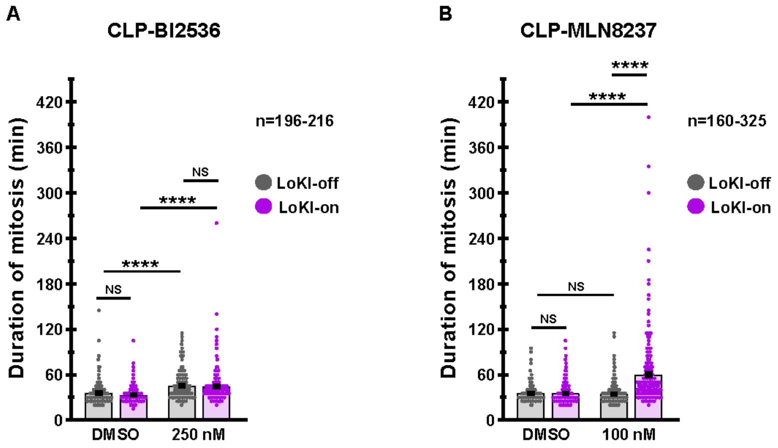

Figure 4-figure supplement 3 Legend: Mitotic duration is prolonged in cells treated with centrosome-targeted Plk1 or AurA inhibitors. (**A, B**) Quantification of time-lapse experiments depicts duration of mitosis from nuclear envelope breakdown to the onset of anaphase in cells treated with CLP-BI2536 (**A**) DMSO, LoKI-off, n=196, 250 nM, LoKI-off n=216, ****p<0.0001; DMSO, LoKI-on, n=211, 250 nM, LoKI-on n=211, ****p<0.0001 or CLP-MLN8237 (**B**) DMSO, LoKI-on, n=257, 100 nM, LoKI-on n=325, ****p<0.0001; 100 nM, LoKI-off, n=237, 100 nM, LoKI-on n=325, ****p<0.0001. Points represent individual cells (n). Experiments were conducted at least three times (N=3) and P values were calculated by unpaired two-tailed Student's t-test. Data are mean ± s.e.m. NS, not significant.

Figure 5:

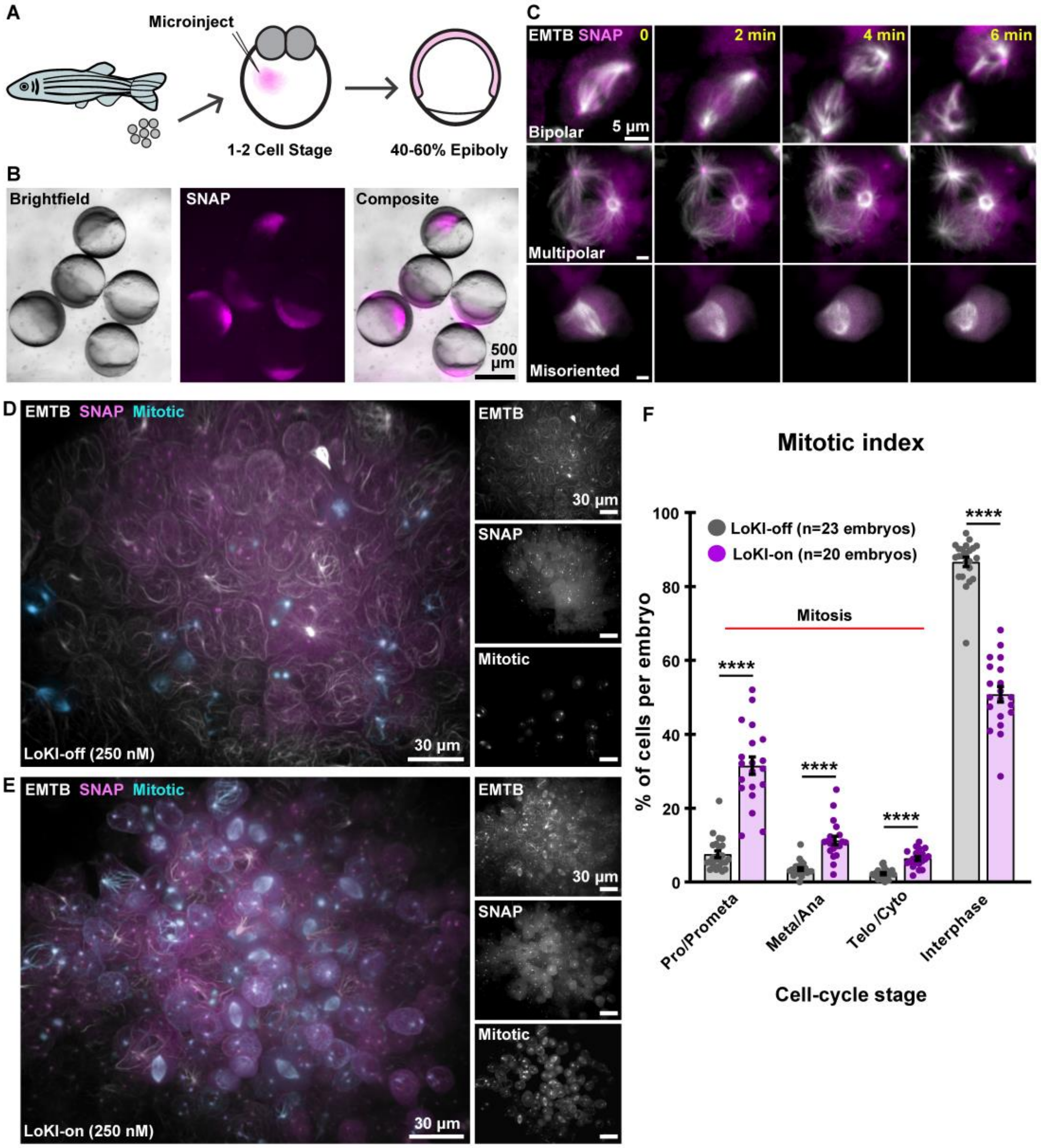

Figure 5 Legend: In vivo implementation of LoKI implicates Plk1 activity at centrosomes in coordinating mitoses during early development. (**A**) Schematic of experimental scheme. Microinjection of LoKI mRNAs into zebrafish embryos occurs at the 1–2 cell stage. Live-cell imaging is conducted at ~50% epiboly. (**B**) Zebrafish embryos (left, brightfield) depicting regional expression of SNAP (mid, magenta) at ~50% epiboly. Composite images (right) depict expression of SNAP only in the cells of the zebrafish embryos. (**C**) Centrosomal delivery of Plk1 inhibitors perturb cell division in zebrafish embryos. Time-lapse images of dividing cells embedded in LoKI-on zebrafish embryos 5 hr post application of 250 nM CLP-BI2536. Representative examples of normal bipolar spindles (top) multipolar spindles (mid) and spindle orientation defects (bottom) are presented. Composite images show microtubule marker EMTB-3xGFP (white) and SNAP (magenta). (**D, E**) 3D-rendered images depict incidence of mitotic cells and general organization of whole LoKI-off (D) or LoKI-on (**E**) zebrafish embryos treated with 250 nM CLP-BI2536. EMTB

(white and top inset), SNAP (magenta and mid inset), and mitotic cells (cyan and bottom inset) are shown. (**F**) Graph depicting mitotic index measurements for LoKI-expressing embryos; LoKI-off, n=23, LoKI-on, n=20, ****p<0.0001. Each point represents % of cells per individual embryo (n). Experiments were conducted at least three times (N=3) and P values were calculated by unpaired two-tailed Student's t-test. Data are mean ± s.e.m.

Figure 5-figure supplement 1:

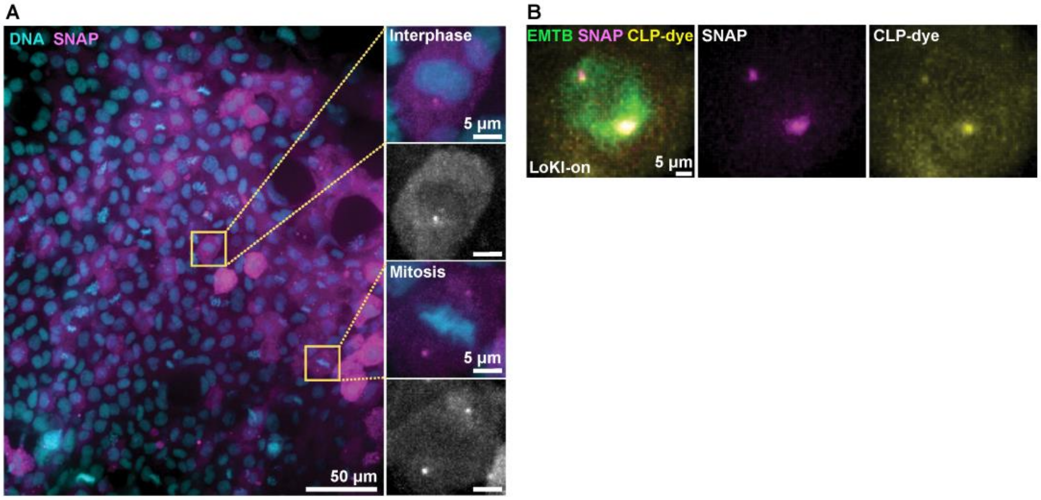

Figure 5-figure supplement 1 Legend: Validation of LoKI expression in zebrafish embryos. (**A**) Confocal micrograph of an embryo expressing LoKI-on (magenta) counterstained for DNA (cyan). Magnification of cells (insets) at interphase (upper) and mitosis (lower). Grayscale images reveal localization of the centrosomal LoKI-on platform. (**B**) In vivo validation of drug delivery. Immunofluorescent detection of microtubule marker EMTB-3xGFP (green), SNAP (magenta) and CLP-647 dye (yellow) in a cell embedded in a living zebrafish embryo.

Figure 6:

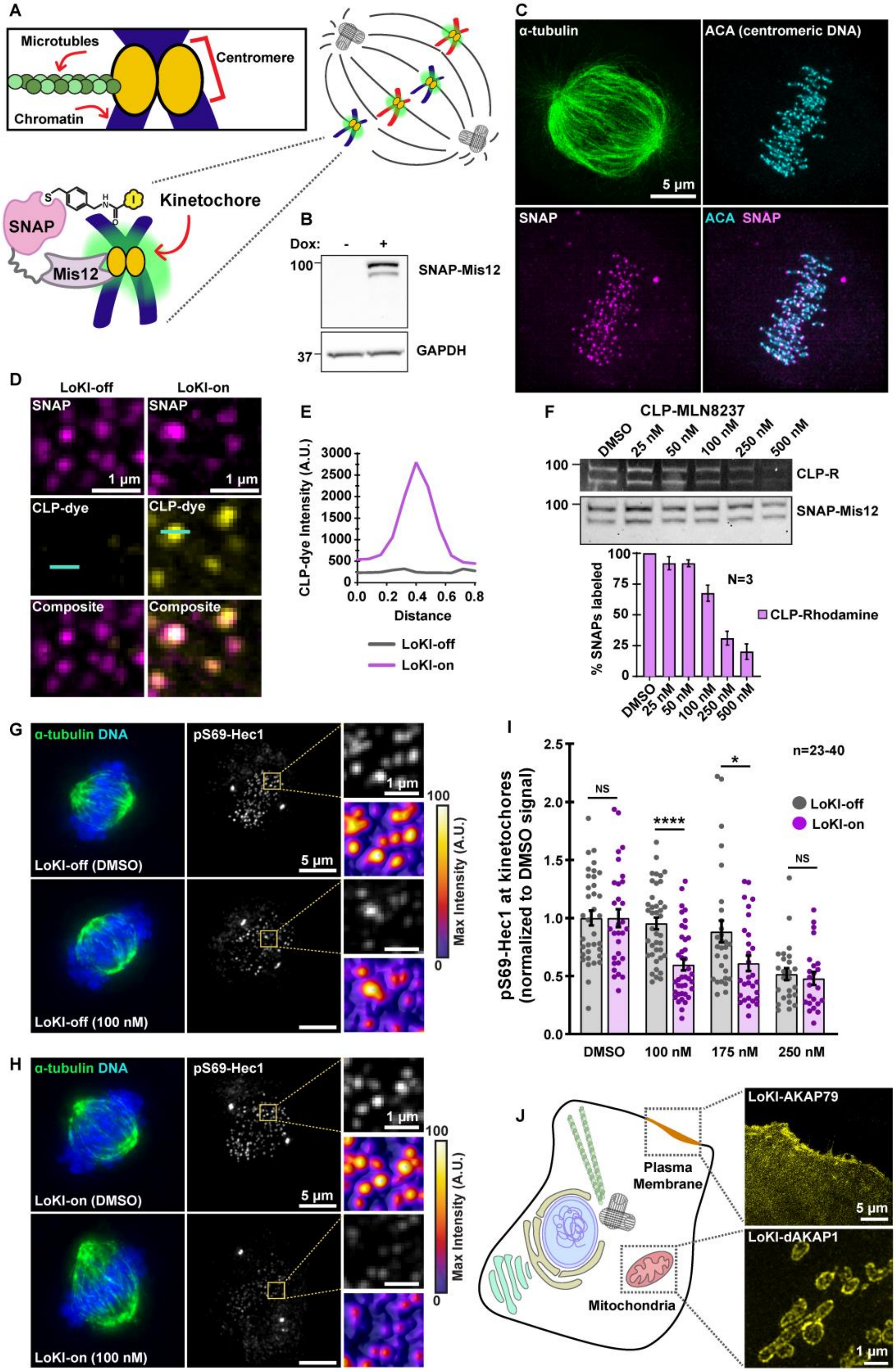
A
Microtubles
Centromere
Chromatin
SNAP
Mis12
Kinetochore
B
Dox: - +
100
SNAP-Mis12
37
GAPDH
C
α-tubulin
ACA (centromeric DNA)
5 μm
SNAP
ACA SNAP
D
LoKI-off
LoKI-on
SNAP
SNAP
1 μm
1 μm
CLP-dye
CLP-dye
Composite
Composite
E
CLP-dye Intensity (A.U.)
3000
2500
2000
1500
1000
500
0
0.0 0.2 0.4 0.6 0.8
Distance
LoKI-off
LoKI-on
F
CLP-MLN8237
DMSO
25 nM
50 nM
100 nM
250 nM
500 nM
100
CLP-R
100
SNAP-Mis12
% SNAPs labeled
100
75
50
25
0
N=3
CLP-Rhodamine
DMSO
25 nM
50 nM
100 nM
250 nM
500 nM
G
α-tubulin DNA
pS69-Hec1
1 μm
100
Max Intensity (A.U.)
0
5 μm
LoKI-off (DMSO)
LoKI-off (100 nM)
H
α-tubulin DNA
pS69-Hec1
1 μm
100
Max Intensity (A.U.)
0
5 μm
LoKI-on (DMSO)
LoKI-on (100 nM)
I
pS69-Hec1 at kinetochores (normalized to DMSO signal)
2.5
2.0
1.5
1.0
0.5
0.0
n=23-40
NS
****
*
NS
LoKI-off
LoKI-on
DMSO
100 nM
175 nM
250 nM
J
Plasma Membrane
Mitochondria
LoKI-AKAP79
5 μm
LoKI-dAKAP1
1 μm

Figure 6 Legend: Kinetochore-targeted CLP-MLN8237 reveals that AurA-mediated Hec1 phosphorylation is a local event. (**A**) Schematic of microtubule association with centromeric chromatin at kinetochores. Diagram of LoKI-Mis12 securing CLP-linked inhibitors to kinetochores (inset). (**B**) Immunoblot confirming SNAP-Mis12 (top) expression after induction with doxycycline for 72 hr and GAPDH loading controls (bottom). (**C**) Representative SIM micrograph depicting α-tubulin (green), mCherry-SNAP-Mis12 (magenta) and centromeric DNA marker ACA (cyan) in U2OS cells. Composite image depicts co-distribution of LoKI-Mis12 with ACA. (**D**) SIM micrographs of LoKI-off (left) and LoKI-on (right) U2OS cells. SNAP expression (top, magenta), CLP-647 conjugation (mid, yellow) and composite images (bottom) are depicted. Line on CLP-dye was used to generate panel E plot. (**E**) Line plot of CLP-dye signal from a representative kinetochore in panel D. (**F**) Pulse-chase experiments measuring CLP-MLN8237's ability to block CLP-rhodamine conjugation to LoKI-on. In-gel rhodamine fluorescence (top), immunoblot of SNAP loading controls (mid), and fluorescence quantification of pulse-chase experiments (bottom). (**G, H**) Immunofluorescence of representative mitotic LoKI-off (**G**) and LoKI-on (**H**) U2OS cells treated with DMSO or 100 nM CLP-MLN8237 for 4 hr. Composite images (left) show α-tubulin (green) and DNA (blue). Immunofluorescence detection of pS69-Hec1 (mid and top right insets, gray). Heat maps (bottom right) depict maximum intensity measurements of pS69-Hec1 signal from representative insets. (**I**) Quantification of pS69-Hec1 immunofluorescence at kinetochores after 4 hr CLP-MLN8237 treatment; 100 nM, LoKI-off, n=40, LoKI-on, n=39, $****p<0.0001$; 175 nM, LoKI-off, n=29, LoKI-on, n=29, $*p=0.0212$. Points represent individual cells (n). Data normalized to DMSO. Experiments were conducted at least three times (N=3) and P values were calculated by unpaired two-tailed Student's t-test. Data are mean ± s.e.m. NS, not significant. (**J**) Implementation of LoKI at other subcellular locations shows SNAP targeting to plasma membrane via AKAP79 and mitochondrial localization via d-AKAP1.

Figure 6-figure supplement 1:

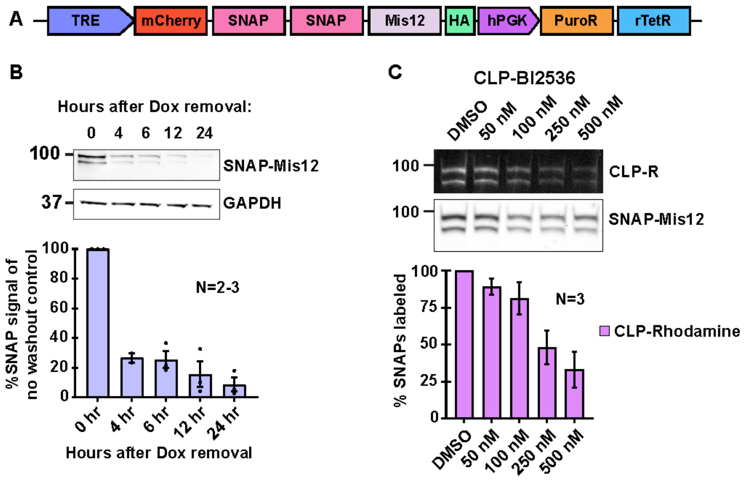

Figure 6-figure supplement 1 Legend: Validation of Mis12-LoKI platforms. (**A**) Schematic depicting the Mis12-LoKI viral construct with mCherry-SNAP-Mis12 under the control of a doxycycline-inducible promoter. (**B**) Immunoblot of SNAP-Mis12 (top) expression at selected time points after removal of doxycycline and GAPDH loading controls (bottom). Quantification of amalgamated data is presented below. (**C**) Pulse-chase experiments measuring CLP-MLN8237's ability to block CLP-rhodamine conjugation to LoKI-on. In-gel rhodamine fluorescence (top), immunoblot of SNAP loading controls (mid), and fluorescence quantification of pulse-chase experiments (bottom). Experiments were conducted at least two times (N=2–3). Data are mean ± s.e.m.

Figure 6-figure supplement 2:

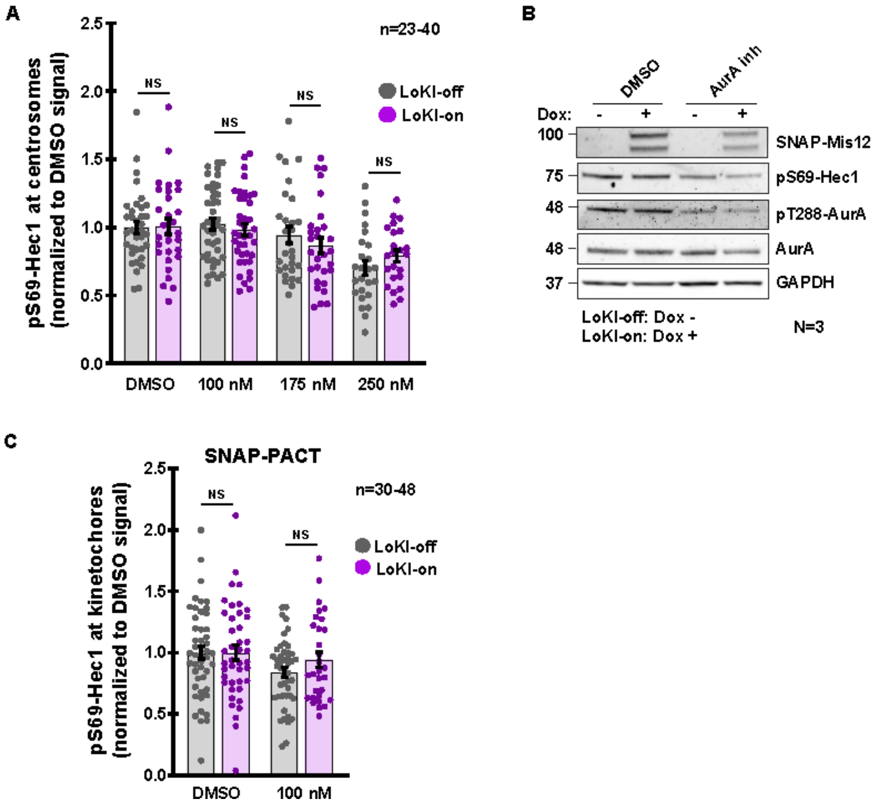

Figure 6-figure supplement 2 Legend: Characterization of AurA inhibition with CLP-MLN8237. (**A**) Quantification of pS69-Hec1 immunofluorescence at centrosomes after 4 hr CLP-MLN8237 treatment. (**B**) Immunoblot detection of pS69-Hec1 (blot 2) and pT288-AurA (blot 3) in Mis12-LoKI-off and Mis12-LoKI-on expressing cells collected via mitotic shake-off. Cells were treated for 16 hr with nocodazole and 4 hr with nocodazole plus DMSO or 100 nM CLP-MLN8237. Total AurA (blot 3), SNAP-PACT (blot 1), and GAPDH (blot 5) are also depicted. (**C**) Quantification of pS69-Hec1 immunofluorescence at kinetochores after 4 hr CLP-MLN8237 treatment in SNAP-PACT expressing U2OS cells. Points in (**A**) and (**C**) represent individual cells (n). Data normalized to DMSO. Experiments were conducted at least three times (N=3) and P values were calculated by unpaired two-tailed Student's t-test. Data are mean ± s.e.m. NS, not significant.

CHAPTER 3: GRAVIN SIGNALING NETWORKS COORDINATE γ-TUBULIN ORGANIZATION AT MITOTIC SPINDLE POLES

3.1 ABSTRACT

Mitogenic signals that regulate cell division often proceed through multi-enzyme assemblies within defined intracellular compartments. The anchoring protein Gravin restricts the action of mitotic kinases and cell-cycle effectors to defined mitotic structures. In this report we discover that genetic deletion of Gravin disrupts proper accumulation and asymmetric distribution of γ-tubulin during mitosis. We utilize a new precision pharmacology tool, Local Kinase Inhibition (LoKI), to inhibit the Gravin binding partner polo-like kinase 1 (Plk1) at spindle poles. Using a combination of gene-editing approaches, quantitative imaging, and biochemical assays we provide evidence that disruption of local Plk1 signaling underlies the γ-tubulin distribution defects observed with Gravin loss. Our study uncovers a new role for Gravin in coordinating γ-tubulin recruitment during mitosis and illuminates the mechanism by which signaling enzymes regulate this process at a distinct subcellular location.

3.2 INTRODUCTION

Spatial biology is an emerging aspect of biomedicine wherein investigators study how the subcellular location of enzymes underlies health and disease (Scott and Pawson 2009; Lemmon et al. 2016). At the molecular level, intracellular targeting of cell signaling enzymes is achieved through the interaction with anchoring, adaptor, or scaffolding proteins (Langeberg and Scott 2015). A-kinase anchoring proteins (AKAPs) are a prototypic example of these signal-organizing proteins that are classified by their ability to anchor protein kinase A (PKA) (Gabrovsek et al. 2017; Tasken and Aandahl 2004); Bucko and Scott, in press). However, numerous studies have identified other classes of protein kinases, phosphatases, small GTPases and effector proteins that are AKAP-binding partners (Esseltine and Scott 2013). Thus, an important function of AKAPs is to provide a locus for the processing, integration, and termination of chemical stimuli by constraining these signaling molecules at defined subcellular locations (Bucko and Scott 2021). Recent findings highlight that AKAPs provide spatial and temporal synchronization of protein kinases that control the mammalian cell cycle. Several multivalent AKAPs such as pericentrin, AKAP450, and Gravin have been implicated in targeting PKA and other signaling enzymes to mitotic structures (Diviani et al. 2000; Chen et al. 2004; Witczak et al. 1999; Canton et al. 2012). For example, during mitosis Gravin anchors Aurora A and polo-like kinase 1 (Plk1) at the spindle poles (Hehnly et al. 2015). We previously showed that mitotic defects and cell-cycle delay ensue upon displacement of either enzyme from the Gravin scaffold. However, given the breadth of targets for these enzymes, a mechanistic dissection of their role in regulating mitotic machinery remains complex.

γ-tubulin participates in various aspects of cell division including centrosome duplication, chromosome segregation, and mitotic progression (Alvarado-Kristensson et al. 2009; Hendrickson et al. 2001; Muller et al. 2006). Importantly, γ-tubulin also initiates nucleation of microtubules at the spindle poles during mitosis (Moritz et al. 1995; Zheng et al. 1995). Aberrant expression and subcellular distribution of γ-tubulin has been documented in several cancers including gliomas, medulloblastomas, breast cancer, and non-small cell lung cancer (Katsetos et al. 2006; Caracciolo et al. 2010; Cho et al. 2010; Niu et al. 2009; Maounis et al. 2012). Thus, gaining greater insight into how γ-tubulin is regulated is paramount to understanding its role in disease and for the development of novel therapeutics that target this protein (Friesen et al. 2012; Chinen et al. 2015).

In this study, we discover that Gravin loss impairs the accumulation of γ-tubulin at the spindle poles during mitosis. We utilize a recently developed precision pharmacology tool, Local Kinase Inhibition (LoKI), to demonstrate that targeted inhibition of centrosomal Plk1, alters the accumulation and asymmetric distribution γ-tubulin at mitotic spindle poles. Finally, we show that deletion of Gravin disrupts the formation of Nedd1/γ-tubulin sub-complexes that are necessary for tubulin ring assembly, thus illuminating a key centrosome-specific function of this anchoring protein.

3.3 RESULTS

Gravin loss perturbs accumulation of γ-tubulin at mitotic spindle poles

Gravin organizes several signaling elements during mitosis (Canton et al. 2012; Canton and Scott 2013; Colicino et al. 2018). Conversely, removal of Gravin disrupts the localization of active kinases at mitotic centrosomes and is associated with spindle defects (Hehnly et al. 2015; Bucko et al. 2019). To ensure the proper assembly of mitotic spindles, γ-tubulin initiates nucleation of microtubules at the spindle poles (Zimmerman et al. 2004). We examined whether cells with genetically ablated Gravin exhibited defects in the expression or localization of this critical spindle assembly component. First, immunoblots of mouse embryonic fibroblasts (MEFs) from wildtype (WT) and Gravin null (-/-) mice established that total cellular protein expression of γ-tubulin was similar for both genotypes (Figure 1A). Next, immunofluorescence detection confirmed that γ-tubulin (magenta) decorates spindle poles in wildtype MEFs during mitosis (Figure 1B). Counterstaining with α-tubulin (green) and DAPI (blue) revealed the mitotic spindle and DNA, respectively (Figure 1B). Strikingly, γ-tubulin is much less concentrated at the spindle poles in Gravin null cells (Figure 1C). Representative heat maps highlight this phenomenon (Figure 1B-E). Likewise, surface plots depicting maximum intensity signals further illustrate this result (Figure 1D-G). Quantitative analysis using integrated intensity measurements revealed 33.4% less γ-tubulin at mitotic spindle poles in Gravin null MEFs as compared to wildtype cells (Figure 1H). Complementary experiments in HeLa cells stably expressing a control or Gravin shRNA provide further evidence for this phenomenon (Figure 1-figure supplement 1A, B). Gravin-depleted HeLa cells display 23.6% less γ-tubulin at the spindle poles than controls (Figure 1-figure supplement 1C). Collectively, these findings reveal that accumulation of γ-tubulin during mitosis is disrupted in cells lacking Gravin.

Generation and validation of genetically engineered human Gravin KO cells

While our initial findings postulate that Gravin loss disrupts γ-tubulin targeting to mitotic spindle poles, it is not clear whether complete deletion of Gravin in human cells produces a similar outcome. To generate Gravin knockout (KO) human lines we used CRISPR/Cas9-mediated genome editing to disrupt the *AKAP12* gene on chromosome 6 in U2OS osteosarcoma cells (Figure 2A). Targets were selected within the exon of *AKAP12* that is shared by all three Gravin isoforms, α, β, and γ (Figure 2A, middle schematic). We employed either a single guide RNA (gRNA) directed toward target 1 (Gravin KO) or a combination of two gRNAs directed toward both targets 1 and 2 (Gravin KO #2) to generate independent Gravin KO cell lines (Figure 2A, bottom schematic).

To validate our clonal cell lines we utilized four complementary approaches. First, Sanger sequencing was used to confirm introduction of indels in Gravin KO clones (Figure 2B). Sequence analysis indicates introduction of a premature stop codon that abolishes the Gravin coding region at target site 1 in our Gravin KO clone (Figure 2B, red sequence). Second, immunoblots detected robust Gravin expression in wildtype cells while a complete loss of the protein was observed in KO lines (Figure 2C). Immunoblot detection of GAPDH served as a loading control (Figure 2C). Removal of Gravin was validated with two separate antibodies against this anchoring protein (Figure 2C, Figure 2-figure supplement 1A). Third, we assessed our genome-edited clones for the presence of micronucleated cells. Micronuclei are structures that contain genetic material outside of the main nucleus and often result from missegregated chromosomes (Leibowitz, Zhang, and Pellman 2015). We used this assessment on the basis of previous studies that established an association between Gravin loss and the formation of micronuclei (Colicino et al. 2018). Our experiments in Gravin-depleted HEK 293 cells demonstrate that micronuclei formation can be used as a functional readout for Gravin loss (Figure 2-figure supplement 1B). Indeed, we observed this phenomenon in our genetically-engineered human U2OS clones as well (Figure 2D-G). Interphase wildtype cells display a low incidence of micronuclei at baseline (Figure 2D).

On the contrary, we observe more micronucleated cells when Gravin is ablated (Figure 2E, F, Figure 2-figure supplement 1C). Gravin loss results in a 2.4-fold increase in the number of micronucleated cells (Figure 2G). This enrichment was further validated in an additional Gravin KO clone (Figure 2-figure supplement 1C). Fourth, additional immunoblotting established that both wildtype and Gravin KO U2OS cell lines express normal levels of γ-tubulin and Plk1, a previously-characterized Gravin interacting partner (Figure 2H). Together, these data provide evidence for an engineered human cell line that lacks the Gravin anchoring protein.

Gravin deletion enhances the asymmetric distribution of γ-tubulin

Gravin governs the asymmetric distribution of protein kinases at mitotic spindle poles (Hehnly et al. 2015). We employed super-resolution structured illumination microscopy (SIM) to examine γ-tubulin organization at each spindle pole. Accordingly, we found that this key microtubule assembly component distributes asymmetrically between the two poles in wildtype MEFs (Figure 3A). This result is further illustrated by representative line plots depicting maximum intensity signals across the x-plane (Figure 3B, C). Quantitative analysis using integrated intensity measurements establish that pole 1 clusters 19.9% more γ-tubulin than pole 2 in wildtype MEF cells (Figure 3D). Parallel analyses recapitulate this phenomenon in wildtype U2OS cells (Figure 3E, Figure 3-figure supplement 1A). These additional studies demonstrated an 18.9% enrichment of γ-tubulin at pole 1 as compared to pole 2 (Figure 3E). These data reveal the asymmetric distribution of γ-tubulin between individual spindle poles in both wildtype murine and human cells.

Loss of Gravin disrupts the recruitment of signaling elements to mitotic spindle poles (Hehnly et al. 2015; Bucko et al. 2019). Therefore, we tested whether Gravin ablation perturbs the distribution of γ-tubulin between the two poles (Figure 3F-K). As before, immunofluorescent staining in wildtype MEFs confirmed an enrichment of γ-tubulin (yellow) at one spindle pole over the other (Figure 3F). Magnified insets and representative surface plots emphasize this result (Figure 3F). Surprisingly, Gravin null MEFs displayed a more pronounced asymmetry in the pole-to-pole distribution of γ-tubulin (Figure 3G). Quantitative methods were employed to further probe this observation. First, integrated intensity measurements were used to quantitate the total γ-tubulin signal at each pole. Then, the γ-tubulin signal at the pole with the lowest intensity was divided by the signal at the pole with the highest intensity giving us the ratio of γ-tubulin between the poles ("lowest/highest pole ratio"). In wildtype MEFs, we calculated a mean lowest/highest pole ratio of 0.811 (Figure 3J). However, in Gravin null cells we observed an average ratio of 0.737 (Figure 3J). Parallel analyses in the CRISPR/Cas9-edited U2OS cells revealed a similar result (Figure 3H, I, K). Wildtype U2OS cells displayed a minor enrichment of γ-tubulin at one pole over the other (Figure 3H). Quantitative analysis of multiple wildtype cells yielded a mean lowest/highest pole ratio of 0.812 (Figure 3K). Consistent with our earlier findings, Gravin KO U2OS cells displayed a ratio of 0.708. Finally, immunoblots established that total γ-tubulin expression was similar between wildtype and Gravin null genotypes in both MEF and U2OS cell lines (Figure 3L). Collectively, these findings suggest that Gravin deletion leads to enhanced asymmetry of γ-tubulin between mitotic spindle poles.

Precision targeting of Plk1 inhibitors to spindle poles promotes asymmetric distribution of active Plk1 and γ-tubulin

Gravin anchors Plk1 during mitosis and depletion of this scaffold reduces the pool of active kinase at the mitotic spindle poles (Hehnly et al. 2015; Bucko et al. 2019). Thus, it is possible that reduced Plk1 activity may contribute to the defects seen in our Gravin null U2OS cells. We previously reported that treatment with the Plk1 inhibitor BI2536 reduces the total levels of pT210-Plk1 (an index of active kinase) at centrosomes (Bucko et al. 2019). Here we examined how the pT210-Plk1 pool that remains after inhibition with BI2536 distributes between the individual poles. In DMSO-treated controls, immunofluorescent detection of pT210-Plk1 revealed a mild enrichment of active kinase at one spindle pole over the other (Figure 4A). Remarkably, inhibition of Plk1 led to greater asymmetry in the pole-to-pole distribution of pT210-Plk1 (Figure 4A). This effect is even more pronounced with increasing concentrations of Plk1 inhibitor (Figure 4A). Representative line plots further illustrate this result (Figure 4B). Integrated intensity measurements were used to quantitate the total pT210-Plk1 signal at the spindle poles for each inhibitor dose (Figure 4C). While DMSO-treated cells display an 18.7% enrichment in pT210-Plk1 at one pole over the other, cells treated with 20 nM BI2536 show a 67.8% difference between the two poles (Figure 4C). These data suggest that inhibition of Plk1 perturbs the distribution of active kinase between the spindle poles.

Since Gravin anchors Plk1 at mitotic spindle poles we assessed whether selective inhibition of Plk1 at this location disrupts the pole-to-pole distribution of active kinase. This was achieved by Local Kinase Inhibition (LoKI), a drug-targeting approach that allows us to deliver the Plk1 inhibitor CLP-BI2536 to centrosomes (Bucko et al. 2019). This precision pharmacology tool allowed us to inhibit Plk1 specifically at spindle poles (Figure 4D). Immunofluorescence detection of pT210-Plk1 assessed the levels of active kinase at each spindle pole (Figure 4E, Figure 4-figure supplement 1A). Control cells express a mutant construct called LoKI-off that is unable to conjugate derivatized kinase inhibitors at spindle poles. When treated with 250 nM CLP-BI2536, these cells display 37.7% less pT210-Plk1 (gray) at pole 2 as compared to pole 1 (Figure 4E, F). Heat plots further emphasize this result (Figure 4E). Strikingly, cells expressing the active LoKI-on targeting platform exhibited 66.1% less pT210-Plk1 at pole 2 as compared to pole 1 when treated with the same concentration of drug (Figure 4E, F). Quantitative analyses established a 1.8-fold greater difference in the distribution of active kinase with spindle pole-targeted inhibitors as comparted to global drug (Figure 4F). Additional controls were conducted in DMSO-treated U2OS cells (Figure 4-figure supplement 1A, B). These studies confirmed that in the absence of drug we observe comparable distributions of pT210-Plk1 between the poles in cells expressing either LoKI targeting platform (Figure 4-figure supplement 1A, B). Additional validation confirmed that the enhanced asymmetry of pT210-Plk1 does not result from redistribution of total Plk1 protein (Figure 4-figure supplement 1C). Together, these data suggest that local targeting of Plk1 inhibitor drugs to mitotic spindle poles leads to enhanced asymmetry in the distribution of active kinase at the spindle poles.

Recruitment of γ-tubulin to centrosomes relies on Plk1 activity (Haren, Stearns, and Luders 2009; Xu and Dai 2011). Consequently, inhibition of Plk1 at this location disrupts γ-tubulin targeting to these structures (Bucko et al. 2019). Thus, a logical next step was to test whether local inhibition of Plk1 enhances the asymmetrical localization of γ-tubulin between the individual spindle poles. Targeted delivery of CLP-BI2536 in LoKI-on cells promoted a more asymmetric distribution of γ-tubulin as compared to DMSO controls (Figure 4G). Magnified insets of each pole further emphasize this result (Figure 4G). Quantitative analysis revealed that the lowest/highest pole ratio for γ-tubulin drops from 0.761 to 0.680 when Plk1 inhibitors are targeted to the mitotic spindle poles (Figure 4H). In contrast, a less pronounced effect was observed when experiments were repeated in LoKI-off cells (Figure 4-figure supplement 1D, E). These precision pharmacology experiments reveal that targeted Plk1 inhibitor drugs lead to an enhanced asymmetric localization of γ-tubulin at mitotic spindle poles.

Gravin ablation diminishes interactions between γ-tubulin and upstream regulators

Nedd1, a member of the γ-tubulin ring complex (γ-TURC), coordinates γ-tubulin accumulation at centrosomes (Haren et al. 2006; Manning et al. 2010). Furthermore, Plk1 promotes the interaction of γ-tubulin with Nedd1 to ensure proper targeting of γ-TURC during mitosis (Zhang et al. 2009). We employed proximity ligation assay (PLA), a technique that marks protein-protein interactions that occur within a range of 40–60 nm, to identify protein interaction pairs in wildtype and Gravin null mitotic cells (Figure 5A-E). Immunofluorescent detection of PLA puncta (green) and DAPI (blue) uncovered Plk1/γ-tubulin interaction pairs in wildtype MEFs (Figure 5A). Significantly fewer PLA puncta were detected in Gravin null cells (Figure 5B). Quantitative analysis reveals a 24% reduction in the number of puncta observed in Gravin null MEFs as compared to wildtype controls (9.8 versus 12.9, respectively; Figure 5C).

Complementary experiments were carried out to assess Nedd1/γ-tubulin protein-protein interactions (Figure 5D-E). Again, immunofluorescent detection identified PLA puncta (yellow) and DAPI (blue) in mitotic cells (Figure 5D). As before, Gravin null MEFs display fewer PLA puncta than wildtype control cells (Figure 5D). Quantitation further revealed that Gravin-depleted cells display 34.8% less PLA puncta than wildtype MEFs (Figure 5E). These findings suggest that Plk1/γ-tubulin and Nedd1/γ-tubulin interactions are reduced in cells lacking Gravin. Thus, abrogation of Plk1-mediated signaling may underlie the abnormalities in γ-tubulin accumulation observed in Gravin null cells (Figure 5F).

3.4 DISCUSSION

Subcellular targeting and anchoring of protein kinases is a recognized molecular mechanism that enhances the precision and fidelity of protein phosphorylation events (Langeberg and Scott 2015). Gravin regulates various aspects of mitosis including the clustering of mitotic protein kinases to facilitate spindle formation and mitotic progression (Nauert et al. 1997; Gelman 2010; Hehnly et al. 2015). In this study, we discover a new role for this anchoring protein in modulating the recruitment of γ-tubulin, a major regulator of microtubule nucleation. Our imaging studies in Figure 1 reveal that loss of Gravin perturbs the accumulation of γ-tubulin at mitotic spindle poles. Elevated expression and ectopic cellular distribution of γ-tubulin has been observed in astrocytic gliomas (Katsetos et al. 2006). Delocalization of this key microtubule-nucleating component has also been detected in human breast cancer, with the most dramatic changes occurring in tumor cell lines that encompass the greatest metastatic potential (Cho et al. 2010). Both reports conclude that inappropriate subcellular distribution of γ-tubulin is associated with tumor progression. Our findings argue that Gravin-mediated signaling further contributes to this process. Other investigators have shown that Gravin loss is linked to defective mitoses in a variety of cancer cell lines (Gelman 2010; Parada et al. 2018). Recent phosphoproteomics studies further implicate this anchoring protein as a potential prognostic biomarker for high-grade meningiomas

(Gelman 2010; Parada et al. 2018). Our discovery that Gravin-ablated cells display an enhanced pole-to-pole asymmetry of γ-tubulin provides additional clues into how protein scaffolds safeguard cell division events (Figure 3F-K). Thus, we postulate that Gravin may serve a protective role during mitosis by ensuring the proper localization of γ-tubulin at mitotic spindle poles. Collectively, these studies suggest that precise targeting of mitotic signaling components contributes to the fidelity of cell division.

Polo-like kinase 1 is a promising target for therapeutic intervention in cancer (Steegmaier et al. 2007; Choi et al. 2015; Lee et al. 2015; Gutteridge et al. 2016; Cheng et al. 2018). This enzyme catalyzes phosphorylation events necessary for the efficient and accurate progression of cells through mitosis (Barr, Sillje, and Nigg 2004; Lens, Voest, and Medema 2010; Combes et al. 2017). While ATP-competitive kinase inhibitors such as BI2536 are putative anticancer compounds that have entered clinical trials, conventional approaches for delivering these drugs increase off-target effects and mask contribution of Plk1 at specified subcellular locations (Steegmaier et al. 2007; Lenart et al. 2007; Klaeger et al. 2017). With this in mind we reasoned that manipulating molecular scaffolds such as Gravin could offer new insight into how locally-constrained signaling enzymes are regulated. Moreover, pharmacological strategies that inhibit kinase activity within a specified locale permit the investigation of individual signaling events. Here, we demonstrate an application of the new precision pharmacology tool, LoKI, by targeting kinase inhibitor drugs to the subcellular location where Gravin anchors Plk1 (Bucko et al. 2019; Kawashima and Newton 2020). The rationale for utilizing LoKI targeting was provided by previous reports that have implicated a role for Plk1 in organizing γ-tubulin at mitotic centrosomes (Lane and Nigg 1996; Haren et al. 2006; Xu and Dai 2011; Bucko et al. 2019). A key advance, illustrated in Figure 4, is that suppression of Plk1 activity at mitotic spindle poles enhances the asymmetric distribution of γ-tubulin. By taking advantage of the spatial resolution afforded by the LoKI system we discover that selective loss of Plk1 action at spindle poles perturbs the distribution of γ-tubulin. In addition, the data in Figure 4E-H uncover a link between loss of Plk1 activity at the spindle poles and an enhanced asymmetric distribution of γ-tubulin. On the basis of these results, it is possible that dampened Plk1 activity at mitotic spindle poles underlies the γ-tubulin accumulation defects observed in cells lacking Gravin. Alternatively, Gravin may facilitate phosphorylation of yet unknown mitotic substrates that regulate γ-tubulin targeting. Irrespective of either mechanism, our findings advance the concept that Gravin-anchored kinase activity is necessary to optimally regulate the distribution of a central γ-tubulin ring complex (γ-TURC) component during mitosis.

AKAPs constrain enzymes within spatially restricted signaling islands to restrict kinases and phosphatases to the immediate vicinity of select substrates (Smith et al. 2017; Smith et al. 2013; Nygren et al. 2017). Our previous reports showed that Gravin organizes Plk1 and Aurora A kinases at spindle poles to facilitate proper spatial relay of signaling during mitosis (Hehnly et al. 2015; Bucko et al. 2019). A new concept emerging from this study is that cells without Gravin have lost the necessary protein-protein interactions to drive robust localization of γ-tubulin at spindle poles. This is supported by data in Figure 5D-E showing that γ-tubulin interaction with Nedd1, a Plk1 substrate, is disrupted in Gravin null cells. On the basis of these findings we conclude that inappropriate targeting of Plk1 activity in Gravin-ablated cells may contribute to the loss of γ-tubulin/Nedd1 interactions. Moreover, our data is in line with a recent study which discovered that increased Plk1 mobility in Gravin-depleted cells results in aberrant phosphorylation of CEP215, a PCM component that regulates the assembly of the γ-tubulin ring complex (γ-TURC) (Colicino et al. 2018). Since Plk1 promotes the interaction of γ-tubulin with Nedd1, it is possible that loss of this interaction in Gravin null cells drives the disruptions in γ-tubulin accumulation that we observe (Zhang et al. 2009). Thus, our findings in Figure 5 offer additional mechanistic insight into how Gravin organizes signaling complexes at specific subcellular location to ensure that kinases are positioned in close proximity to their targets.

A recognized facet of AKAPs is their ability to work within spatially restricted microenvironments to direct and insulate kinase action within a few angstroms of their intended targets (Smith et al. 2017; Smith et al. 2018). Kinase anchoring is particularly effective for the modulation of a highly coordinated process such as the cell cycle (Fulcher and Sapkota 2020). Thus, it is perhaps not surprising that subtle perturbations in the organization of key macromolecular complexes are responsible for certain defective signaling events that are observed in a range of cancers (Bucko and Scott 2021). This is evidenced by studies that have identified the *AKAP12* gene, which encodes Gravin, in a deletion hotspot for a variety of human cancers (Xia et al. 2001). However, it is equally worth noting that elevated levels of Gravin in ovarian cancer have been correlated with poor prognosis (Bateman et al. 2015). Thus, more studies are necessary to clarify the role of Gravin in these different pathological contexts. Another theme emerging from our work is that deploying tools that direct kinase inhibitors to specific subcellular locations provide clues into the contributions of local signaling events. This study provides a practical application of the LoKI system and demonstrates that precision pharmacology can be utilized to decipher how anchored Plk1 activity at the spindle poles drives the asymmetric distribution of γ-tubulin. Together, our findings lead us to speculate that perturbation of Gravin signaling during mitosis may underlie disease progression. However, future work is necessary to uncover additional Gravin binding partners and downstream substrates that become dysregulated when this anchoring protein is ablated in disease contexts.

3.5 METHODS

Reagents

A detailed list of reagents is presented in “Chapter 3 Key Resource Table” of Appendix

Plasmid constructs

Constructs for the generation of LoKI cells were generated as described in (Bucko et al. 2019). In brief, LoKI constructs contain an N-terminal mCherry reporter protein, two SNAP-tag domains, and a PACT (AKAP450 centrosomal targeting) sequence. The second SNAP-tag has a varied codon sequence to simplify PCR-amplification. Individual components were PCR amplified with overlapping ends and/or Gateway “att” sites and assembled using Gibson Cloning. Constructs were subcloned into pLIX402 (a gift from David Root; Addgene plasmid #41394) using Gateway Cloning. Mutant LoKI vectors were generated by performing site-directed mutagenesis with a QuikChange II XL kit (Aligent). Constructs were verified by Sanger sequencing.

Cell culture

U2OS cells used to generate stable cell lines (Bucko et al. 2019) were purchased from ATCC and tested negative for mycoplasma contamination as assessed by the Universal Mycoplasma Detection Kit (ATCC 30-1012K). U2OS, Control and Gravin shRNA HeLa (Hehnly et al. 2015)), Control and Gravin shRNA HEK293 ((Canton et al. 2012)) and immortalized MEF (generated as described in (Hehnly et al. 2015)) cells were maintained in DMEM, high glucose (Life Technologies) at 37°C and 5% CO2. All media was supplemented with 10% FBS. Infections for generation of stable knockdown in HeLa and HEK293 cells were performed with shRNA lentiviral particles (Santa Cruz Biotech). Infections for generation of stable LoKI cells were performed using lentiviral particles created in-house (as described in (Bucko et al. 2019)).

CRISPR-Cas9 editing of Gravin

CRISPR/Cas9-mediated genome editing was used to delete the AKAP12 gene on chromosome 6 in U2OS cells. Two unique guide RNAs (gRNAs) were designed to the following targets: gRNA1, AGAGATGGCTACTAAGTCAG**CGG**; gRNA 2, AGCCGAATCTGGCCAAGCAG**TGG**. Bold letters indicate PAM sequence. Constructs expressing Cas9 and either gRNA were generated by cloning into pSpCas9(BB)-2A-Puro (PX459) vectors (Addgene plasmid #48139). Individual vectors were transfected into U2OS cells using TransIT-LT1 reagent (Mirus) in Opti-MEM® (Life Technologies) media according to manufacturer's instructions. Single clones were isolated using Scienceware cloning discs (Sigma-Aldrich). Clones were first screened by immunoblotting for loss of Gravin protein expression using two independent antibodies. Clones that had undetectable levels of Gravin were further checked for mutations. In brief, cells were pelleted and purification of genomic DNA was achieved by treating with 50 mM NaOH for 20 minutes at 95°C followed by treatment with 1M Tris pH 8.0 and a 10 minutes spin at 14,000 rpm. Primers flanking the target sites were designed and the region was amplified by PCR. Primer sequences are designated in the Key Resources Table. PCR products were cloned into vectors using the Zero Blunt™ TOPO™ PCR Cloning Kit (Thermo Fisher). Individual clones were isolated for plasmid DNA mini-prep and verified by Sanger sequencing.

Drug treatments

BI2536 (AdooQ) and CLP-BI2536 (Bucko et al. 2019) were used to inhibit Plk1. For LoKI experiments, cells were treated as described in (Bucko et al. 2019). In brief, prior to drug treatment, cells were incubated with 1 µg/mL doxycycline hyclate (Sigma-Aldrich) in FBS-supplemented DMEM for 48-72 hours to induce expression of LoKI targeting platforms. Cells were grown on 1.5 poly-D-lysine coated coverslips (neuVitro) for ~16 hours in complete DMEM and then treated with DMSO or CLP-BI2536 in serum-free DMEM for 4 hours. For washout experiments (γ-tubulin data), cells were incubated in serum-free DMEM without inhibitors for an additional 1 hour. Cells were washed once with PBS prior to fixation.

Immunoblotting

Cells were lysed in RIPA buffer (50 mM Tris HCl pH 7.4, 1% Triton X-100, 0.5% Sodium Deoxycholate, 0.1% SDS, 50 mM NaF, 120 mM NaCl, 5 mM β-glycerophosphate) with protease and phosphatase inhibitors (1 mM benzamidine, 1 mM AEBSF, 2 µg/mL leupeptin, 100 nM microcystin-LR). Samples were boiled for 5 minutes at 95°C in NuPAGE™ LDS Sample Buffer 4X (Thermo Fisher) + 5% BME (Sigma-Aldrich) and protein concentration was determined using a Pierce™ BCA Protein Assay Kit (Thermo Fisher). Samples were resolved on Bolt® 4-12% Bis-Tris Plus Gels (Invitrogen), proteins were transferred to nitrocellulose for immunoblotting, and membranes were probed with primary antibodies. Detection was achieved with a HRP-conjugated rabbit or mouse secondary antibody (GE Healthcare) followed by enhanced chemiluminescence with SuperSignal™ West Pico PLUS Chemiluminescent Substrate (Thermo Fisher). Representative blots were adjusted for brightness and contrast in Fiji.

Immunofluorescence

Cells grown on 1.5 poly-D-lysine coated coverslips (neuVitro) for ~16 hours were fixed in ice-cold methanol or in 4% paraformaldehyde in PBS for 10 minutes. Cells were permeabilized and blocked in PBS with 0.5% Triton X-100 and 1% BSA (PBSAT) for 30 minutes. Primary antibodies and secondary antibodies, conjugated to Alexa Fluor dyes (Invitrogen), were diluted in PBSAT and cells were stained for 1 hour in each. Counterstaining with FITC-tubulin antibodies and/or DAPI was carried out for 10-45 minutes in PBSAT. Washes with PBSAT were carried out in one of two ways (3X for 5 minutes or 10X, quick on and off) between antibody and/or dye incubation steps and prior to mounting. Coverslips were mounted on slides using ProLong® Diamond Antifade Mountant (Life Technologies).

Proximity Ligation Assay

Cells were methanol-fixed, permeabilized, blocked, and stained with primary antibodies as described under “immunofluorescence”. Cells were incubated with anti-rabbit and anti-mouse probes (Duolink) and PLA was carried out according to manufacturer’s instructions. Where applicable, cells were counterstained as described above.

Microscopy

Widefield and super-resolution 3D-SIM images were acquired on a Deltavision OMX V4 (GE Healthcare) system equipped with a 60x/1.42 NA PlanApo oil immersion lens (Olympus), 405-, 488-, 568-, and 642-nm solid-state lasers and sCMOS cameras (pco.edge). For SIM, 15 images per optical slice (3 angles and 5 phases) were acquired. Image stacks of 4-7 µm with 0.200 (widefield) or 0.125-µm (SIM) optical thick z-sections were acquired using immersion oil with a refractive index 1.516 or 1.518. Z-stacks were generated using the DAPI or α-tubulin channels to define the upper and lower boundaries of the plane with a 0.5 µm step size. SIM images were reconstructed using Wiener filter settings of 0.003 and optical transfer functions measured specifically for each channel with SoftWoRx software (GE Healthcare) were used to obtain super-resolution images with a two-fold increase in resolution both axially and laterally. Images from different color channels were registered using parameters generated from a gold grid registration slide (GE Healthcare) and SoftWoRx. Widefield images were deconvolved using SoftWoRx. For micronuclei counts and acquisition of DIC images for PLA assays, a DM16000B inverted microscope (Leica) equipped with a 63x Plan-Apocromat NA 1.4 oil objective, a CSU10 confocal spinning disk (Yokogawa) and a CoolSnap HQ camera (Photometrics) controlled by MetaMorph 7.6.4 (Molecular Devices) was used. Representative images were adjusted for brightness and contrast in Fiji.

Image Analysis

SoftWoRx (GE Healthcare) or NIH ImageJ (Fiji) software was used to generate maximum intensity projections from z-stack images. Immunofluorescence signals were measured using Fiji software. For analysis of immunofluorescence at spindle poles, sum slice 32-bit Tiff projections were generated from z-stack images. The oval selection tool in Fiji was used to draw a circle (ROI) around the spindle pole and measure the signal in the 647 (γ-tubulin) channel. The area of the circle remained consistent for all experimental replicates. Using the measure function in Fiji, with “Area” and “Raw Integrated Density” predefined as measurements, values were recorded for each spindle pole and for a nearby background region. Total signal at spindle poles: The average raw integrated density for the spindle poles was determined by adding together the raw integrated densities for each pole in a cell and dividing that value by two. The integrated density for the background was subtracted from the average spindle pole integrated density to yield a background-subtracted average integrated density signal. In cases of a negative value (when background signal is higher than that at poles), a value of zero was reported. An average spindle pole signal was calculated for each control and experimental condition. To do this, normalized average integrated densities were added together and divided by the total number of cells for a given condition. This resulted in a value representing the background-normalized average integrated density at the spindle poles. Values for Gravin null and drug-treated cells were normalized to wildtype or DMSO-treated controls, respectively. **Signal at individual spindle poles:** The individual raw integrated densities for each spindle pole in a given cell were classified into two categories: pole 1 (the spindle pole that contains the highest fluorescence signal) and pole 2 (the pole with the lowest fluorescence signal). The background signal values were subtracted from each individual pole. As before, negative values were replaced with a zero. Values for the low pole were normalized to average high pole values of each corresponding condition. **Lowest/highest pole ratios:** Background-subtracted integrated intensity values were used to determine the total γ-tubulin signal at each pole. The immunofluorescence signal of the pole with the lowest intensity was divided by the signal of the pole with the highest intensity to determine the ratio of γ-tubulin between the poles. In cases where the value for the ratio was zero, the value was removed and not included in statistical analysis. This was to avoid misinterpretation of the data since a value of zero at both poles and a high value at pole 1 but a zero value at pole 2 would both yield the same ratio. **Micronuclei analysis:** For each experimental replicate, 500 interphase cells were examined using the DAPI channel. The number of cells with micronuclei was divided by 500 to determine the percent of micronucleated cells per experiment. **PLA analysis:** The number of PLA puncta per cell was quantified using the cell counter tool in Fiji. **Surface and line plots:** Plots were generated in Fiji software from maximum intensity projections of representative images using the 3D Surface Plot function or the Plot Profile function. The Image J "fire" LUT setting was used to generate pseudo-color images.

Statistical analysis

Statistics were performed using an unpaired two-tailed Student's t-test or a one-way ANOVA in GraphPad Prism software. All values are reported as mean ± standard error of the mean (s.e.m) with p-values less than 0.05 considered statistically significant. Number of independent experiments (N) and number of individual points over several experiments (n) are presented. Detail analyses are presented in the "Chapter 3 Statistical Analyses Table" of Appendix.

Sample size and replicates

The sample size was not statistically determined. Where applicable, $n > 20$ independent measurements were conducted across $N \geq 3$ independent experiments. For micronuclei experiments in Gravin KO #2 (Figure 2-figure supplement 1C) at least 1000 cells per condition over 2 independent experiments were assayed.

3.6 ACKNOWLEDGEMENTS

This chapter contains experiments from work that is currently under review: Bucko PJ, Garcia I, Manocha R, Bhat A, Worderman L, and Scott JD. Gravin signaling networks coordinate γ-tubulin organization at mitotic spindle poles. Special thanks to Irvin Garcia for carrying out proximity ligation assays. Thank you to Patrina Pellett (previously at GE Healthcare) for assistance with super-resolution imaging techniques, Juan-Jesus Vincente in Linda Wordeman's lab (UW) for help with experimental design, data analysis, and thoughtful discussion, and to members of the Scott lab for critical discussions.

3.7 FIGURES

Figure 1:

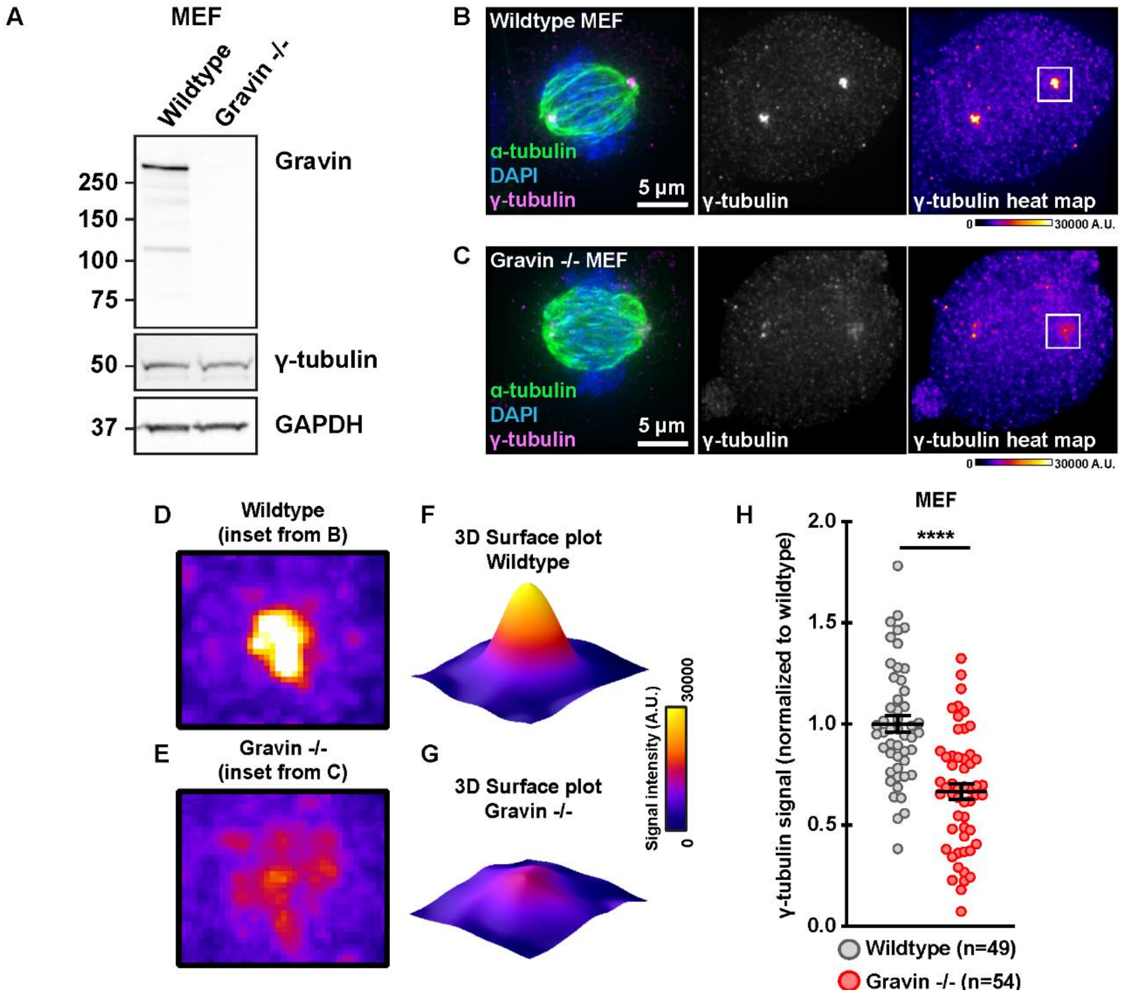

Figure 1 Legend: Loss of Gravin reduces γ-tubulin accumulation at mitotic spindle poles. (**A**) Immunoblot detection of Gravin (top), γ-tubulin (middle), and GAPDH (bottom) in wildtype and Gravin null (-/-) mouse embryonic fibroblasts (MEFs). (**B, C**) Immunofluorescence of representative wildtype (**A**) and Gravin -/- (**B**) mitotic cells. Composite images (left) show α-tubulin (green), DAPI (blue), and γ-tubulin (magenta). Distribution of γ-tubulin is presented in grayscale (middle) and as pseudo-color heat maps (right). Signal intensity scale (A.U.) is shown below. (**D, E**) Magnified heat-maps from image insets in B and C (white boxes) highlight γ-tubulin signal in wildtype (**D**) and Gravin -/- (**E**) cells. (**F, G**) Surface plots representing signal intensity of γ-tubulin in wildtype (**F**) and Gravin -/- (**G**) cells. (**H**) Quantification of γ-tubulin immunofluorescence at spindle poles in wildtype (gray) and Gravin -/- (red) MEFs. Points represent individual cells (n). Data are normalized to wildtype controls; wildtype, n=49, Gravin -/-, n=54, ****p<0.0001; Experiments were conducted four times (N=4). P values were calculated by unpaired two-tailed Student's t-test. Data are mean ± s.e.m.

Figure 1-figure supplement 1:

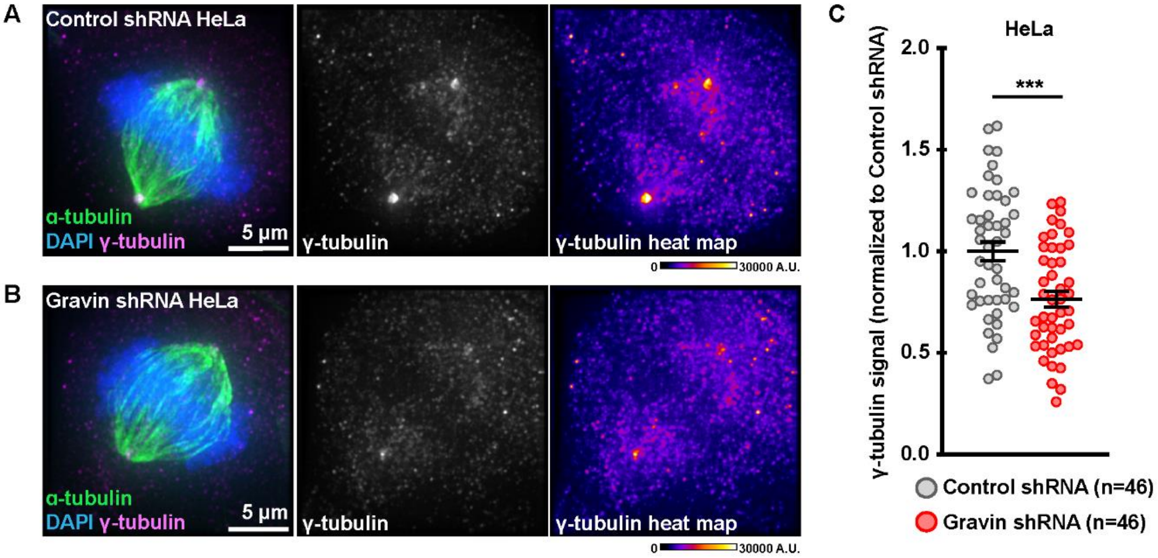

Figure 1-figure supplement 1 Legend: Loss of Gravin in HeLa cells perturbs accumulation of γ-tubulin at mitotic spindle poles. (**A, B**) Immunofluorescence of representative control shRNA (**A**) and Gravin shRNA (**B**) mitotic HeLa cells. Composite images (left) show α-tubulin (green), DAPI (blue), and γ-tubulin (magenta). Distribution of γ-tubulin is represented in grayscale (middle) and with pseudo-color heat maps (right). Signal intensity scale (A.U.) is shown below. (**C**) Quantification of amalgamated γ-tubulin immunofluorescence data at spindle poles in control shRNA (gray) and Gravin shRNA (red) HeLa cells. Points represent individual cells (n). Data are normalized to control shRNA; control shRNA, n=46, Gravin shRNA, n=46, ***p=0.0002; Experiments were conducted three times (N=3). P values were calculated by unpaired two-tailed Student's t-test. Data are mean ± s.e.m.

Figure 2:

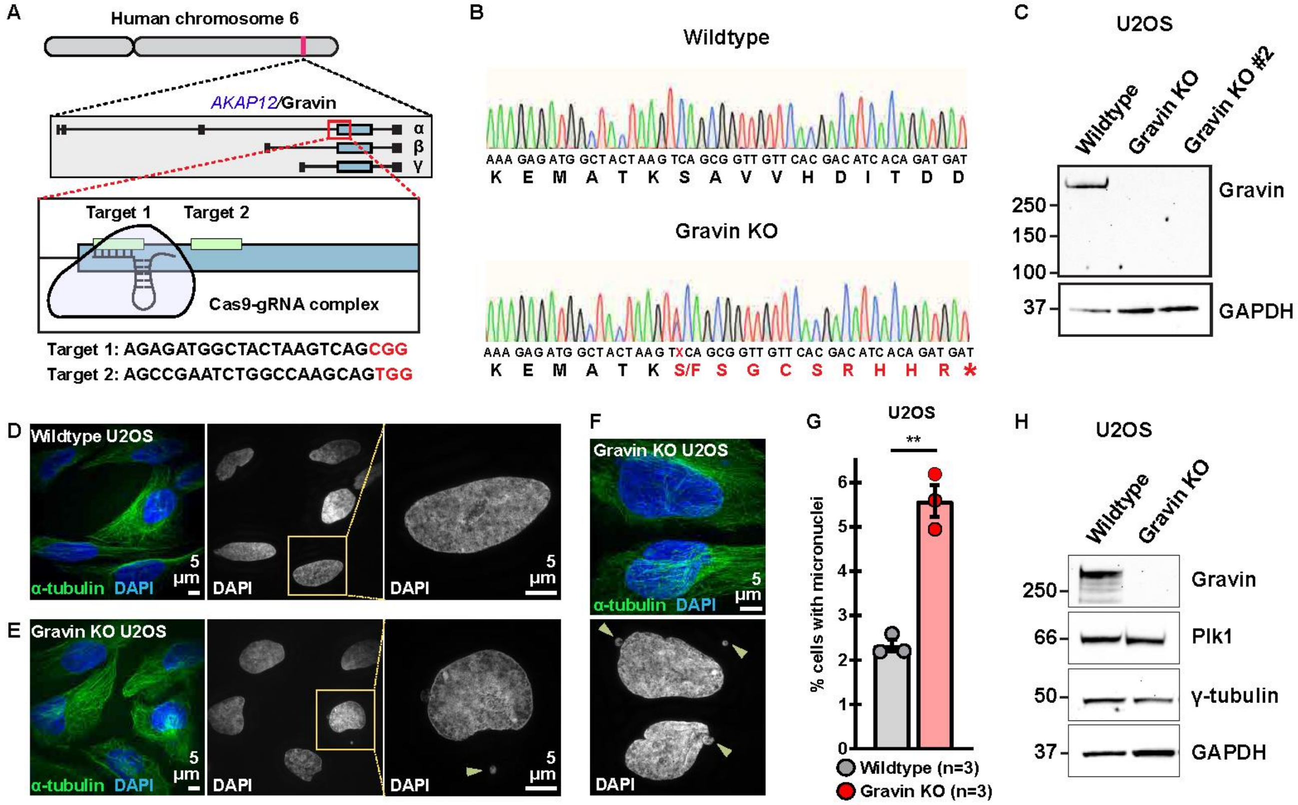

Figure 2 Legend: Generation of Gravin knockout U2OS cells. (**A**) CRISPR-Cas9 gene editing of human chromosome six in U2OS cells to disrupt the Gravin-encoding gene, *AKAP12* (top). Targets are directed to the exon that is shared by all three Gravin isoforms, α, β, and γ (middle). Two unique guide RNAs (gRNAs) were designed to targets 1 and 2 (bottom). Target sequences are presented bellow with PAM sites highlighted in red. (**B**) Traces depicting nucleic (small letters) and amino (large letters) acid sequences for a representative wildtype (top) and Gravin KO (bottom) clone. A mutation present in Gravin KO cells alters the protein coding sequence (red) to generate a premature stop codon (asterisk) and lead to a truncated protein. Traces represent pooled allele sequences for each individual clone. Two amino acid alterations were detected (S or F). (**C**) Immunoblot detection of Gravin (top) and GAPDH (bottom) in wildtype and Gravin KO clonal U2OS cells. (**D-F**) Structured illumination microscopy (SIM) images of wildtype (**D**) and Gravin KO (**E, F**) cells during interphase. Composite images (left) show α-tubulin (green) and DAPI (blue). DAPI stain depicted in grayscale (middle). Magnified insets (right) and yellow arrows highlight micronuclei. (**G**) Quantification of amalgamated data representing the percent (%) of cells with micronuclei in wildtype (gray) and Gravin KO (red) U2OS cells. Points depict individual experiments (n); wildtype, n=3, Gravin KO, n=3, **p=0.001; A total of 1500 cells were analyzed over three independent experiments. P values were calculated by unpaired two-tailed Student's t-test. Data are mean ± s.e.m. (**H**) Immunoblot detection of Gravin (blot 1), Plk1 (blot 2), γ-tubulin (blot 3), and GAPDH (blot 4) in wildtype and Gravin KO U2OS cells.

Figure 2-figure supplement 1:

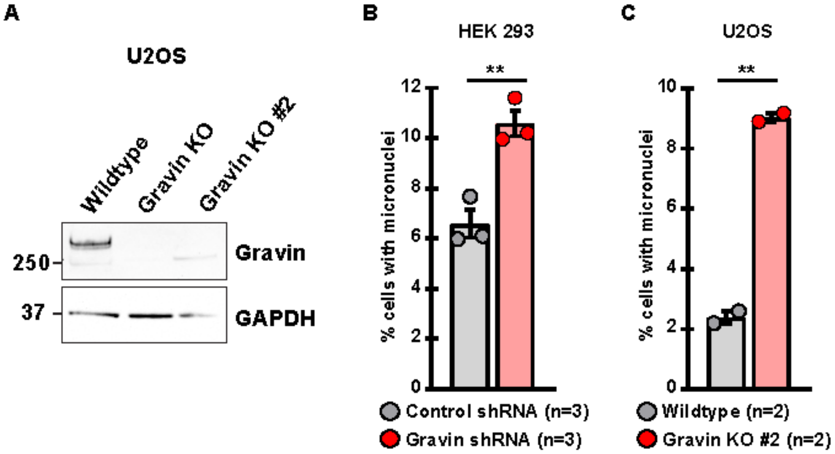

Figure 2-figure supplement 1 Legend: Further validation of Gravin knockout U2OS cells. (**A**) Immunoblot detection of Gravin (top) using a rabbit antibody and GAPDH (bottom) in wildtype and Gravin KO clonal U2OS cells. (**B, C**) Quantification representing the percent (%) of cells with micronuclei in HEK 293 (**B**) and wildtype and CRISPR/Cas9-edited U2OS clone 2 (**C**) cells. Points depict individual experiments (n); (**B**) control shRNA, n=3, Gravin shRNA, n=3, **p=0.0059; (**C**) wildtype, n=2, Gravin KO, n=2, **p=0.0014. A total of 1500 (**B**) or 1000 (**C**) cells were analyzed over three (**B**) or two (**C**) independent experiments. P values were calculated by unpaired two-tailed Student's t-test. Data are mean ± s.e.m.

Figure 3:

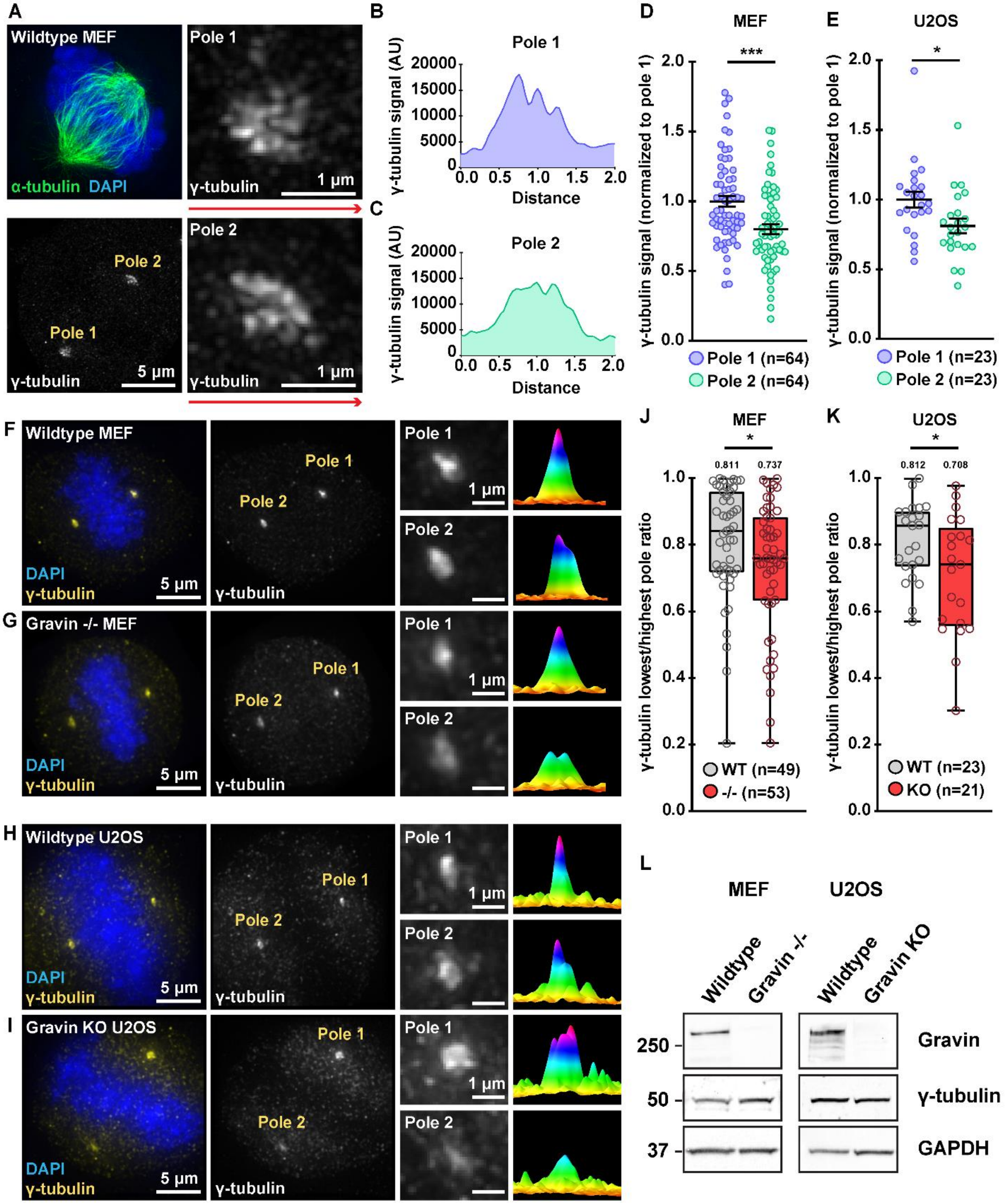

Figure 3 Legend: Deletion of Gravin enhances the asymmetric distribution of γ-tubulin. (**A**) SIM micrograph of a wildtype MEF during mitosis. Composite images (top left) show α-tubulin (green) and DAPI (blue). Grayscale images depict γ-tubulin at both pole (bottom left). Magnified

images reveal that pole 1 (top right) accumulates more γ-tubulin than pole 2 (bottom right). (**B, C**) Signal intensity (y-axis) is graphed against distance (x-axis) to generate plot profiles of maximum intensity signal measurements. Distance along red lines in A were used to generate representative plot profiles for pole 1 (**B**) and pole 2 (**C**). (**D, E**) Quantification of γ-tubulin immunofluorescence at pole 1 (blue) and pole 2 (green) for MEF (**D**) and U2OS (**E**) mitotic cells; (**D**) pole 1, n=64, pole 2, n=64, ***p=0.0002; (**E**) pole 1, n=23, pole 2, n=23, *p=0.0181. (**F-I**) Immunofluorescence of representative wildtype MEF (**F**), Gravin -/- MEF (**G**) wildtype U2OS (**H**) and Gravin KO (**I**) mitotic cells. Composite images (far left) show DAPI (blue) and γ-tubulin (yellow). Grayscale images (middle left) depict γ-tubulin at poles. Magnified insets (middle right) show signals at individual poles. Surface plots (far right) depict signal intensity profiles of each pole. (**J, K**) Quantification of γ-tubulin immunofluorescence at each pole represented as box plots showing lowest/highest pole ratio in wildtype (gray) and Gravin null (red) MEF (**J**) and U2OS (**K**) mitotic cells. Mean values are indicated above each plot; (**J**) WT, n=49, -/-, n=53, *p=0.0438; (**K**) WT, n=23, KO, n=21, *p=0.0263. Points in **D, E, J** and **K** represent individual cells (n). Data in **D** and **E** are normalized to pole 1. Experiments were conducted at least three times (N=3). P values were calculated by unpaired two-tailed Student’s t-test. Data are mean ± s.e.m. (**L**) Immunoblot detection of Gravin (top), γ-tubulin (middle), and GAPDH (bottom) in wildtype and Gravin null MEF (left) and U2OS (right) cells.

Figure 3-figure supplement 1:

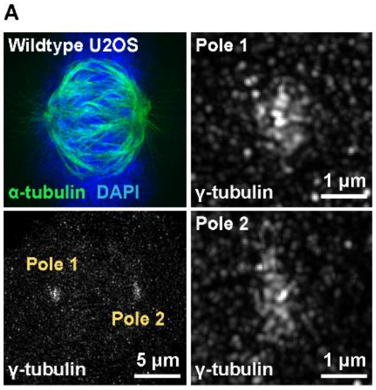

Figure 3-figure supplement 1 Legend: Pole-to-pole distribution of γ-tubulin in wildtype U2OS cells. (**A**) SIM micrograph of a representative wildtype U2OS cell during mitosis. Composite image (top left) shows α-tubulin (green) and DAPI (blue). Grayscale image depicts γ-tubulin at both poles (bottom left). Magnified images reveal that pole 1 (top right) accumulates more γ-tubulin than pole 2 (bottom right).

Figure 4:

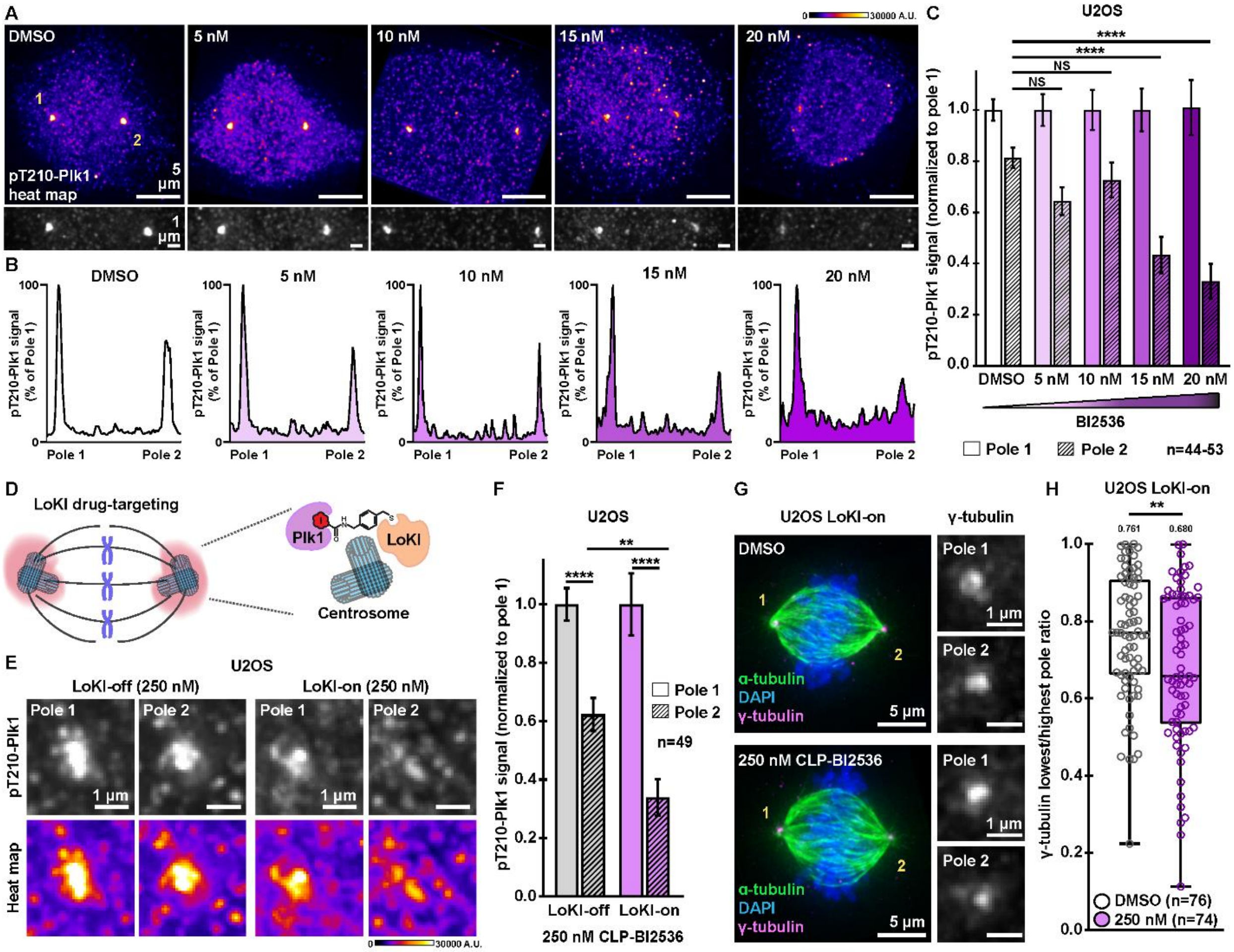

Figure 4 Legend: Targeting Plk1 inhibitors to spindle poles promotes a more asymmetric distribution of active Plk1 and γ-tubulin. (**A**) Immunofluorescence detection of pT210-Plk1 (an index of kinase activity) at mitotic spindle pole in parental U2OS cells treated with DMSO or BI2536 for 4 hr. Distribution of pT210-Plk1 is represented with pseudo-color heat maps (top) and in grayscale (bottom). Signal intensity scale (A.U.) is shown above. (**B**) pT210-Plk1 signal (grayscale from A) is graphed against distance to generate plot profiles of maximum intensity signal measurements. Peaks are normalized to pole 1. BI2536 concentrations are indicated. (**C**) Quantification of amalgamated pT210-Plk1 immunofluorescence at each pole for U2OS parental cells treated with DMSO or BI2536; pole 2, DMSO, n=53, control; 5nM, n=44, p=0.1387; 10 nM, n=44, p=0.7016; 15 nM, n=44, ****p<0.0001; 20 nM, n=44, ****p<0.0001. (**D**) Schematic of precision drug targeting of Plk1 inhibitor to spindle poles (pink) using the Local Kinase Inhibition (LoKI) system. (**E**) Immunofluorescence of pT210-Plk1 at individual spindle poles in representative LoKI-off (left) and LoKI-on (right) U2OS cells treated with 250 nM CLP-BI2536 for 4 hr. Signal of active kinase is represented in grayscale (top) and with pseudo-color heat maps (bottom). Signal intensity scale (A.U.) is shown below. (**F**) Quantification of amalgamated pT210-Plk1 immunofluorescence at each pole after 4 hr of targeted BI2536 delivery; LoKI-off, pole 1, n=49, LoKI-off, pole 2, n=49, ****p<0.0001; LoKI-on, pole 1, n=49, LoKI-on, pole 2, n=49, ****p<0.0001; LoKI-off, pole 2, n=49, LoKI-on, pole 2, n=49, **p=0.0010. (**G**) Immunofluorescence

of a LoKI-on mitotic cell treated with DMSO (top) or 250 nM CLP-BI2536 (bottom) for 4 hr. Composite images (left) show α-tubulin (green), DAPI (blue), and γ-tubulin (magenta). Magnified grayscale images (right) show γ-tubulin signal at poles. (**H**) Quantification of amalgamated γ-tubulin immunofluorescence data at each pole. Data is represented as box plots showing lowest/highest pole ratio for LoKI-on cells after 4 hr treatment with DMSO (white) or 250 nM CLP-BI2536 (purple) followed by a 1 hr washout. Mean values are indicated above each plot; DMSO, n=76, 250 nM, n=74, **p=0.0074. Values depicted in **C**, **F** and **H** represent individual cells (n). Data in **C** and **F** are normalized to pole 1. Experiments were conducted at least three times (N=3). P values were calculated by one-way ANOVA with Dunnett's multiple comparisons test performed with pole 2 DMSO as control (**C**) or unpaired two-tailed Student’s t-test (**F**, **H**). Data are mean ± s.e.m. NS, not significant.

Figure 4-figure supplement 1:

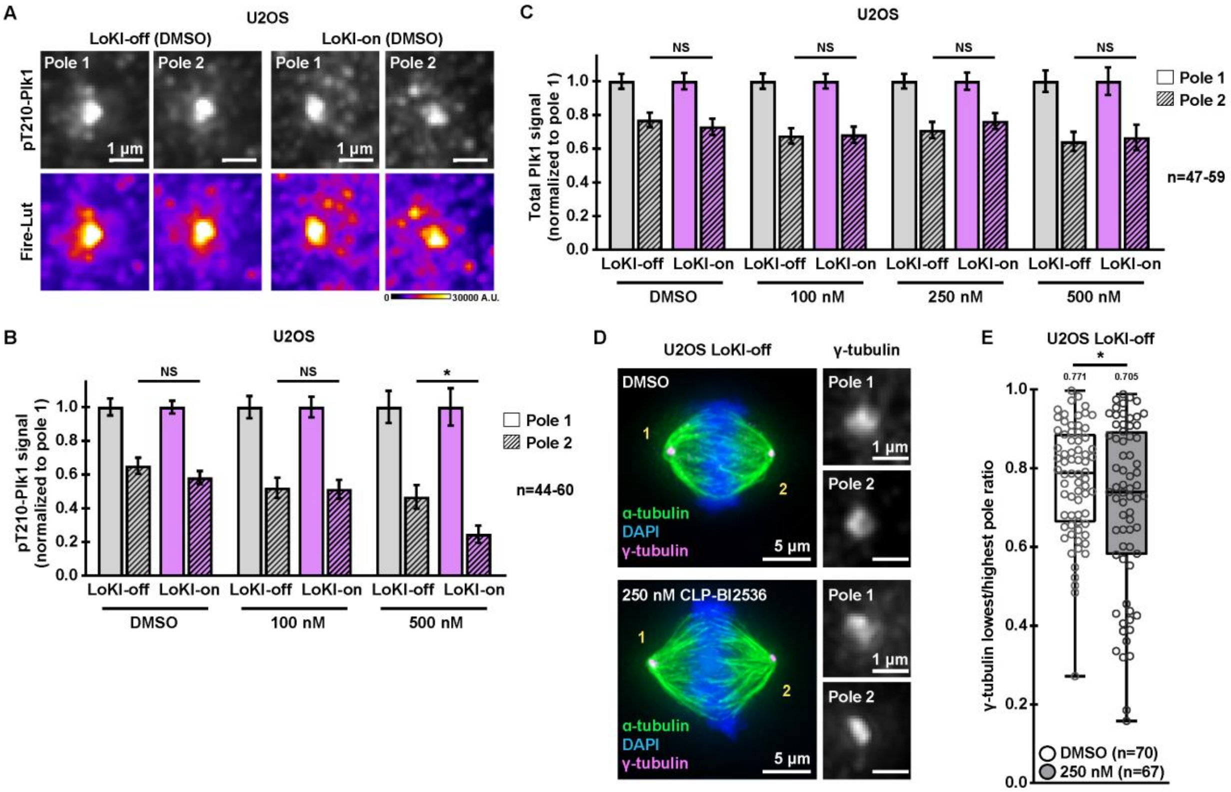

Figure 4-figure supplement 1 Legend: Plk1 inhibition promotes an asymmetric distribution of active kinase and γ-tubulin. (**A**) Immunofluorescence of pT210-Plk1 at individual spindle poles in representative LoKI-off (left) and LoKI-on (right) U2OS cells treated with DMSO for 4 hr. Signal of active kinase is represented in grayscale (top) and with pseudo-color heat maps (bottom). Signal intensity scale (A.U.) is shown below. (**B**) Quantification of pT210-Plk1 immunofluorescence at each pole after 4 hr treatment with DMSO or CLP-BI2536; pole 2: DMSO, LoKI-off, n=44, LoKI-on, n=60, p=0.2477; 100 nM, LoKI-off, n=46, LoKI-on, n=59, p=0.9257; 500 nM, LoKI-off, n=53, LoKI-on, n=60, *p=0.0102. (**C**) Quantification of total Plk1 immunofluorescence at each pole after 4 hr treatment with DMSO or CLP-BI2536; pole 2: DMSO, LoKI-off, n=52, LoKI-on, n=59, p=0.5380; 100 nM, LoKI-off, n=52, LoKI-on, n=58, p=0.9172; 250 nM, LoKI-off, n=55, LoKI-on, n=47, p=0.4275; 500 nM, LoKI-off, n=52, LoKI-on, n=52, p=0.8007. (**D**) Immunofluorescence of representative LoKI-off mitotic cells treated with DMSO (top) or 250 nM CLP-BI2536 (bottom) for 4 hr. Composite images (left) show α-tubulin (green), DAPI (blue), and γ-tubulin (magenta). Magnified grayscale images (right) show γ-tubulin signal at individual poles. (**E**) Quantification of amalgamated γ-tubulin immunofluorescence data. Data represented as box plots showing lowest/highest pole ratio for LoKI-off cells after 4 hr treatment with DMSO (white) or 250 nM CLP-BI2536 (gray). Mean values are indicated above each plot; DMSO, n=70, 250 nM, n=67, *p=0.0370. Values depicted in **B**, **C** and **E** represent individual cells (n). Data in **B** and **C** are normalized to pole 1. Experiments were conducted at least three times (N=3). P values were calculated by unpaired two-tailed Student's t-test. Data are mean ± s.e.m. NS, not significant.

Figure 5:

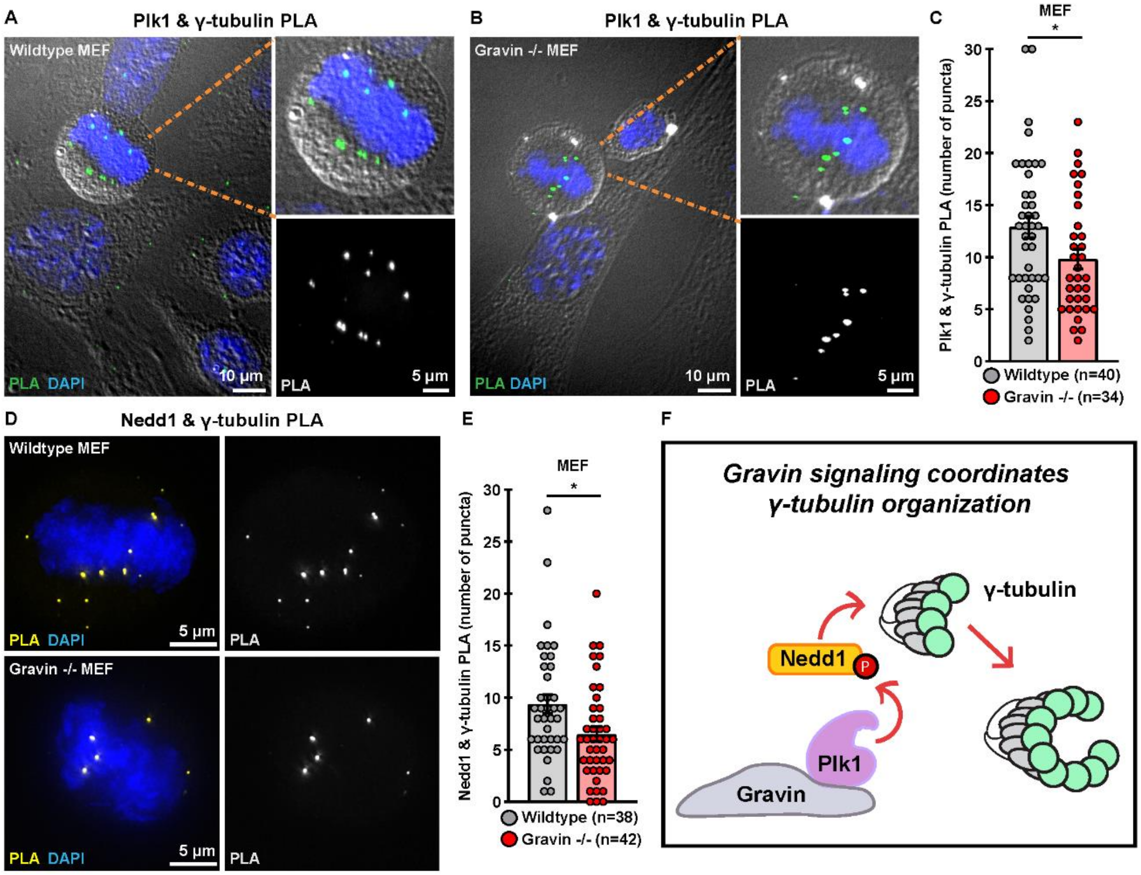

Figure 5 Legend: Interactions between γ-tubulin and upstream regulators are disrupted in Gravin-ablated cells. (**A, B**) Wildtype (**A**) and Gravin -/- (**B**) MEFs assayed with proximity ligation assay (PLA) reveal Plk1 & γ-tubulin interaction pairs. Composite images (left) show PLA puncta (green) and DAPI (blue). Differential interference contrast (DIC) shows cell boundaries in mitotic (foreground) and interphase (background) cells. Magnified insets of composite images (top right) depict a mitotic cell. Grayscale images (bottom right) reveal PLA puncta. (**C**) Quantification of Plk1 & γ-tubulin PLA (number of puncta per cell) in wildtype (gray) and Gravin -/- (red) MEFs; wildtype, n=40, Gravin -/-, n=34, *p=0.0357. (**D**) Immunofluorescence of wildtype (top) and Gravin -/- (bottom) MEFs assayed with PLA reveal Nedd1 & γ-tubulin interaction pairs. Composite images (left) show PLA (yellow) and DAPI (blue). Single channel images of PLA are represented in grayscale (right). (**E**) Quantification of Nedd1 & γ-tubulin PLA (number of puncta per cell) in wildtype (gray) and Gravin -/- (red) MEFs; wildtype, n=38, Gravin -/-, n=42, *p=0.0131. Points in **C** and **E** represent individual cells (n). Experiments were conducted three times (N=3). P values were calculated by unpaired two-tailed Student's t-test. Data are mean ± s.e.m. (**F**) Schematic depicting that Gravin organizes a signaling network which promotes accumulation of γ-tubulin (gray circles) when Plk1 and Nedd1 are in proximity to γ-tubulin.

CHAPTER 4: CONCLUSIONS AND FUTURE DIRECTIONS

4.1 LOCALIZED KINASE ACTIVITY UNDERLIES MITOTIC SIGNALING

While spatiotemporal regulation of signaling is now a recognized aspect of biology, we are only beginning to resolve how individual enzymes come together to drive complex biological events inside the cell. The challenge of studying local kinase action becomes particularly evident when we consider a process such as mitosis. Since the subcellular localizations and activities of protein kinases continuously change as a cell progresses through the mitotic cycle, ascribing unique functions to individual enzymes remains difficult. In this thesis, I attempt to tackle this problem and elucidate how two key mitotic kinases, Aurora A and Plk1 function during mitosis. While these enzymes share similar localization patterns and many overlapping roles, knowing their individual contributions is critical for understanding how cell division is regulated. Moreover, elucidating local kinase action can inform how Aurora A and Plk1 become dysregulated in disease and aid in the development of better anti-mitotic cancer therapeutics.

The studies in this thesis were borne from the observation that the A-kinase anchoring protein Gravin organizes centrosome-localized pools of Aurora A and Plk1 during mitosis. Based on previous findings from our lab, I hypothesized that activity of Aurora A and Plk1, specifically at mitotic centrosomes, is critical for ensuring the fidelity of various events during mitosis (Hehnly et al. 2015). Specifically, I set out to uncover how these Gravin-anchored pools of Aurora A and Plk1 facilitate and maintain mitotic signaling. While previous studies have utilized small-molecule inhibitor drugs to ascribed general functions to kinases during mitosis, this global drug distribution strategy could not resolve how Aurora A and Plk1 act at specific locations within the mitotic cell. In Chapter 2, I presented a new pharmacological tool, LoKI, which allowed me to achieve localized kinase inhibition and assign location-specific roles to these individual enzymes. Although this work provides new evidence for how Aurora A and Plk1 function within specific microenvironments, there is still much to learn about how this is played out in different cellular contexts. For example, utilizing LoKI to study how Aurora A and Plk1 activities are altered in diseased cells may inform future drug development. Additionally, implementing this system to study the local roles of other mitotic kinases can further elucidate how a specific signaling event is coordinated. Thus, generating new chemically-modified drugs that can be directed to LoKI platforms at centrosomes, kinetochores, and other mitotic structures can further decode how local kinase signaling events are regulated during cell division.

In conjunction with employing methods for localized kinase inhibition, further elucidating AKAP-mediated signaling events can provide information about how enzymes function at distinct subcellular locales. While our group previously showed that loss of Gravin promotes mitotic spindle abnormalities, mechanistic clues into how this occurs came with studies presented in Chapter 3 of this thesis. These experiments demonstrate that organization of a major microtubule nucleating protein, γ-tubulin, is disrupted in Gravin-depleted cells. My initial studies explore how Gravin organizes γ-tubulin in mouse embryonic fibroblasts; however, a major advance in this work came with the generation of CRISPR-Cas9 genome-edited U2OS cells. While previous findings in human cells have utilized shRNA-mediated knockdown to deplete Gravin, to my knowledge this is the first human cell line in which the Gravin gene has been completely disrupted. However, removing a scaffold protein to ascertain the roles of binding partners in specific cellular processes poses several challenges. For example, it becomes difficult to determine whether a particular phenotype is due to a disrupted protein-protein interactions, aberrant protein localization, or loss of kinase activity. Studies in Chapter 3 reveal that interaction between Plk1 and Nedd1, a Plk1 substrate and regulator of microtubule nucleation, is disrupted in Gravin null cells. Thus, it is possible that the γ-tubulin accumulation defects observed in cells lacking Gravin are because other components of the microtubule nucleating complex are disrupted. Using LoKI, I also demonstrate that inhibition of Plk1 activity at mitotic centrosomes in wildtype U2OS cells recapitulates the defects that I observe in cells lacking Gravin. However, since both Plk1 activity and protein-protein interactions between Plk1 and downstream substrates are disrupted in

Gravin-depleted cells, the exact molecular mechanism that governs this process may be more complex. It is quite possible that yet unknown Gravin binding partners may also play a role. In fact, GCP3, a component of the gamma-tubulin ring complex, was recently identified in a screen as a potential Gravin interacting protein (Fogeron et al. 2013). However, this interaction has not yet been validated. Additional studies are required to clarify whether GCP3 binds Gravin, whether localization of this protein is disrupted in Gravin null cells, and whether the functional consequence of disrupting a GCP3-Gravin interaction is, in fact, failed accumulation of γ-tubulin at mitotic spindle defects. Moreover, future work will likely uncover additional downstream substrates that are regulated by Gravin-anchored enzymes and provide greater insight into how mitotic signaling events are coordinated at specific subcellular locations. Nonetheless, the work presented in this thesis introduces a new pharmacology tool for localized kinase inhibition, ascribes location-specific functions to the mitotic kinases, Aurora A and Plk1, and uncovers new Gravin-mediated signaling events during mitosis.

4.2 THE FUTURE OF LOCALIZED KINASE BIOLOGY

Studying signaling complexes at molecular scaffolds such as AKAPs and designing pharmacological tools to achieve localized kinase inhibition are complementary methods for elucidating local kinase action. I envision that in the future these approaches can be combined to achieve even greater insight into how enzymes function in space and time. One way to do this is to use CRISPR/Cas9 genome-editing to generate LoKI platform “knock-ins”. In “knock-in” cells, AKAP-LoKI fusions would be expressed from the endogenous genetic locus negating the need for transient or viral expression vectors to be introduced. By using a cell’s endogenous promoter, expression of the LoKI platform would permit subcellular drug targeting without resulting in overexpression of the protein that is used for platform localization. In Chapter 2, I used a PACT domain, instead of Gravin, to direct Aurora A and Plk1 kinase inhibitors to centrosomes. While this allowed me to keep the Gravin complex intact, it is worth noting that overexpression of PACT is sufficient to displace other proteins at the centrosomes (Gillingham and Munro 2000). Even though extensive validation and control experiments were conducted to allow for correct interpretation of the data, it would be beneficial to utilize a modified approach that avoids this issue entirely. However, it is also worth considering that creating “knock-in” cells in which the AKAP is artificially fused to bulky LoKI platform may still disrupt correct assembly of AKAP complexes. Regardless, in a properly validated “knock-in” line, the ability to achieve localized kinase inhibition could inform how enzymes normally function within macromolecular complexes at defined subcellular locations.

Another future avenue for the study of local kinase biology could involve exploiting multiple chemical-genetic tools in combination to better probe subcellular signaling events. For example, expressing an analog-sensitive Plk1 at a distinct microenvironment and directing LoKI platforms to that location could reduce off-target effects that may occur as the CLP-modified drug distributes throughout the cell prior to being sequestered at the desired location. Moreover, future studies utilizing this combination approach could validate previous work that ascribed unique roles for Plk1 within distinct regions of the kinetochore, including the outer kinetochore, chromatin, and the inner centromere (Lera et al. 2016). Similarly, implementing LoKI platforms in cells that express drug-resistant kinases could further decouple the activity-specific and location-specific roles of individual kinases. Undoubtedly, utilizing multiple chemical-genetic methods to explore the local contributions of unique signaling enzymes will further elucidate local kinase action.

While the focus of this thesis was to decipher local actions of Aurora A and Plk1, I envision that future applications of this tool would include targeting additional kinases to study local signaling events in other processes. For example, the LoKI strategy could go beyond examining the spatiotemporal regulation of mitosis and be used to decipher the local signaling profiles of kinases that regulate cell motility or metabolism. In a broader sense, local drug targeting can help investigators address questions that have been difficult to answer with traditional drug delivery methods. By exploiting our knowledge of AKAP-mediated signaling events and implementing LoKI targeted drug delivery, we now have strategy for studying local kinase action at a resolution that was not possible before. Ultimately, by piecing together how individual enzymes drive a signaling event at a specific subcellular location, we will gain important mechanistic clues into the regulation of complex biological phenomena.

APPENDIX

Chapter 2 Key Resources Table				
Reagent type (species) or resource	**Designation**	**Source or reference**	**Identifiers**	**Additional information**
Antibody	Alpha-tubulin, clone DM1A	Sigma Aldrich	T9026 Mouse monoclonal RRID: AB_477593	IF (1:500)
Antibody	Alpha-tubulin-FITC, clone DM1A	Sigma Aldrich	F2168 Mouse monoclonal RRID: AB_477593	IF (1:200)
Antibody	Amersham ECL Mouse IgG, HRP-linked F(ab')$_2$ fragment (from sheep)	GE Life Sciences	NA9310	WB (1:10000)
Antibody	Amersham ECL Rabbit IgG, HRP-linked F(ab')$_2$ fragment (from donkey)	GE Life Sciences	NA9340	WB (1:10000)
Antibody	Aurora A	Sigma Aldrich	SAB2500135 Goat polyclonal	WB (1:1000)
Antibody	Centromere (ACA)	Antibodies Inc.	15-234-0001 Human polyclonal	IF (1:200)
Antibody	Phospho-Aurora A (T288), clone C39D8	Cell Signaling	3079 Rabbit polyclonal	IF (1:500); WB (1:1000)
Antibody	Donkey anti-goat IgG-HRP	Santa Cruz	sc-2020	WB (1:10000)

Antibody	Donkey anti-Mouse IgG, Alexa Fluor 488	Invitrogen	A-21202	IF (1:500)
Antibody	Donkey anti-Mouse IgG, Alexa Fluor 555	Invitrogen	A-31570	IF (1:500)
Antibody	Donkey anti-Mouse IgG, Alexa Fluor 647	Invitrogen	A-11126	IF (1:500)
Antibody	Donkey anti-Rabbit IgG, Alexa Fluor 488	Invitrogen	A-21206	IF (1:500)
Antibody	Donkey anti-Rabbit IgG, Alexa Fluor 555	Invitrogen	A-31572	IF (1:500)
Antibody	Donkey anti-Rabbit IgG, Alexa Fluor 647	Invitrogen	A-31573	IF (1:500)
Antibody	DyLight™ 405 AffiniPure Donkey Anti-Human IgG (H+L)	Jackson Labs	RRID: AB_2340553	IF (1:500)
Antibody	GAPDH-HRP	Novus	NB110-40405 Mouse monoclonal RRID: AB_669249	WB (1:2000)
Antibody	Gamma-tubulin	Abcam	11317 Rabbit polyclonal	IF (1:1500)
Antibody	Gravin, clone JP74	Sigma Aldrich	G3795 Mouse monoclonal	WB (1:1000)
Antibody	Gravin, clone R3698	(Nauert et al. 1997)	Rabbit polyclonal	IF (1:1000)
Antibody	Phospho-Gravin (T766)	(Canton et al. 2012; Hehnly et al. 2015;	Rabbit polyclonal	IF (1:1000)

		Colicinio et al. 2018)		
Antibody	Phospho-Hec1 (S69)	(Deluca et al. 2018)	Rabbit polyclonal	IF (1:3000) WB (1:3000)
Antibody	Phospho-Plk1 (T210)	Biolegend	628901 Rabbit polycolonal RRID: AB_439786	IF (1:500); WB (1:1000)
Antibody	Plk1, clone 35-206	Millipore	05-844 Mouse monoclonal RRID: AB_11213632	IF (1:500); WB (1:1000)
Antibody	SNAP-tag	New England Biolabs	P9310S Rabbit polyclonal	WB (1:1000)
Cell line (*H. sapein*)	HEK293 Control shRNA stable cell line	(Canton et al. 2012; Hehnly et al. 2015; Colicinio et al. 2018)		Maintained in Scott lab in DMEM supplemented with 10% FBS under 4 ug/mL Puromycin selection
Cell line (*H. sapein*)	HEK293 Gravin shRNA stable cell line	(Canton et al. 2012; Hehnly et al. 2015; Colicinio et al. 2018)		Maintained in Scott lab in DMEM supplemented with 10% FBS under under 4 ug/mL Puromycin selection
Cell line (*H. sapein*)	HeLa	From L. Wordeman lab, origin ATCC		Maintained in the Scott Lab in DMEM supplemented with 10% FBS
Cell line (*H. sapein*)	hTERT-RPE	Gift from P. Jallepalli lab, origin ATCC		Maintained in the Scott Lab in DMEM/F-12,

				Hepes with 10% FBS
Cell line (*M. musculus)*	MEF Gravin wildtype	(Hehnly et al. 2015)		
Cell line (*M. musculus)*	MEF Gravin knockout	(Hehnly et al. 2015)		
Cell line (*H. sapein*)	U2OS	ATCC	HTB-96	Maintained in the Scott Lab in DMEM supplemented with 10% FBS
Chemical compound, drug	Alisertib, MLN8237	AdooQ	A10004-10nM-D	Manufacturer's instructions
Chemical compound, drug	BI2536	AdooQ	A10134-50	Manufacturer's instructions
Chemical compound, drug	Beta-mercaptoethanol (BME)	Sigma Aldrich	M6250	
Chemical compound, drug	CLP-BI2536	This paper		See "synthesis of CLP-reagents"
Chemical compound, drug	CLP-MLN8237	This paper		See "synthesis of CLP-reagents"
Chemical compound, drug	CLP-rhodamine	This paper		See "synthesis of CLP-reagents"
Chemical compound, drug	DAPI	Thermo Fisher	62248	IF (1:1000)
Chemical compound, drug	Dimethylsulfoxide (DMSO)	Pierce	TS-20688	Manufacturer's instructions
Chemical compound, drug	DMEM FluoroBrite™	Life Technologies	A1896701	
Chemical compound, drug	DMEM/F-12 Hepes	Life Technologies	11330057	

Chemical compound, drug	DMEM, high glucose	Life Technologies	11965118	
Chemical compound, drug	Doxycycline hyclate	Sigma Aldrich	24390-14-5	
Chemical compound, drug	Fetal Bovine Serum	Thermo Fisher	A3382001	
Chemical compound, drug	Lipofectamine 2000 Transfection Reagent	Invitrogen	11668027	
Chemical compound, drug	NuPAGE™ LDS Sample Buffer 4X	Thermo Fisher	NP0008	
Chemical compound, drug	Opti-MEM® I Reduced Serum Medium, no phenol red	Life Technologies	11058021	
Chemical compound, drug	ProLong® Diamond Antifade Mountant	Life Technologies	P36961	Manufacturer’s instructions
Chemical compound, drug	Polybrene	Santa Cruz	134220	Manufacturer’s instructions
Chemical compound, drug	Puromycin dihydrochloride	Santa Cruz	58-58-2	4 ug/mL
Chemical compound, drug	SNAP-Cell® Fluorescein	New England Biolabs	S9107S	Manufacturer’s instructions
Chemical compound, drug	SNAP-Cell® 647-SiR	New England Biolabs	S9102S	Manufacturer’s instructions
Chemical compound, drug	SuperSignal™ West Dura Extended Duration Substrate	Thermo Fisher	34075	
Chemical compound, drug	TransIT®-LT1 Transfection Reagent	Mirus	MIR2300	
Chemical compound, drug	Trypsin-EDTA (0.25%), phenol red	Gibco	25200056	

Commercial assay or kit	BCA Protein Assay Kit	Thermo Fisher	23227	
Commercial assay or kit	QuikChange II XL kit	Aligent	200522	
Commercial assay or kit	GeneJET Genomic DNA purification kit	Thermo Fisher	K0721	
Peptide, recombinant protein	Aurora A, active	Invitrogen	PV3612	
Peptide, recombinant protein	Plk1, active	SignalChem	P41-10H	
Recombinant DNA reagent	EMTB-3XGFP	Addgene		pCS2+ backbone
Recombinant DNA reagent	GFP-H2B	Addgene		pEGFP-N1 backbone
Recombinant DNA reagent	His6-SNAP-tag	Addgene		pMCSG7 backbone
Recombinant DNA reagent	pMD2.G		RRID: Addgene_12259	gift from Didier Trono; Addgene plasmid #12259
Recombinant DNA reagent	psPAX2		RRID: Addgene_12260	gift from Didier Trono; Addgene plasmid #12259
Recombinant DNA reagent	SNAP-PACT	This paper		In-house modified pLIX402 backbone (gift from David Root; Addgene plasmid #41394)
Recombinant DNA reagent	SNAP-PACT (C144A)	This paper		In-house modified pLIX402

				backbone (gift from David Root; Addgene plasmid #41394)
Recombinant DNA reagent	SNAP-Mis12	This paper		In-house modified pLIX402 backbone (gift from David Root; Addgene plasmid #41394)
Recombinant DNA reagent	SNAP-Mis12 (C144A)	This paper		In-house modified pLIX402 backbone (gift from David Root; Addgene plasmid #41394)
Recombinant DNA reagent	SNAP-AKAP79	This paper		In-house modified pcDNA3.1+ backbone (Life Technologies)
Recombinant DNA reagent	SNAP-dAKAP1	This paper		In-house modified pcDNA3.1+ backbone (Life Technologies)
Software, algorithm	Fiji/ImageJ	ImageJ (http://imagej.nih.gov/ij/)		
Software, algorithm	GraphPad Prism	GraphPad Prism (https://graphpad.com)		
Software, algorithm	Imaris	Bitplane		
Software, algorithm	SoftWoRx	GE Healthcare		

Other	1.5 poly-D-lysine coated coverslips	neuVitro	GG-12-1.5-pdl	
Other	AnykD™ Criterion™ TGX™ Precast Midi Protein Gel	Biorad	5671124	
Other	Bolt® 4-12% Bis-Tris Plus Gels	Invitrogen	NW04120BOX	
Other	Scienceware cloning discs	Sigma Aldrich	Z374431	
Other	µ-Slide 4 Well Glass Bottom: # 1.5H (170 µm +/- 5 µm) D 263 M Schott glass	(Ibidi)Pierce ™	80426	

Chapter 3 Key Resources Table				
Reagent type (species) or resource	**Designation**	**Source or reference**	**Identifiers**	**Additional information**
Antibody	Alpha-tubulin, clone DM1A	Sigma Aldrich	T9026 Mouse monoclonal RRID: AB_477593	IF (1:500)
Antibody	Alpha-tubulin-FITC, clone DM1A	Sigma Aldrich	F2168 Mouse monoclonal RRID: AB_477593	IF (1:200)
Antibody	Amersham ECL Mouse IgG, HRP-linked F(ab')$_2$ fragment (from sheep)	GE Life Sciences	NA9310	WB (1:10000)
Antibody	Amersham ECL Rabbit IgG, HRP-linked F(ab')$_2$ fragment (from donkey)	GE Life Sciences	NA9340	WB (1:10000)
Antibody	Donkey anti-Mouse IgG, Alexa Fluor 488	Invitrogen	A-21202	IF (1:500)
Antibody	Donkey anti-Rabbit IgG, Alexa Fluor 647	Invitrogen	A-31573	IF (1:500)
Antibody	Gamma-tubulin	Abcam	11317 Rabbit polyclonal RRID: AB_297921	IF (1:1500) PLA (1:500) WB (1:1000)
Antibody	GAPDH-HRP	Novus	NB110-40405 Mouse monoclonal RRID: AB_669249	WB (1:2000)

Antibody	Gravin, clone JP74	Sigma Aldrich	G3795 Mouse monoclonal	WB (1:1000)
Antibody	Gravin, clone R3698	(Nauert et al. 1997)	Rabbit polyclonal	WB (1:1000)
Antibody	Nedd1, clone H-3	Santa Cruz Biotechnology	sc-398733 Mouse monoclonal	PLA (1:100)
Antibody	Phospho-Plk1 (T210)	Biolegend	628901 Rabbit polycolonal RRID: AB_439786	IF (1:500)
Antibody	Plk1, clone 35-206	Millipore	05-844 Mouse monoclonal RRID: AB_11213632	WB (1:1000)
Antibody	Plk1, clone F-8	Santa Cruz Biotechnology	sc-17783 Mouse monoclonal RRID: AB_628157	PLA (1:100)
Cell line (*H. sapein*)	HEK293 Control shRNA stable cell line	(Canton et al. 2012)		Maintained in Scott lab in DMEM supplemented with 10% FBS under 4 ug/mL Puromycin selection
Cell line (*H. sapein*)	HEK293 Gravin shRNA stable cell line	(Canton et al. 2012)		Maintained in Scott lab in DMEM supplemented with 10% FBS under under 4 ug/mL Puromycin selection

Cell line (*H. sapein*)	HeLa Control shRNA stable cell line	(Hehnly et al. 2015)		Maintained in Scott lab in DMEM supplemented with 10% FBS under 4 ug/mL Puromycin selection
Cell line (*H. sapein*)	HeLa Gravin shRNA stable cell line	(Hehnly et al. 2015)		Maintained in Scott lab in DMEM supplemented with 10% FBS under 4 ug/mL Puromycin selection
Cell line (*H. sapein*)	U2OS	ATCC	HTB-96	Maintained in the Scott Lab in DMEM supplemented with 10% FBS
Cell line (*H. sapein*)	U2OS LoKI-off	(Bucko et al. 2019)		Maintained in the Scott Lab in DMEM supplemented with 10% FBS under 4 ug/mL Puromycin selection
Cell line (*H. sapein*)	U2OS LoKI-on	(Bucko et al. 2019)		Maintained in the Scott Lab in DMEM supplemented with 10% FBS under 4 ug/mL Puromycin selection
Cell line (*M. musculus)*	MEF Gravin wildtype	(Hehnly et al. 2015)		
Cell line (*M. musculus)*	MEF Gravin -/-	(Hehnly et al. 2015)		

Chemical compound, drug	BI2536	AdooQ	A10134-50	Manufacturer’s instructions
Chemical compound, drug	Beta-mercaptoethanol (BME)	Sigma Aldrich	M6250	
Chemical compound, drug	CLP-BI2536	(Bucko et al. 2019)		
Chemical compound, drug	DAPI	Thermo Fisher	62248	IF (1:1000)
Chemical compound, drug	Dimethylsulfoxide (DMSO)	Pierce	TS-20688	Manufacturer’s instructions
Chemical compound, drug	DMEM, high glucose	Life Technologies	11965118	
Chemical compound, drug	Doxycycline hyclate	Sigma Aldrich	24390-14-5	
Chemical compound, drug	Fetal Bovine Serum	Thermo Fisher	A3382001	
Chemical compound, drug	Lipofectamine 2000 Transfection Reagent	Invitrogen	11668027	
Chemical compound, drug	NuPAGE™ LDS Sample Buffer 4X	Thermo Fisher	NP0008	
Chemical compound, drug	Opti-MEM® I Reduced Serum Medium, no phenol red	Life Technologies	11058021	
Chemical compound, drug	ProLong® Diamond Antifade Mountant	Life Technologies	P36961	Manufacturer’s instructions

Chemical compound, drug	Polybrene	Santa Cruz	134220	Manufacturer's instructions
Chemical compound, drug	Puromycin dihydrochloride	Santa Cruz	58-58-2	4 ug/mL
Chemical compound, drug	SuperSignal™ West Pico PLUS Chemiluminescent Substrate	Thermo Fisher	34579	
Chemical compound, drug	TransIT®-LT1 Transfection Reagent	Mirus	MIR2300	
Chemical compound, drug	Trypsin-EDTA (0.25%), phenol red	Gibco	25200056	
Commercial assay or kit	BCA Protein Assay Kit	Thermo Fisher	23227	
Commercial assay or kit	Duolink® In Situ Detection Reagents Green	Sigma Aldrich	DUO92014	
Commercial assay or kit	Duolink® In Situ PLA® Probe Anti-Mouse MINUS	Sigma Aldrich	DUO92004	
Commercial assay or kit	Duolink® In Situ PLA® Probe Anti-Rabbit PLUS	Sigma Aldrich	DUO92002	
Commercial assay or kit	GeneJET Genomic DNA purification kit	Thermo Fisher	K0721	
Commercial assay or kit	QuikChange II XL kit	Aligent	200522	
Recombinant DNA reagent	pSpCas9(BB)-GravinKO1-2A-Puro (PX459)	This paper	RRID: Addgene_48139	PX459 backbone; U6-sgRNA cassette: AGAGATGGCTACTAAGTCAG

Recombinant DNA reagent	pSpCas9(BB)-GravinKO2-2A-Puro (PX459)	This paper	RRID: Addgene_48139	PX459 backbone; U6-sgRNA cassette: AGCCGAATCTGGCCAAGCAG
Recombinant DNA reagent	pMD2.G	Bucko et al. 2019	RRID: Addgene_12259	gift from Didier Trono; Addgene plasmid #12259
Recombinant DNA reagent	psPAX2	Bucko et al. 2019	RRID: Addgene_12260	gift from Didier Trono; Addgene plasmid #12259
Recombinant DNA reagent	SNAP-PACT-pLIX402	Bucko et al. 2019		In-house modified pLIX402 backbone (gift from David Root; Addgene plasmid #41394)
Recombinant DNA reagent	SNAP-PACT-pLIX402 (C144A)	Bucko et al. 2019		In-house modified pLIX402 backbone (gift from David Root; Addgene plasmid #41394)
Sequenced-based reagent	gRNA1-forward	This paper	PCR primers	TTGGACAGAGAGACTCTGAAGATGTG
Sequenced-based reagent	gRNA1-reverse	This paper	PCR primers	CTTCATCTTTCTTCACAGTGAGTAGC
Sequenced-based reagent	gRNA2-forward	This paper	PCR primers	ACTGTGAAGAAAGATGAAGGGG
Sequenced-based reagent	gRNA2-reverse	This paper	PCR primers	TTGATCCTGTTTCACTGGTCAC

Software, algorithm	Fiji/ImageJ	ImageJ (http://imagej.nih.gov/ij/)		
Software, algorithm	GraphPad Prism	GraphPad Prism (https://graphpad.com)		
Software, algorithm	SoftWoRx	GE Healthcare		
Other	1.5 poly-D-lysine coated coverslips	neuVitro	GG-12-1.5-pdl	
Other	Bolt® 4-12% Bis-Tris Plus Gels	Invitrogen	NW04120BOX	
Other	Scienceware cloning discs	Sigma Aldrich	Z374431	

Chapter 3 Statistical Analyses Table

Figure	Condition	Sample size (n)	Test	Statistics	p-value	Summary
1H	Wildtype	49	unpaired two-tailed Student's t-test	t=5.855, df=101	<0.0001	****
	Gravin -/-	54				
S1C	Control shRNA	46	unpaired two-tailed Student's t-test	t=3.901, df=90	0.0002	***
	Gravin shRNA	46				
2G	Wildtype	3	unpaired two-tailed Student's t-test	t=8.527, df=4	0.0010	**
	Gravin KO	3				
S2B	Control shRNA	3	unpaired two-tailed Student's t-test	t=5.340, df=4	0.0059	**
	Gravin shRNA	3				
S2C	Wildtype	2	unpaired two-tailed Student's t-test	t=26.90, df=2	0.0014	**
	Gravin KO	2				
3D	Pole 1	64	unpaired two-tailed Student's t-test	t=3.794, df=126	0.0002	***
	Pole2	64				
3E	Pole 1	23	unpaired two-tailed Student's t-test	t=2.454, df=44	0.0181	*
	Pole2	23				
3J	WT	49	unpaired two-tailed Student's t-test	t=2.042, df=100	0.0438	*
	-/-	53				
3K	WT	23	unpaired two-tailed Student's t-test	t=2.303, df=42	0.0263	*
	KO	21				
4C	DMSO (pole 2)	53	one-way ANOVA with Dunnett's multiple comparisons test	F (4, 224)=11.47	control	-
	5 nM (pole 2)	44			0.1387	NS
	10 nM (pole 2)	44			0.7016	NS
	15 nM (pole 2)	44			<0.0001	****
	20 nM (pole 2)	44			<0.0001	****

4F	LoKI-off, pole 1	49	unpaired two-tailed Student's t-test	t=4.770, df=96	<0.0001	****
	LoKI-off, pole 2	49				
4F	LoKI-on, pole 1	49	unpaired two-tailed Student's t-test	t=5.362, df=96	<0.0001	****
	LoKI-on, pole 2	49				
4F	LoKI-off, pole 2	49	unpaired two-tailed Student's t-test	t=3.382, df=96	0.0010	**
	LoKI-on, pole 2	49				
4H	DMSO	76	unpaired two-tailed Student's t-test	t=2.716, df=148	0.0074	**
	250 nM	74				
S4B	DMSO, LoKI-off (pole 2)	44	unpaired two-tailed Student's t-test	t=1.163, df=102	0.2477	NS
	DMSO, LoKI-on (pole 2)	60				
S4B	100 nM, LoKI-off (pole 2)	46	unpaired two-tailed Student's t-test	t=0.09352, df=103	0.9257	NS
	100 nM, LoKI-on (pole 2)	59				
S4B	500 nM, LoKI-off (pole 2)	53	unpaired two-tailed Student's t-test	t=2.612, df=111	0.0102	*
	500 nM, LoKI-on (pole 2)	60				
S4C	DMSO, LoKI-off (pole 2)	52	unpaired two-tailed Student's t-test	t=0.6178, df=109	0.5380	NS
	DMSO, LoKI-on (pole 2)	59				
S4C	100 nM, LoKI-off (pole 2)	52	unpaired two-tailed Student's t-test	t=0.1043, df=108	0.9172	NS
	100 nM, LoKI-on (pole 2)	58				
S4C	250 nM, LoKI-off (pole 2)	55	unpaired two-tailed Student's t-test	t=0.7968, df=100	0.4275	NS
	250 nM, LoKI-on (pole 2)	47				
S4C	500 nM, LoKI-off (pole 2)	52	unpaired two-tailed Student's t-test	t=0.2530, df=102	0.8007	NS
	500 nM, LoKI-on (pole 2)	52				
S4E	DMSO	70	unpaired two-tailed Student's t-test	t=2.106, df=135	0.0370	*
	250 nM	67				
5C	Wildtype	40		t=2.140, df=72	0.0357	*

	Gravin -/-	34	unpaired two-tailed Student's t-test			
5E	Wildtype	38	unpaired two-tailed Student's t-test	t=2.538, df=78	0.0131	*
	Gravin -/-	42				

REFERENCES

Akakura, S., P. Nochajski, L. Gao, P. Sotomayor, S. Matsui, and I. H. Gelman. 2010. 'Rb-dependent cellular senescence, multinucleation and susceptibility to oncogenic transformation through PKC scaffolding by SSeCKS/AKAP12', *Cell Cycle*, 9: 4656-65.

Alvarado-Kristensson, M., M. J. Rodriguez, V. Silio, J. M. Valpuesta, and A. C. Carrera. 2009. 'SADB phosphorylation of gamma-tubulin regulates centrosome duplication', *Nat Cell Biol*, 11: 1081-92.

Asteriti, I. A., F. De Mattia, and G. Guarguaglini. 2015. 'Cross-Talk between AURKA and Plk1 in Mitotic Entry and Spindle Assembly', *Front Oncol*, 5: 283.

Asteriti, I. A., E. Di Cesare, F. De Mattia, V. Hilsenstein, B. Neumann, E. Cundari, P. Lavia, and G. Guarguaglini. 2014. 'The Aurora-A inhibitor MLN8237 affects multiple mitotic processes and induces dose-dependent mitotic abnormalities and aneuploidy', *Oncotarget*, 5: 6229-42.

Barr, F. A., H. H. Sillje, and E. A. Nigg. 2004. 'Polo-like kinases and the orchestration of cell division', *Nat Rev Mol Cell Biol*, 5: 429-40.

Bateman, N. W., E. Jaworski, W. Ao, G. Wang, T. Litzi, E. Dubil, C. Marcus, K. A. Conrads, P. N. Teng, B. L. Hood, N. T. Phippen, L. A. Vasicek, W. P. McGuire, K. Paz, D. Sidransky, C. A. Hamilton, G. L. Maxwell, K. M. Darcy, and T. P. Conrads. 2015. 'Elevated AKAP12 in paclitaxel-resistant serous ovarian cancer cells is prognostic and predictive of poor survival in patients', *J Proteome Res*, 14: 1900-10.

Bishop, A., O. Buzko, S. Heyeck-Dumas, I. Jung, B. Kraybill, Y. Liu, K. Shah, S. Ulrich, L. Witucki, F. Yang, C. Zhang, and K. M. Shokat. 2000. 'Unnatural ligands for engineered proteins: new tools for chemical genetics', *Annu Rev Biophys Biomol Struct*, 29: 577-606.

Bruinsma, W., M. Aprelia, J. Kool, L. Macurek, A. Lindqvist, and R. H. Medema. 2015. 'Spatial Separation of Plk1 Phosphorylation and Activity', *Front Oncol*, 5: 132.

Bucko, P. J., C. K. Lombard, L. Rathbun, I. Garcia, A. Bhat, L. Wordeman, F. D. Smith, D. J. Maly, H. Hehnly, and J. D. Scott. 2019. 'Subcellular drug targeting illuminates local kinase action', *Elife*, 8.

Bucko, P.J., and J.D. Scott. 2021. 'Drugs that regulate local cell signaling: AKAP targeting as a therapeutic option', *Annu Rev Pharmacol Toxicol*, 61: 2.1-2.19.

Calejo, A. I., and K. Tasken. 2015. 'Targeting protein-protein interactions in complexes organized by A kinase anchoring proteins', *Front Pharmacol*, 6: 192.

Canton, D. A., C. D. Keene, K. Swinney, L. K. Langeberg, V. Nguyen, L. Pelletier, T. Pawson, L. Wordeman, N. Stella, and J. D. Scott. 2012. 'Gravin is a transitory effector of polo-like kinase 1 during cell division', *Mol Cell*, 48: 547-59.

Canton, D. A., and J. D. Scott. 2013. 'Anchoring proteins encounter mitotic kinases', *Cell Cycle*, 12: 863-4.

Caracciolo, V., L. D'Agostino, E. Draberova, V. Sladkova, C. Crozier-Fitzgerald, D. P. Agamanolis, J. P. de Chadarevian, A. Legido, A. Giordano, P. Draber, and C. D. Katsetos. 2010. 'Differential expression and cellular distribution of gamma-tubulin and betaIII-tubulin in medulloblastomas and human medulloblastoma cell lines', *J Cell Physiol*, 223: 519-29.

Carr, D. W., Z. E. Hausken, I. D. Fraser, R. E. Stofko-Hahn, and J. D. Scott. 1992. 'Association of the type II cAMP-dependent protein kinase with a human thyroid RII-anchoring protein. Cloning and characterization of the RII-binding domain', *J Biol Chem*, 267: 13376-82.

Carr, D. W., and J. D. Scott. 1992. 'Blotting and band-shifting: techniques for studying protein-protein interactions', *Trends Biochem Sci*, 17: 246-9.

Carr, D. W., R. E. Stofko-Hahn, I. D. Fraser, S. M. Bishop, T. S. Acott, R. G. Brennan, and J. D. Scott. 1991. 'Interaction of the regulatory subunit (RII) of cAMP-dependent protein kinase with RII-anchoring proteins occurs through an amphipathic helix binding motif', *J Biol Chem*, 266: 14188-92.

Caunt, C. J., M. J. Sale, P. D. Smith, and S. J. Cook. 2015. 'MEK1 and MEK2 inhibitors and cancer therapy: the long and winding road', *Nat Rev Cancer*, 15: 577-92.

Chen, D., A. Purohit, E. Halilovic, S. J. Doxsey, and A. C. Newton. 2004. 'Centrosomal anchoring of protein kinase C betaII by pericentrin controls microtubule organization, spindle function, and cytokinesis', *J Biol Chem*, 279: 4829-39.

Cheng, C. Y., C. J. Liu, Y. C. Huang, S. H. Wu, H. W. Fang, and Y. J. Chen. 2018. 'BI2536 induces mitotic catastrophe and radiosensitization in human oral cancer cells', *Oncotarget*, 9: 21231-43.

Chinen, T., P. Liu, S. Shioda, J. Pagel, B. Cerikan, T. C. Lin, O. Gruss, Y. Hayashi, H. Takeno, T. Shima, Y. Okada, I. Hayakawa, Y. Hayashi, H. Kigoshi, T. Usui, and E. Schiebel. 2015. 'The gamma-tubulin-specific inhibitor gatastatin reveals temporal requirements of microtubule nucleation during the cell cycle', *Nat Commun*, 6: 8722.

Chmatal, L., K. Yang, R. M. Schultz, and M. A. Lampson. 2015. 'Spatial Regulation of Kinetochore Microtubule Attachments by Destabilization at Spindle Poles in Meiosis I', *Curr Biol*, 25: 1835-41.

Cho, E. H., R. A. Whipple, M. A. Matrone, E. M. Balzer, and S. S. Martin. 2010. 'Delocalization of gamma-tubulin due to increased solubility in human breast cancer cell lines', *Cancer Biol Ther*, 9: 66-76.

Choi, M., W. Kim, M. G. Cheon, C. W. Lee, and J. E. Kim. 2015. 'Polo-like kinase 1 inhibitor BI2536 causes mitotic catastrophe following activation of the spindle assembly checkpoint in non-small cell lung cancer cells', *Cancer Lett*, 357: 591-601.

Cirak, Y., Y. Furuncuoglu, O. Yapicier, A. Aksu, and E. Cubukcu. 2015. 'Aurora A overexpression in breast cancer patients induces taxane resistance and results in worse prognosis', *J BUON*, 20: 1414-9.

Colicino, E. G., A. M. Garrastegui, J. Freshour, P. Santra, D. E. Post, L. Kotula, and H. Hehnly. 2018. 'Gravin regulates centrosome function through PLK1', *Mol Biol Cell*, 29: 532-41.

Combes, G., I. Alharbi, L. G. Braga, and S. Elowe. 2017. 'Playing polo during mitosis: PLK1 takes the lead', *Oncogene*, 36: 4819-27.

Corbin, J. D., S. L. Keely, and C. R. Park. 1975. 'The distribution and dissociation of cyclic adenosine 3':5'-monophosphate-dependent protein kinases in adipose, cardiac, and other tissues', *J Biol Chem*, 250: 218-25.

Cowley, D. O., J. A. Rivera-Perez, M. Schliekelman, Y. J. He, T. G. Oliver, L. Lu, R. O'Quinn, E. D. Salmon, T. Magnuson, and T. Van Dyke. 2009. 'Aurora-A kinase is essential for bipolar spindle formation and early development', *Mol Cell Biol*, 29: 1059-71.

Deak, V. A., and E. Klussmann. 2016. 'Pharmacological Interference With Protein-protein Interactions of Akinase Anchoring Proteins as a Strategy for the Treatment of Disease', *Curr Drug Targets*, 17: 1147-71.

DeLuca, J. G. 2017. 'Aurora A Kinase Function at Kinetochores', *Cold Spring Harb Symp Quant Biol*, 82: 91-99.

DeLuca, K. F., A. Meppelink, A. J. Broad, J. E. Mick, O. B. Peersen, S. Pektas, S. M. A. Lens, and J. G. DeLuca. 2018. 'Aurora A kinase phosphorylates Hec1 to regulate metaphase kinetochore-microtubule dynamics', *J Cell Biol*, 217: 163-77.

Dessauer, C. W. 2009. 'Adenylyl cyclase--A-kinase anchoring protein complexes: the next dimension in cAMP signaling', *Mol Pharmacol*, 76: 935-41.

Diviani, D., L. K. Langeberg, S. J. Doxsey, and J. D. Scott. 2000. 'Pericentrin anchors protein kinase A at the centrosome through a newly identified RII-binding domain', *Curr Biol*, 10: 417-20.

Dukic, A. R., L. H. Haugen, G. Pidoux, E. Leithe, O. Bakke, and K. Tasken. 2017. 'A protein kinase A-ezrin complex regulates connexin 43 gap junction communication in liver epithelial cells', *Cell Signal*, 32: 1-11.

Elia, A. E., L. C. Cantley, and M. B. Yaffe. 2003. 'Proteomic screen finds pSer/pThr-binding domain localizing Plk1 to mitotic substrates', *Science*, 299: 1228-31.

Ellis-Davies, G. C. 2007. 'Caged compounds: photorelease technology for control of cellular chemistry and physiology', *Nat Methods*, 4: 619-28.

Esseltine, J. L., and J. D. Scott. 2013. 'AKAP signaling complexes: pointing towards the next generation of therapeutic targets?', *Trends Pharmacol Sci*, 34: 648-55.

Fabbro, D., S. W. Cowan-Jacob, H. Mobitz, and G. Martiny-Baron. 2012. 'Targeting cancer with small-molecular-weight kinase inhibitors', *Methods Mol Biol*, 795: 1-34.

Ferguson, F. M., and N. S. Gray. 2018. 'Kinase inhibitors: the road ahead', *Nat Rev Drug Discov*, 17: 353-77.

Fogeron, M. L., H. Muller, S. Schade, F. Dreher, V. Lehmann, A. Kuhnel, A. K. Scholz, K. Kashofer, A. Zerck, B. Fauler, R. Lurz, R. Herwig, K. Zatloukal, H. Lehrach, J. Gobom, E. Nordhoff, and B. M. Lange. 2013. 'LGALS3BP regulates centriole biogenesis and centrosome hypertrophy in cancer cells', *Nat Commun*, 4: 1531.

Friesen, D. E., K. H. Barakat, V. Semenchenko, R. Perez-Pineiro, B. W. Fenske, J. Mane, D. S. Wishart, and J. A. Tuszynski. 2012. 'Discovery of small molecule inhibitors that interact with gamma-tubulin', *Chem Biol Drug Des*, 79: 639-52.

Fulcher, L. J., and G. P. Sapkota. 2020. 'Mitotic kinase anchoring proteins: the navigators of cell division', *Cell Cycle*, 19: 505-24.

Gabrovsek, Laura, Paula Bucko, Graeme K. Carnegie, and John D. Scott. 2017. 'A-Kinase Anchoring Protein (AKAP).' in Sangdun Choi (ed.), *Encyclopedia of Signaling Molecules* (Springer New York: New York, NY).

Gelens, L., J. Qian, M. Bollen, and A. T. Saurin. 2018. 'The Importance of Kinase-Phosphatase Integration: Lessons from Mitosis', *Trends Cell Biol*, 28: 6-21.

Gelman, I. H. 2010. 'Emerging Roles for SSeCKS/Gravin/AKAP12 in the Control of Cell Proliferation, Cancer Malignancy, and Barriergenesis', *Genes Cancer*, 1: 1147-56.

———. 2012. 'Suppression of tumor and metastasis progression through the scaffolding functions of SSeCKS/Gravin/AKAP12', *Cancer Metastasis Rev*, 31: 493-500.

Gheghiani, L., D. Loew, B. Lombard, J. Mansfeld, and O. Gavet. 2017. 'PLK1 Activation in Late G2 Sets Up Commitment to Mitosis', *Cell Rep*, 19: 2060-73.

Gillingham, A. K., and S. Munro. 2000. 'The PACT domain, a conserved centrosomal targeting motif in the coiled-coil proteins AKAP450 and pericentrin', *EMBO Rep*, 1: 524-9.

Glover, D. M., M. H. Leibowitz, D. A. McLean, and H. Parry. 1995. 'Mutations in aurora prevent centrosome separation leading to the formation of monopolar spindles', *Cell*, 81: 95-105.

Gold, M. G., S. L. Reichow, S. E. O'Neill, C. R. Weisbrod, L. K. Langeberg, J. E. Bruce, T. Gonen, and J. D. Scott. 2012. 'AKAP2 anchors PKA with aquaporin-0 to support ocular lens transparency', *EMBO Mol Med*, 4: 15-26.

Gordon, T., B. Grove, J. C. Loftus, T. O'Toole, R. McMillan, J. Lindstrom, and M. H. Ginsberg. 1992. 'Molecular cloning and preliminary characterization of a novel cytoplasmic antigen recognized by myasthenia gravis sera', *J Clin Invest*, 90: 992-9.

Goshima, G., T. Kiyomitsu, K. Yoda, and M. Yanagida. 2003. 'Human centromere chromatin protein hMis12, essential for equal segregation, is independent of CENP-A loading pathway', *J Cell Biol*, 160: 25-39.

Gower, C. M., J. R. Thomas, E. Harrington, J. Murphy, M. E. Chang, I. Cornella-Taracido, R. K. Jain, M. Schirle, and D. J. Maly. 2016. 'Conversion of a Single Polypharmacological Agent into Selective Bivalent Inhibitors of Intracellular Kinase Activity', *ACS Chem Biol*, 11: 121-31.

Gupta, G. D., and L. Pelletier. 2017. 'Centrosome Biology: Polymer-Based Centrosome Maturation', *Curr Biol*, 27: R836-R39.

Gutteridge, R. E., M. A. Ndiaye, X. Liu, and N. Ahmad. 2016. 'Plk1 Inhibitors in Cancer Therapy: From Laboratory to Clinics', *Mol Cancer Ther*, 15: 1427-35.

Hannak, E., M. Kirkham, A. A. Hyman, and K. Oegema. 2001. 'Aurora-A kinase is required for centrosome maturation in Caenorhabditis elegans', *J Cell Biol*, 155: 1109-16.

Haren, L., M. H. Remy, I. Bazin, I. Callebaut, M. Wright, and A. Merdes. 2006. 'NEDD1-dependent recruitment of the gamma-tubulin ring complex to the centrosome is necessary for centriole duplication and spindle assembly', *J Cell Biol*, 172: 505-15.

Haren, L., T. Stearns, and J. Luders. 2009. 'Plk1-dependent recruitment of gamma-tubulin complexes to mitotic centrosomes involves multiple PCM components', *PLoS One*, 4: e5976.

He, Y., W. Jiang, X. Qian, F. Liu, Q. Zhang, and C. You. 2015. 'Role of Aurora-A in Ovarian Cancer: A Meta-Analysis', *Oncol Res Treat*, 38: 442-7.

Hehnly, H., D. Canton, P. Bucko, L. K. Langeberg, L. Ogier, I. Gelman, L. F. Santana, L. Wordeman, and J. D. Scott. 2015. 'A mitotic kinase scaffold depleted in testicular seminomas impacts spindle orientation in germ line stem cells', *Elife*, 4: e09384.

Hendrickson, T. W., J. Yao, S. Bhadury, A. H. Corbett, and H. C. Joshi. 2001. 'Conditional mutations in gamma-tubulin reveal its involvement in chromosome segregation and cytokinesis', *Mol Biol Cell*, 12: 2469-81.

Hill, Z. B., B. G. Perera, S. S. Andrews, and D. J. Maly. 2012. 'Targeting diverse signaling interaction sites allows the rapid generation of bivalent kinase inhibitors', *ACS Chem Biol*, 7: 487-95.

Hinshaw, S. M., and S. C. Harrison. 2018. 'Kinetochore Function from the Bottom Up', *Trends Cell Biol*, 28: 22-33.

Hoelder, S., P. A. Clarke, and P. Workman. 2012. 'Discovery of small molecule cancer drugs: successes, challenges and opportunities', *Mol Oncol*, 6: 155-76.

Huang, L. J., K. Durick, J. A. Weiner, J. Chun, and S. S. Taylor. 1997. 'Identification of a novel protein kinase A anchoring protein that binds both type I and type II regulatory subunits', *J Biol Chem*, 272: 8057-64.

Jones, M. J., and P. V. Jallepalli. 2016. 'Engineering and Functional Analysis of Mitotic Kinases Through Chemical Genetics', *Methods Mol Biol*, 1413: 349-63.

Joukov, V., and A. De Nicolo. 2018. 'Aurora-PLK1 cascades as key signaling modules in the regulation of mitosis', *Sci Signal*, 11.

Joukov, V., A. De Nicolo, A. Rodriguez, J. C. Walter, and D. M. Livingston. 2010. 'Centrosomal protein of 192 kDa (Cep192) promotes centrosome-driven spindle assembly by engaging in organelle-specific Aurora A activation', *Proc Natl Acad Sci U S A*, 107: 21022-7.

Kang, Y. H., J. E. Park, L. R. Yu, N. K. Soung, S. M. Yun, J. K. Bang, Y. S. Seong, H. Yu, S. Garfield, T. D. Veenstra, and K. S. Lee. 2006. 'Self-regulated Plk1 recruitment to kinetochores by the Plk1-PBIP1 interaction is critical for proper chromosome segregation', *Mol Cell*, 24: 409-22.

Katsetos, C. D., G. Reddy, E. Draberova, B. Smejkalova, L. Del Valle, Q. Ashraf, A. Tadevosyan, K. Yelin, T. Maraziotis, O. P. Mishra, S. Mork, A. Legido, J. Nissanov, P. W. Baas, J. P. de Chadarevian, and P. Draber. 2006. 'Altered cellular distribution and subcellular sorting of gamma-tubulin in diffuse astrocytic gliomas and human glioblastoma cell lines', *J Neuropathol Exp Neurol*, 65: 465-77.

Kawashima, A. T., and A. C. Newton. 2020. 'Pharmacology on Target', *Trends Pharmacol Sci*, 41: 227-30.

Kennedy, E. J., and J. D. Scott. 2015. 'Selective disruption of the AKAP signaling complexes', *Methods Mol Biol*, 1294: 137-50.

Keppler, A., S. Gendreizig, T. Gronemeyer, H. Pick, H. Vogel, and K. Johnsson. 2003. 'A general method for the covalent labeling of fusion proteins with small molecules in vivo', *Nat Biotechnol*, 21: 86-9.

Klaeger, S., S. Heinzlmeir, M. Wilhelm, H. Polzer, B. Vick, P. A. Koenig, M. Reinecke, B. Ruprecht, S. Petzoldt, C. Meng, J. Zecha, K. Reiter, H. Qiao, D. Helm, H. Koch, M. Schoof, G. Canevari, E. Casale, S. R. Depaolini, A. Feuchtinger, Z. Wu, T. Schmidt, L. Rueckert, W. Becker, J. Huenges, A. K. Garz, B. O. Gohlke, D. P. Zolg, G. Kayser, T. Vooder, R. Preissner, H. Hahne, N. Tonisson, K. Kramer, K. Gotze, F. Bassermann, J. Schlegl, H. C. Ehrlich, S. Aiche, A. Walch, P. A. Greif, S. Schneider, E. R. Felder, J. Ruland, G. Medard, I. Jeremias, K. Spiekermann, and B. Kuster. 2017. 'The target landscape of clinical kinase drugs', *Science*, 358.

Koch, A., H. B. Rode, A. Richters, D. Rauh, and S. Hauf. 2012. 'A chemical genetic approach for covalent inhibition of analogue-sensitive aurora kinase', *ACS Chem Biol*, 7: 723-31.

Koh, H. M., B. G. Jang, C. L. Hyun, Y. S. Kim, J. W. Hyun, W. Y. Chang, and Y. H. Maeng. 2017. 'Aurora Kinase A Is a Prognostic Marker in Colorectal Adenocarcinoma', *J Pathol Transl Med*, 51: 32-39.

Kovanich, D., M. A. van der Heyden, T. T. Aye, T. A. van Veen, A. J. Heck, and A. Scholten. 2010. 'Sphingosine kinase interacting protein is an A-kinase anchoring protein specific for type I cAMP-dependent protein kinase', *Chembiochem*, 11: 963-71.

Kufer, T. A., H. H. Sillje, R. Korner, O. J. Gruss, P. Meraldi, and E. A. Nigg. 2002. 'Human TPX2 is required for targeting Aurora-A kinase to the spindle', *J Cell Biol*, 158: 617-23.

Lane, H. A., and E. A. Nigg. 1996. 'Antibody microinjection reveals an essential role for human polo-like kinase 1 (Plk1) in the functional maturation of mitotic centrosomes', *J Cell Biol*, 135: 1701-13.

Langeberg, L. K., and J. D. Scott. 2015. 'Signalling scaffolds and local organization of cellular behaviour', *Nat Rev Mol Cell Biol*, 16: 232-44.

Lee, K. S., T. R. Burke, Jr., J. E. Park, J. K. Bang, and E. Lee. 2015. 'Recent Advances and New Strategies in Targeting Plk1 for Anticancer Therapy', *Trends Pharmacol Sci*, 36: 858-77.

Lee, K. S., and R. L. Erikson. 1997. 'Plk is a functional homolog of Saccharomyces cerevisiae Cdc5, and elevated Plk activity induces multiple septation structures', *Mol Cell Biol*, 17: 3408-17.

Lee, K. S., J. E. Park, Y. H. Kang, W. Zimmerman, N. K. Soung, Y. S. Seong, S. J. Kwak, and R. L. Erikson. 2008. 'Mechanisms of mammalian polo-like kinase 1 (Plk1) localization: self- versus non-self-priming', *Cell Cycle*, 7: 141-5.

Leibowitz, M. L., C. Z. Zhang, and D. Pellman. 2015. 'Chromothripsis: A New Mechanism for Rapid Karyotype Evolution', *Annu Rev Genet*, 49: 183-211.

Lemmon, M. A., D. M. Freed, J. Schlessinger, and A. Kiyatkin. 2016. 'The Dark Side of Cell Signaling: Positive Roles for Negative Regulators', *Cell*, 164: 1172-84.

Lenart, P., M. Petronczki, M. Steegmaier, B. Di Fiore, J. J. Lipp, M. Hoffmann, W. J. Rettig, N. Kraut, and J. M. Peters. 2007. 'The small-molecule inhibitor BI 2536 reveals novel insights into mitotic roles of polo-like kinase 1', *Curr Biol*, 17: 304-15.

Lens, S. M., E. E. Voest, and R. H. Medema. 2010. 'Shared and separate functions of polo-like kinases and aurora kinases in cancer', *Nat Rev Cancer*, 10: 825-41.

Lera, R. F., G. K. Potts, A. Suzuki, J. M. Johnson, E. D. Salmon, J. J. Coon, and M. E. Burkard. 2016. 'Decoding Polo-like kinase 1 signaling along the kinetochore-centromere axis', *Nat Chem Biol*, 12: 411-8.

Levine, M. S., and A. J. Holland. 2018. 'The impact of mitotic errors on cell proliferation and tumorigenesis', *Genes Dev*, 32: 620-38.

Li, S., Z. Deng, J. Fu, C. Xu, G. Xin, Z. Wu, J. Luo, G. Wang, S. Zhang, B. Zhang, F. Zou, Q. Jiang, and C. Zhang. 2015. 'Spatial Compartmentalization Specializes the Function of Aurora A and Aurora B', *J Biol Chem*, 290: 17546-58.

Littlepage, L. E., H. Wu, T. Andresson, J. K. Deanehan, L. T. Amundadottir, and J. V. Ruderman. 2002. 'Identification of phosphorylated residues that affect the activity of the mitotic kinase Aurora-A', *Proc Natl Acad Sci U S A*, 99: 15440-5.

Lomas, O., and M. Zaccolo. 2014. 'Phosphodiesterases maintain signaling fidelity via compartmentalization of cyclic nucleotides', *Physiology (Bethesda)*, 29: 141-9.

Mack, K., and M. J. M. Fischer. 2017. 'Disrupting sensitization of TRPV4', *Neuroscience*, 352: 1-8.

Macurek, L., A. Lindqvist, D. Lim, M. A. Lampson, R. Klompmaker, R. Freire, C. Clouin, S. S. Taylor, M. B. Yaffe, and R. H. Medema. 2008. 'Polo-like kinase-1 is activated by aurora A to promote checkpoint recovery', *Nature*, 455: 119-23.

Manfredi, M. G., J. A. Ecsedy, A. Chakravarty, L. Silverman, M. Zhang, K. M. Hoar, S. G. Stroud, W. Chen, V. Shinde, J. J. Huck, D. R. Wysong, D. A. Janowick, M. L. Hyer, P. J. Leroy, R. E. Gershman, M. D. Silva, M. S. Germanos, J. B. Bolen, C. F. Claiborne, and T. B. Sells. 2011. 'Characterization of Alisertib (MLN8237), an investigational small-molecule inhibitor of aurora A kinase using novel in vivo pharmacodynamic assays', *Clin Cancer Res*, 17: 7614-24.

Manning, J. A., S. Shalini, J. M. Risk, C. L. Day, and S. Kumar. 2010. 'A direct interaction with NEDD1 regulates gamma-tubulin recruitment to the centrosome', *PLoS One*, 5: e9618.

Maounis, N. F., E. Draberova, E. Mahera, M. Chorti, V. Caracciolo, T. Sulimenko, D. Riga, N. Trakas, A. Emmanouilidou, A. Giordano, P. Draber, and C. D. Katsetos. 2012. 'Overexpression of gamma-tubulin in non-small cell lung cancer', *Histol Histopathol*, 27: 1183-94.

Marumoto, T., T. Hirota, T. Morisaki, N. Kunitoku, D. Zhang, Y. Ichikawa, T. Sasayama, S. Kuninaka, T. Mimori, N. Tamaki, M. Kimura, Y. Okano, and H. Saya. 2002. 'Roles of aurora-A kinase in mitotic entry and G2 checkpoint in mammalian cells', *Genes Cells*, 7: 1173-82.

Means, C. K., B. Lygren, L. K. Langeberg, A. Jain, R. E. Dixon, A. L. Vega, M. G. Gold, S. Petrosyan, S. S. Taylor, A. N. Murphy, T. Ha, L. F. Santana, K. Tasken, and J. D. Scott. 2011. 'An entirely specific type I A-kinase anchoring protein that can sequester two molecules of protein kinase A at mitochondria', *Proc Natl Acad Sci U S A*, 108: E1227-35.

Moritz, M., M. B. Braunfeld, J. W. Sedat, B. Alberts, and D. A. Agard. 1995. 'Microtubule nucleation by gamma-tubulin-containing rings in the centrosome', *Nature*, 378: 638-40.

Muller, H., M. L. Fogeron, V. Lehmann, H. Lehrach, and B. M. Lange. 2006. 'A centrosome-independent role for gamma-TuRC proteins in the spindle assembly checkpoint', *Science*, 314: 654-7.

Muramatsu, M., L. Gao, J. Peresie, B. Balderman, S. Akakura, and I. H. Gelman. 2017. 'SSeCKS/AKAP12 scaffolding functions suppress B16F10-induced peritoneal metastasis by attenuating CXCL9/10 secretion by resident fibroblasts', *Oncotarget*, 8: 70281-98.

Nauert, J. B., T. M. Klauck, L. K. Langeberg, and J. D. Scott. 1997. 'Gravin, an autoantigen recognized by serum from myasthenia gravis patients, is a kinase scaffold protein', *Curr Biol*, 7: 52-62.

Newlon, M. G., M. Roy, Z. E. Hausken, J. D. Scott, and P. A. Jennings. 1997. 'The A-kinase anchoring domain of type IIalpha cAMP-dependent protein kinase is highly helical', *J Biol Chem*, 272: 23637-44.

Newton, A. C., and J. Brognard. 2017. 'Reversing the Paradigm: Protein Kinase C as a Tumor Suppressor', *Trends Pharmacol Sci*, 38: 438-47.

Nigg, E. A., and T. Stearns. 2011. 'The centrosome cycle: Centriole biogenesis, duplication and inherent asymmetries', *Nat Cell Biol*, 13: 1154-60.

Nikonova, A. S., I. Astsaturov, I. G. Serebriiskii, R. L. Dunbrack, Jr., and E. A. Golemis. 2013. 'Aurora A kinase (AURKA) in normal and pathological cell division', *Cell Mol Life Sci*, 70: 661-87.

Niu, Y., T. Liu, G. M. Tse, B. Sun, R. Niu, H. M. Li, H. Wang, Y. Yang, X. Ye, Y. Wang, Q. Yu, and F. Zhang. 2009. 'Increased expression of centrosomal alpha, gamma-tubulin in atypical ductal hyperplasia and carcinoma of the breast', *Cancer Sci*, 100: 580-7.

Nygren, P. J., S. Mehta, D. K. Schweppe, L. K. Langeberg, J. L. Whiting, C. R. Weisbrod, J. E. Bruce, J. Zhang, D. Veesler, and J. D. Scott. 2017. 'Intrinsic disorder within AKAP79 fine-tunes anchored phosphatase activity toward substrates and drug sensitivity', *Elife*, 6.

Nygren, P. J., and J. D. Scott. 2016. 'Regulation of the phosphatase PP2B by protein-protein interactions', *Biochem Soc Trans*, 44: 1313-19.

Parada, C. A., J. Osbun, S. Kaur, Y. Yakkioui, M. Shi, C. Pan, T. Busald, Y. Karasozen, L. F. Gonzalez-Cuyar, R. Rostomily, J. Zhang, and M. Ferreira, Jr. 2018. 'Kinome and phosphoproteome of high-grade meningiomas reveal AKAP12 as a central regulator of aggressiveness and its possible role in progression', *Sci Rep*, 8: 2098.

Pines, J., and C. L. Rieder. 2001. 'Re-staging mitosis: a contemporary view of mitotic progression', *Nat Cell Biol*, 3: E3-6.

Prosser, S. L., and L. Pelletier. 2017. 'Mitotic spindle assembly in animal cells: a fine balancing act', *Nat Rev Mol Cell Biol*, 18: 187-201.

Rosenmund, C., D. W. Carr, S. E. Bergeson, G. Nilaver, J. D. Scott, and G. L. Westbrook. 1994. 'Anchoring of protein kinase A is required for modulation of AMPA/kainate receptors on hippocampal neurons', *Nature*, 368: 853-6.

Schleicher, K., and M. Zaccolo. 2018. 'Using cAMP Sensors to Study Cardiac Nanodomains', *J Cardiovasc Dev Dis*, 5.

Schrade, K., J. Troger, A. Eldahshan, K. Zuhlke, K. R. Abdul Azeez, J. M. Elkins, M. Neuenschwander, A. Oder, M. Elkewedi, S. Jaksch, K. Andrae, J. Li, J. Fernandes, P. M. Muller, S. Grunwald, S. F. Marino, T. Vukicevic, J. Eichhorst, B. Wiesner, M. Weber, M. Kapiloff, O. Rocks, O. Daumke, T. Wieland, S. Knapp, J. P. von Kries, and E. Klussmann. 2018. 'An AKAP-Lbc-RhoA interaction inhibitor promotes the translocation of aquaporin-2 to the plasma membrane of renal collecting duct principal cells', *PLoS One*, 13: e0191423.

Scott, J. D., C. W. Dessauer, and K. Tasken. 2013. 'Creating order from chaos: cellular regulation by kinase anchoring', *Annu Rev Pharmacol Toxicol*, 53: 187-210.

Scott, J. D., and T. Pawson. 2009. 'Cell signaling in space and time: where proteins come together and when they're apart', *Science*, 326: 1220-4.

Scutt, P. J., M. L. Chu, D. A. Sloane, M. Cherry, C. R. Bignell, D. H. Williams, and P. A. Eyers. 2009. 'Discovery and exploitation of inhibitor-resistant aurora and polo kinase mutants for the analysis of mitotic networks', *J Biol Chem*, 284: 15880-93.

Seki, A., J. A. Coppinger, C. Y. Jang, J. R. Yates, and G. Fang. 2008. 'Bora and the kinase Aurora a cooperatively activate the kinase Plk1 and control mitotic entry', *Science*, 320: 1655-8.

Sloane, D. A., M. Z. Trikic, M. L. Chu, M. B. Lamers, C. S. Mason, I. Mueller, W. J. Savory, D. H. Williams, and P. A. Eyers. 2010. 'Drug-resistant aurora A mutants for cellular target validation of the small molecule kinase inhibitors MLN8054 and MLN8237', *ACS Chem Biol*, 5: 563-76.

Smith, F. D., J. L. Esseltine, P. J. Nygren, D. Veesler, D. P. Byrne, M. Vonderach, I. Strashnov, C. E. Eyers, P. A. Eyers, L. K. Langeberg, and J. D. Scott. 2017. 'Local protein kinase A action proceeds through intact holoenzymes', *Science*, 356: 1288-93.

Smith, F. D., M. H. Omar, P. J. Nygren, J. Soughayer, N. Hoshi, H. T. Lau, C. G. Snyder, T. C. Branon, D. Ghosh, L. K. Langeberg, A. Y. Ting, L. F. Santana, S. E. Ong, M. F. Navedo, and J. D. Scott. 2018. 'Single nucleotide polymorphisms alter kinase anchoring and the subcellular targeting of A-kinase anchoring proteins', *Proc Natl Acad Sci U S A*, 115: E11465-E74.

Smith, F. D., S. L. Reichow, J. L. Esseltine, D. Shi, L. K. Langeberg, J. D. Scott, and T. Gonen. 2013. 'Intrinsic disorder within an AKAP-protein kinase A complex guides local substrate phosphorylation', *Elife*, 2: e01319.

Steegmaier, M., M. Hoffmann, A. Baum, P. Lenart, M. Petronczki, M. Krssak, U. Gurtler, P. Garin-Chesa, S. Lieb, J. Quant, M. Grauert, G. R. Adolf, N. Kraut, J. M. Peters, and W. J. Rettig. 2007. 'BI 2536, a potent and selective inhibitor of polo-like kinase 1, inhibits tumor growth in vivo', *Curr Biol*, 17: 316-22.

Su, B., Y. Bu, D. Engelberg, and I. H. Gelman. 2010. 'SSeCKS/Gravin/AKAP12 inhibits cancer cell invasiveness and chemotaxis by suppressing a protein kinase C- Raf/MEK/ERK pathway', *J Biol Chem*, 285: 4578-86.

Sumara, I., J. F. Gimenez-Abian, D. Gerlich, T. Hirota, C. Kraft, C. de la Torre, J. Ellenberg, and J. M. Peters. 2004. 'Roles of polo-like kinase 1 in the assembly of functional mitotic spindles', *Curr Biol*, 14: 1712-22.

Sunkel, C. E., and D. M. Glover. 1988. 'polo, a mitotic mutant of Drosophila displaying abnormal spindle poles', *J Cell Sci*, 89 (Pt 1): 25-38.

Sutherland, E. W. 1972. 'Studies on the mechanism of hormone action', *Science*, 177: 401-8.

Takai, N., R. Hamanaka, J. Yoshimatsu, and I. Miyakawa. 2005. 'Polo-like kinases (Plks) and cancer', *Oncogene*, 24: 287-91.

Tang, A., K. Gao, L. Chu, R. Zhang, J. Yang, and J. Zheng. 2017. 'Aurora kinases: novel therapy targets in cancers', *Oncotarget*, 8: 23937-54.

Tasken, K., and E. M. Aandahl. 2004. 'Localized effects of cAMP mediated by distinct routes of protein kinase A', *Physiol Rev*, 84: 137-67.

Taylor, S. S., R. Ilouz, P. Zhang, and A. P. Kornev. 2012. 'Assembly of allosteric macromolecular switches: lessons from PKA', *Nat Rev Mol Cell Biol*, 13: 646-58.

Theurkauf, W. E., and R. B. Vallee. 1982. 'Molecular characterization of the cAMP-dependent protein kinase bound to microtubule-associated protein 2', *J Biol Chem*, 257: 3284-90.

Troger, J., M. C. Moutty, P. Skroblin, and E. Klussmann. 2012. 'A-kinase anchoring proteins as potential drug targets', *Br J Pharmacol*, 166: 420-33.

Vader, G., and S. M. Lens. 2008. 'The Aurora kinase family in cell division and cancer', *Biochim Biophys Acta*, 1786: 60-72.

Wang, G., Q. Jiang, and C. Zhang. 2014. 'The role of mitotic kinases in coupling the centrosome cycle with the assembly of the mitotic spindle', *J Cell Sci*, 127: 4111-22.

Welburn, J. P. I., and A. A. Jeyaprakash. 2018. 'Mechanisms of Mitotic Kinase Regulation: A Structural Perspective', *Front Cell Dev Biol*, 6: 6.

Wilhelm, T., D. B. Lipka, T. Witte, J. A. Wierzbinska, S. Fluhr, M. Helf, O. Mucke, R. Claus, C. Konermann, P. Nollke, C. M. Niemeyer, C. Flotho, and C. Plass. 2016. 'Epigenetic silencing of AKAP12 in juvenile myelomonocytic leukemia', *Epigenetics*, 11: 110-9.

Witczak, O., B. S. Skalhegg, G. Keryer, M. Bornens, K. Tasken, T. Jahnsen, and S. Orstavik. 1999. 'Cloning and characterization of a cDNA encoding an A-kinase anchoring protein located in the centrosome, AKAP450', *EMBO J*, 18: 1858-68.

Wong, W., and J. D. Scott. 2004. 'AKAP signalling complexes: focal points in space and time', *Nat Rev Mol Cell Biol*, 5: 959-70.

Xia, W., P. Unger, L. Miller, J. Nelson, and I. H. Gelman. 2001. 'The Src-suppressed C kinase substrate, SSeCKS, is a potential metastasis inhibitor in prostate cancer', *Cancer Res*, 61: 5644-51.

Xu, D., and W. Dai. 2011. 'The function of mammalian Polo-like kinase 1 in microtubule nucleation', *Proc Natl Acad Sci U S A*, 108: 11301-2.

Ye, A. A., J. Deretic, C. M. Hoel, A. W. Hinman, D. Cimini, J. P. Welburn, and T. J. Maresca. 2015. 'Aurora A Kinase Contributes to a Pole-Based Error Correction Pathway', *Curr Biol*, 25: 1842-51.

Zaccolo, M., F. De Giorgi, C. Y. Cho, L. Feng, T. Knapp, P. A. Negulescu, S. S. Taylor, R. Y. Tsien, and T. Pozzan. 2000. 'A genetically encoded, fluorescent indicator for cyclic AMP in living cells', *Nat Cell Biol*, 2: 25-9.

Zhang, X., Q. Chen, J. Feng, J. Hou, F. Yang, J. Liu, Q. Jiang, and C. Zhang. 2009. 'Sequential phosphorylation of Nedd1 by Cdk1 and Plk1 is required for targeting of the gammaTuRC to the centrosome', *J Cell Sci*, 122: 2240-51.

Zheng, Y., M. L. Wong, B. Alberts, and T. Mitchison. 1995. 'Nucleation of microtubule assembly by a gamma-tubulin-containing ring complex', *Nature*, 378: 578-83.

Zimmerman, W. C., J. Sillibourne, J. Rosa, and S. J. Doxsey. 2004. 'Mitosis-specific anchoring of gamma tubulin complexes by pericentrin controls spindle organization and mitotic entry', *Mol Biol Cell*, 15: 3642-57.

Zon, L. I., and R. T. Peterson. 2005. 'In vivo drug discovery in the zebrafish', *Nat Rev Drug Discov*, 4: 35-44.

FINAL WORDS

During the final months of this thesis work, the outbreak of COVID-19 took the world by surprise. As the health crisis spread across the globe, numerous were sickened, many lost jobs, and for most, life completely changed. The hardships experienced were unlike many of us had previously encountered and the sacrifices that were made during this pandemic undoubtedly took their toll. Though it is still unclear when life will return to normal, we must learn and grow from what is to come in the following months. We must also move forth with compassion for our fellow humans and trust that together we can work to overcome even the most challenging obstacles. Finally, we must take this time to recognize that discoveries do not occur overnight and that a continued trust and support of science is important for combating diseases, developing cures, and being prepared for anything the future may bring. While the coming years will surely be filled with many successes and pitfalls, may we emerge from these times with a greater appreciation for our world, our society, and each other.